GDAŃSK UNIVERSITY
OF TECHNOLOGY

The author of the doctoral dissertation: **Aoussaj Sbai**
Scientific discipline: **Physical sciences**

DOCTORAL DISSERTATION

Title of doctoral dissertation: **Theoretical Investigation of Light-Driven Electron Transfer in Molecular Photosensitizers.**

Title of doctoral dissertation (in Polish): **Teoretyczne Badanie Napędzanego Światłem Transferu Elektronów w Molekularnych Fotosensybilizatorach.**

Supervisor
signature
Prof. dr hab. Julien Guthmuller

Gdańsk, 2026

GDAŃSK UNIVERSITY
OF TECHNOLOGY

STATEMENT

The author of the doctoral dissertation: **Aoussaj Sbai**

I, the undersigned, declare that I am aware that in accordance with the provisions of Art. 27 (1) and (2) of the Act of 4th February 1994 on Copyright and Related Rights (Journal of Laws of 2021, item 1062), the university may use my doctoral dissertation entitled:
Theoretical Investigation of Light-Driven Electron Transfer in Molecular Photosensitizers.
for scientific or didactic purposes.[1]

Gdańsk,......................................
....

signature of the PhD student

Aware of criminal liability for violations of the Act of 4th February 1994 on Copyright and Related Rights and disciplinary actions set out in the Law on Higher Education and Science(Journal of Laws 2021, item 478), as well as civil liability, I declare, that the submitted doctoral dissertation is my own work.

I declare, that the submitted doctoral dissertation is my own work performed under and in cooperation with the supervision of **Prof. dr hab. Julien Guthmuller.**

This submitted doctoral dissertation has never before been the basis of an official procedure associated with the awarding of a PhD degree.

All the information contained in the above thesis which is derived from written and electronic sources is documented in a list of relevant literature in accordance with Art. 34 of the Copyright and Related Rights Act.

I confirm that this doctoral dissertation is identical to the attached electronic version.

Gdańsk,......................................
....

signature of the PhD student

I, the undersigned, agree to include an electronic version of the above doctoral dissertation in the open, institutional, digital repository of Gdańsk University of Technology.

Gdańsk,......................................
....

signature of the PhD student

---

[1] Art 27. 1. Educational institutions and entities referred to in art. 7 sec. 1 points 1, 2 and 4–8 of the Act of 20 July 2018 – Law on Higher Education and Science, may use the disseminated works in the original and in translation for the purposes of illustrating the content provided for didactic purposes or in order to conduct research activities, and to reproduce for this purpose disseminated minor works or fragments of larger works.

2. If the works are made available to the public in such a way that everyone can have access to them at the place and time selected by them, as referred to in para. 1, is allowed only for a limited group of people learning, teaching or conducting research, identified by the entities listed in paragraph 1.

Załącznik nr 3/2
do Zarządzenia Rektora PG nr 30/2022 z 14 kwietnia 2022 r.

GDAŃSK UNIVERSITY
OF TECHNOLOGY

GDAŃSK UNIVERSITY
OF TECHNOLOGY

DESCRIPTION OF DOCTORAL DISSERTATION

The Author of the doctoral dissertation: Aoussaj Sbai

Title of doctoral dissertation: Theoretical Investigation of Light-Driven Electron Transfer in Molecular Photosensitizers

Title of doctoral dissertation in Polish: Teoretyczne Badanie Napędzanego Światłem Transferu Elektronów w Molekularnych Fotosensybilizatorach

Language of doctoral dissertation: English

Supervisor: Prof. dr hab. Julien Guthmuller

Date of doctoral defense:

Keywords of doctoral dissertation in Polish:. TD-DFT, DLPNO-STEOM-CCSD, fotouczulacze, dwuskładnikowa, napędzana światłem ewolucja wodoru, warstwy konwersji w dół, szybkości fotofizyczne, barwniki BODIPY

Keywords of doctoral dissertation in English: TD-DFT, DLPNO-STEOM-CCSD, photosensitizers, two-component light-driven hydrogen evolution, down conversion layers, photophysical rates, BODIPY dyes

Summary of doctoral dissertation in Polish:

Niniejsza rozprawa doktorska bada właściwości fotofizyczne układów do pozyskiwania energii odnawialnej z wykorzystaniem symulacji chemii kwantowej. Głównym celem jest wyjaśnienie, w jaki sposób dominujące ścieżki transferu elektronów wpływają na wydajność konwersji energii, zgodnie z obserwacjami przedstawionymi w uprzednio opublikowanych badaniach eksperymentalnych.

Struktura rozprawy jest następująca. Rozdział 2 stanowi przegląd literatury dotyczącej barwników typu BODIPY. Rozdział 3 przedstawia podstawy teoretyczne, w tym równania rządzące oraz założenia leżące u podstaw metod ab initio i teorii funkcjonału gęstości, a także opis populacji stanów elektronowych i związanych z nimi stałych szybkości. Rozdziały 4 i 5 prezentują wyniki obliczeń dotyczących fotoindukowanego transferu elektronów w neutralnych i zredukowanych barwnikach BODIPY istotnych dla produkcji wodoru. Rozdział 6 ocenia przydatność modeli adiabatycznych i wibronicznych w przewidywaniu zachowania fotofizycznego tych układów. Rozdział 7 analizuje charakterystyki absorpcyjne i emisyjne wybranych warstw konwersji w dół przeznaczonych do zastosowań fotowoltaicznych. Ostatni rozdział podsumowuje główne wyniki oraz omawia rolę ścieżek transferu ładunku i efektów skrętnych cząsteczki w badanych układach energii odnawialnej.

Summary of doctoral dissertation in English:

This thesis investigates the photophysical properties of renewable energy harvesting systems using quantum chemistry simulations. The primary objective is to elucidate how dominant electron-transfer pathways affect energy conversion efficiency, as observed in previously reported experimental studies.

The thesis is organized as follows. Chapter 2 reviews the literature on BODIPY dyes. Chapter 3 presents the theoretical framework, including the governing equations and assumptions underlying ab initio and density functional theory methods, as well as the population of electronic state and associated rate constants. Chapters 4 and 5 report computational results on photoinduced electron transfer in neutral and reduced BODIPY dyes relevant to hydrogen production. Chapter 6 evaluates the validity of adiabatic and vibronic models for predicting the photophysical behavior of these systems. Chapter 7 examines the absorption and emission characteristics of selected down-conversion layers for photovoltaic applications. The final chapter summarizes the main findings and discusses the roles of charge-transfer pathways and molecular torsional effects in the renewable energy systems under study.

TABLE OF CONTENTS

ABSTRACT

Theoretical and computational simulations, particularly Density Functional Theory (DFT), play a crucial role in optimizing the performance of materials used in renewable energy technologies, ranging from simple organic dyes to complex molecular triads. While initial quantum-chemical calculations are commonly performed in the gas phase, solvent effects must be considered to reflect experimental conditions better. This is typically achieved through implicit solvation models, such as the Polarizable Continuum Model.

This research focuses on two main areas:

1. **Investigation of the origin of discrepancies in the photocatalytic activity of BODIPY dyes.** The study examines 2,6-iodine-substituted BODIPY dyes bearing –phenyl, –phenylOH, and –phenylNO_2 substituents at the 8-position of the BODIPY core, with emphasis on the influence of substituents and solvent effects on electron-transfer pathways. Previous studies have proposed a two-cycle framework to describe the mechanism underlying hydrogen generation. In this context, time-dependent DFT (TDDFT) calculations were performed for both neutral and reduced BODIPY dyes. The TDDFT results were benchmarked against high-level DLPNO-STEOM-CCSD calculations to assess the reliability of the employed exchange–correlation functional in predicting excitation energies. Finally, photophysical properties, including rate constants described within the Jablonski framework, were evaluated using adiabatic and vertical Hessian models.
2. **Analysis of the electronic structure of down-conversion films used in semitransparent perovskite solar cells (ST-PSCs).**

   This part of the study focuses on the light absorption and emission properties of down-conversion films, with theoretical results validated through close collaboration with an experimental research group.

The computational results indicate that (i) the population of charge-transfer states significantly promotes deactivation of the hydrogen production process in both neutral and reduced forms, whereas the population of long-lived triplet states and doublet bright states correlates with high catalytic turnover; and (ii) aggregation-induced photophysical properties enhance emission efficiency, thereby contributing to improved performance of down-conversion films.

ACKNOWLEDGEMENT

This dissertation would not have been possible without the generous financial support of the Gdańsk University of Technology Scholarship Programme, as well as access grants to the computing facilities of the Wrocław Centre for Networking and Supercomputing and the Academic Computer Centre TASK in Gdańsk.

I am profoundly grateful to my supervisor, *Prof. Julien Guthmuller*, whose unwavering guidance, patience, and professional courtesy were the driving force fueling my research journey. His expertise was both an inspiration and a compass for this work.

I thank my friends from diverse cultural backgrounds, whose humor and companionship sustained morale and rendered the academic journey both seamless and joyful.

Finally, I extend my warmest thanks to my family and my significant other for their boundless emotional support and intellectual spark. Their genuine interest in science provided continual mental stimulation and anchored me throughout my PhD studies. Their belief in me has been my greatest asset.

I will carry the value of all your contributions forward with immense appreciation.

Aoussaj Sbai

LIST OF ABBREVIATIONS

AIE	Aggregation-Induced Emission
BO	Born–Oppenheimer
BODIPY	4,4-difluoro-4-bora-3a,4a-diaza-s-indacene
CASPT2	Complete Active Space Second-Order Perturbation Theory
CASSCF	Complete Active Space Self-Consistent Field
CatC	Catalytic Center
CC	Coupled Cluster method
CC2	Second-Order Coupled-Cluster
CCSD	Coupled Cluster with Singles and Doubles
CDD	Charge Density Difference
CIS	Configuration Interaction Singles
CR	Charge Recombination
CS	Charge Separation
CT	Charge transfer
DCM	Dichloromethane
DFT	Density Functional Theory
DLPNO	Domain-based Local Pair Natural Orbitals
EDG	Electron-Donating Group
EOM-CC	Equation-of-Motion Coupled Cluster
EOM-CCSD	Equation of Motion – Coupled Cluster with Singles and Doubles -
EtOAc	Ethyl acetate
EWG	Electron-Withdrawing Group
FC	Franck-Condon
GaAs	Gallium Arsenide
HF	Hartree–Fock Theory
HOMO	Highest Occupied Molecular Orbital
HT	Herzberg–Teller
HWHM	Half Width at Half Maximum
IC	Internal Conversion
IR	Infrared
ISC	Intersystem Crossing
LR	Linear-Response
LR-TDDFT	Linear-Response Time-Dependent Density Functional Theory
LUMO	Lowest Unoccupied Molecular Orbital
MAD	Mean Absolute Deviation
MP	Møller–Plesset Perturbation theory
NAC	Nonadiabatic Coupling
NEVPT2	N-Electron Valence State Perturbation Theory (Second Order)
PCM	Polarizable Continuum Model
PES	Potential Energy Surface
PET	Photoinduced Electron Transfer
PS	Photosensitizer
QM/MM	Quantum Mechanics/Molecular Mechanics

RASPT2	Restricted Active Space Second-Order Perturbation Theory
RHF	Restricted Hartree–Fock
RPA	Random Phase Approximation
SCAN	Strongly Constrained and Appropriately Normed
SCF	Self-Consistent Field
SED	Sacrificial Electron Donor
Si	Silicon
SOC	Spin-Orbital Coupling
SOS-PBE-QIDH	Spin-Opposite-Scaled Perdew–Burke–Ernzerhof Quadratic-Integrand Double-Hybrid functional
SOS-ωPBEPP86	Spin-Opposite-Scaled range-separated Perdew–Burke–Ernzerhof–Perdew 86 functional
SS	State Specific
TDA	Tamm–Dancoff Approximation
TDDFT	Time-Dependent Density Functional Theory
TF	Thomas–Fermi Model
UHF	Unrestricted Hartree–Fock
UV	Ultraviolet
VG	Vertical Gradient
Vis	Visible
XC	Exchange–Correlation

Chapter 1: Introduction

1.1 Study context and motivation

The global energy crisis presents one of the arduous challenges of the twenty-first century. Global fossil fuel reserves encounter supply constraints in the face of growing demand [1–3]. In response to this imbalance, governments have enacted urgent political and economic policies, including tax incentives and restrictions on energy use, to rationalize consumption. However, these measures are insufficient to address this issue on a permanent basis. Simultaneously, CO_2 emissions increase sharply, escalating greenhouse concerns. This energy hardship has spurred interest in clean and renewable energy technology.

Although the period 2020–2024 witnessed significant growth in renewable energy deployment, reflecting an unprecedented shift toward investment in solar technologies—as highlighted in **Figure 1.1** by the increasing share of solar power in electricity generation—the annual total electricity generation from fossil fuels remains predominant globally. Nevertheless, the increase in renewable energy continues to offer a promising outlook for a sustainable global energy transition [4].

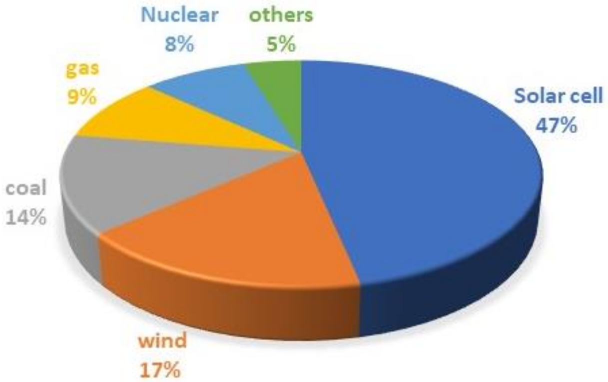

Figure 1.1: Growth in global electricity generation by source, 2000–2024 (%) [4, 5].

Solar energy and water are inexhaustible and abundant resources, considered among the most promising alternatives for generating synthetic fuel and hydrogen, which enables decentralized and resilient power systems. In contrast to hydrogen produced by steam methane reforming, a process that depends on natural gas and emits carbon dioxide [6–8], and to nuclear power, which is susceptible to radioactive leakage and waste storage challenges, light-driven water splitting systems offer a sustainable and pollution-free energy source [9, 10]. The photocatalytic water splitting process relies on two half-reactions:

$$2\mathrm{H_2O} \rightarrow \mathrm{O_2} + 4\mathrm{H^+} + 4\mathrm{e^-} \qquad \text{(water oxidation)}$$
$$4\mathrm{H^+} + 4\mathrm{e^-} \rightarrow 2\mathrm{H_2} \qquad \text{(water reduction)}$$

However, the efficiency of hydrogen production via the water-splitting mechanism remains below expectations compared to conventional methods, preventing large-scale applications. This casts light on the pressing need for ongoing intensive research within this scope.

One of the earliest attempts to develop a water-splitting system employed a titanium dioxide (TiO_2) single-crystal semiconductor electrode. The material harnessed photon energy to drive chemical reactions, ultimately producing hydrogen molecules [11], analogous to the way chlorophyll absorbs light and initiates charge separation through subsequent electron transfer steps [12]. Later, more refinements were made to improve their dye-sensitized photocatalyst structure; however, these structures are very sensitive to environmental factors such as charge carrier concentration, temperature, and the complexity of interfacial charge transport [13–15]. These drawbacks prompted the exploration of partially semiconductor-free alternatives, namely supramolecular and multicomponent molecular photocatalytic systems [16, 17].

Effective optimization of single-component or multi-component water-reduction systems requires the fulfillment of several key criteria:

1. The photosensitizer (PS) must exhibit broad absorption across the entire visible spectrum and the near-infrared region, functioning as a “black dye.” These properties can be tuned through the attachment of suitable substituents.
2. Upon irradiation, the excited state of the photosensitizer should possess sufficient energy to generate a charge-separated state (CS) and enable unidirectional electron transfer from the donor (photosensitizer) to the acceptor (catalytic center).
3. The lifetime of the charge-separated state should be sufficiently long to ensure compound stability and to outcompete charge recombination (CR), i.e., back electron transfer.
4. The photosensitizer must exhibit adequate stability under light, heat, and electricity.

In the supramolecular assembly (**Figure 1.2.1**), the photosensitizer and the catalytic center are covalently linked to ensure a rapid intramolecular electron transfer and to reduce diffusion. A classic example of such a one-component system is the Ru(II)–Pt(II) complex reported by Sakai et al [18], which was described as the first effective molecular device capable of producing H_2 from water under visible light irradiation. In this molecular system, the tris(bipyridine)ruthenium(II) moiety functions as the photosensitizer and absorbs light through metal-to-ligand charge transfer excitations, leading to the reduction of the bridging 2,6-bis(pyrazol-1-yl)pyridine (bpp) ligand. Subsequently, an electron is transferred via the bpp ligand to the catalytically active platinum center. Upon accumulation of two electrons at the catalytic site, proton reduction occurs, resulting in hydrogen evolution. Meanwhile, the Ru(II) center is regenerated by ethylenediaminetetraacetic acid, which serves as a sacrificial electron donor (SED). On the other hand, multi-component water reduction systems (**Figure 1.2.2**) involve a light absorber, a catalytic center (CatC), and an electron donor, linked via intermolecular forces in a synergistic way within the same solution phase. This approach enables independent tuning and optimization of the performance of the photosensitizer and the photocatalyst. However, such assemblies face challenges due to high diffusion rates, which can introduce kinetic bottlenecks and promote faster CR. For instance, $[Ru(bpy)_3]Cl_2$ absorbs light and transitions to a long-lived excited state, which, due to its favorable redox potential, is capable of donating an electron to the mediator $[MV]^{2+}$ (methyl viologen). The mediator subsequently shuttles the electron to the catalytic center. The oxidized $[Ru(bpy)_3]^{3+}$ species is then regenerated by accepting an electron from a sacrificial donor, such as triethanolamine [19].

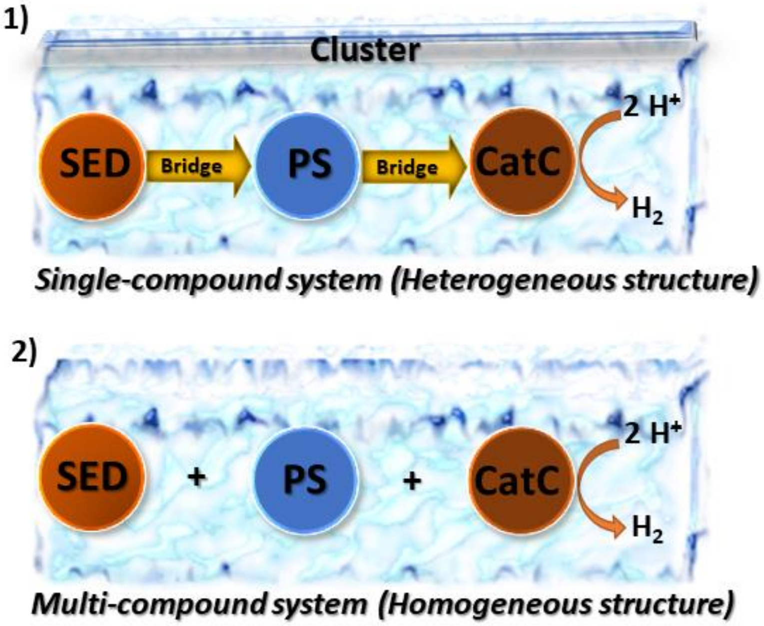

Figure 1.2: Two different water-splitting hydrogen systems.

These structures can be implemented within either homogeneous architectures, which require long-lived excited states (microseconds to milliseconds) to facilitate electron transfer during diffusion [20], or heterogeneous architectures, where CS states exhibit shorter lifetimes (picoseconds to nanoseconds) due to the rapid transfer of electrons to another phase (e.g., a solid) [21].

The electronic properties of the various molecular subunits and their coupling should be precisely tuned to meet the aforementioned criteria. In addition, a fundamental theoretical understanding of photo-induced processes is essential for the development of photocatalytic hydrogen production systems. Since the 1970s, transition-metal complexes, particularly those based on ruthenium, platinum, and iridium, have been widely employed as photosensitizers in both homogeneous and heterogeneous systems, demonstrating high turnover frequencies of up to 50,000 s^{-1} [22]. However, these metals are expensive, scarce, and toxic. They also exhibit a narrow absorption window and are susceptible to degradation by water and buffer anions, leading to irreversible decomposition under photocatalytic conditions. These issues have led researchers to investigate metal-free compounds. Multiple studies [23–25] have demonstrated that organic dyes are flexible and tunable, offering numerous possibilities for modifying and enhancing their properties, such as broadening the absorption spectrum, tuning molecular energy levels, improving charge separation, and optimizing inter- or intramolecular interactions. Organic dyes, such as xanthene and cyanine derivatives, are frequently employed as photosensitizers due to their strong absorption and efficient formation of triplet states [26–28]. Dyes based on a boron-dipyrromethene (BODIPY) core share similar advantages but additionally offer higher photostability, chemical versatility, and low toxicity [29, 30].

Recently, BODIPY dyes for two-component systems were investigated both theoretically and experimentally as photosensitizers [31]. The experimental system in this study is a quasi-homogeneous assembly composed of halogenated BODIPY dyes as the photosensitizer, embedded within a poly(dehydroalanine)-graft-poly(ethylene glycol) (PDha-g-PEG) matrix. Ascorbic acid is employed as the sacrificial electron donor, and the ammonium thiomolybdate cluster, $(NH_4)_2[Mo_3S_{13}]$, serves as the hydrogen evolution photocatalyst. Two major results were observed: Firstly, the cyclic voltammetry (CV) data indicate that electron transfer from the BODIPY dye to $[Mo_3S_{13}]^{2-}$ is thermodynamically favorable, according to their respective oxidation and reduction potentials. Secondly, the 2,6-diiodo meso-phenyl-substituted BODIPY dye (BOB-Ph) photosensitizer exhibits the highest catalytic activity, whereas the introduction of either electron-donating (EDG) or electron-withdrawing (EWG) groups at the para position of the meso-phenyl ring is accompanied by a decrease in hydrogen evolution.

Two photocatalytic cycles have been proposed to elucidate the mechanism of hydrogen production. In the first cycle, photoexcitation in the Franck–Condon region populates a bright singlet excited state. Afterward, spin-orbit coupling, enhanced by relativistic effects due to the presence of iodine atoms, facilitates intersystem crossing (ISC) to a triplet excited state. At this stage, two hypotheses have been proposed. The first (**Figure 1.3.1**) suggests that the triplet state involved is a long-lived state localized on the BODIPY core [32]. This state undergoes intermolecular electron transfer to the catalyst, a process that outcompetes the intramolecular charge transfer from the BODIPY core to its substituents, a deactivation pathway [25]. In contrast, the second hypothesis (**Figure 1.3.3**) indicates that ISC directly populates a triplet charge-separated state, in which the electron density is partially transferred toward the phenyl substituent region. Then, an electron transfer occurs via intramolecular interactions (within a supramolecular structure) or intermolecular interactions (between multicomponent structures) toward the catalytic center [33]. Finally, the transferred electron is replenished by the SED. Experimental evidence indicates that the first photocatalytic cycle is associated with a low fluorescence quantum yield, which indicates efficient population of non-emissive (triplet) states.

Conversely, in the second cycle, the reduction of the BODIPY dye by the SED precedes electron transfer to the catalytic center. Depending on the pathway, the SED initially reduces either the lowest triplet state of the BODIPY dye [32] (**Figure 1.3.2**) or the lowest singlet excited state [33] (**Figure 1.3.4**), leading to two different hypotheses via internal conversion (IC) after the formation of the reduced BODIPY species: an electron is transferred to the catalytic center either from the reduced bright state (**Figure 1.3.2**) or from the reduced charge-separated state (**Figure 1.3.4**), leading to hydrogen evolution. The thermodynamic feasibility of this pathway is supported by cyclic voltammetry measurements of redox potentials and by Gibbs free energy calculations based on experimental and theoretical data [33].

A major difficulty in understanding these processes lies in determining whether the reduction and non-reduction steps occur sequentially, simultaneously, or whether one cancels the other. These questions remain unresolved.

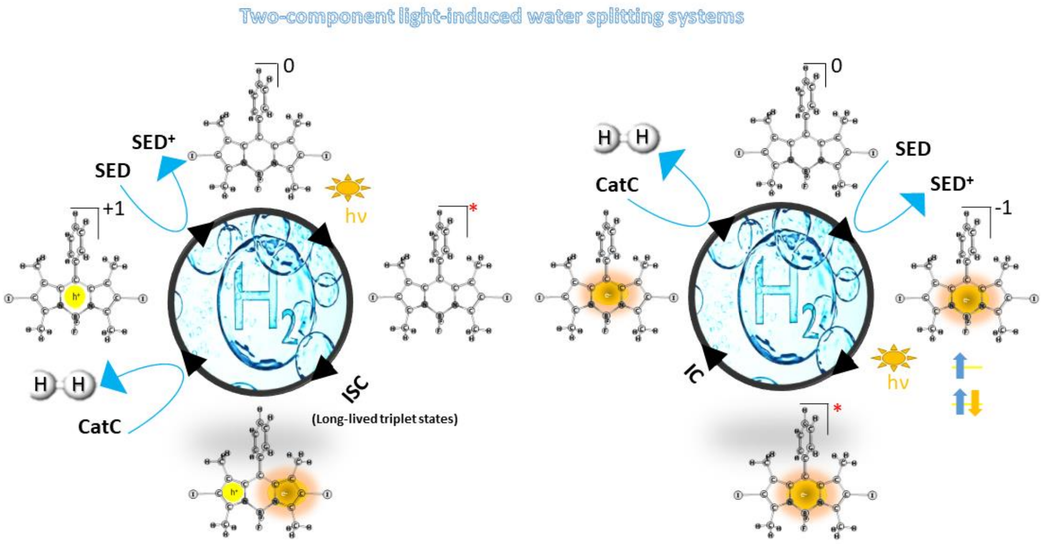

3.1) Non-reduced BOB-Ph compound hydrogen production cycle

3.2) Reduced BOB-Ph compound hydrogen production cycle

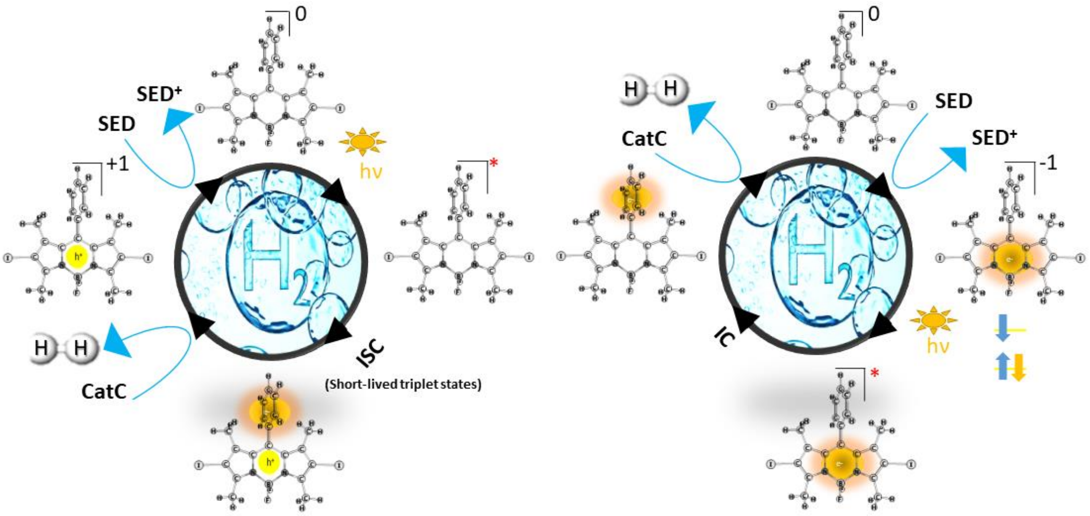

3.3) Non-reduced BOB-Ph compound hydrogen production cycle

3.4) Reduced BOB-Ph compound hydrogen production cycle

Figure 1.3: Hypothesized photocatalytic activity cycles.

In general, no universal photocatalytic cycle can be considered valid for all photophysical situations. Indeed, the latter is governed by multiple factors; for example, the pH of the homogenous structure can affect the protonation state of the SED, while the polarity of the solvent can modulate the stability of reactive intermediates (PS, CatC) involved in the catalytic cycle.

Several endeavors were undertaken through experimental work to design and characterize compounds involved in hydrogen production, such as solubility, integrity, photostability, and toxicity experiments, as well as tuning absorption and emission margin or controlling the degradation of the compound. Nevertheless, theoretical studies are required to give insight into the underlying photophysical properties governing these compounds and rationalize their properties. Despite many computational investigations, the electronic state properties of BODIPY dyes are not yet fully elucidated, and the accuracy of these calculations remains challenging.

1.2 Research goals

In this context, the thesis addresses the following points:

1. Understanding the activation and deactivation pathways upon photoexcitation of BODIPY dyes, and determining the correlation between the differences in catalytic activity among different BODIPY dyes by evaluating the relaxation pathways along the total energy profiles in both the neutral and reduced BODIPY dye cycles.
2. Conducting a theoretical study about the photophysical properties of the BODIPY dye regarding the relaxation rates associated with IC, ISC, and radiative emission, and disentangle the different physical factors that influence these processes.

In the last chapter, the thesis diverges to a different application under the scope of renewable energy: namely, down-conversion materials for perovskite solar cells. This involves the investigation of the electronic structure of the corresponding materials and the simulation of the photophysical spectra (absorption and emission), vertical excitation energies, in order to understand the underlying aspects that affect their efficiency and interpret the experimental data.

Chapter 2: BODIPY: Photophysical Properties and Role in H_2 Production

2.1 BODIPY scaffold and substituent effects

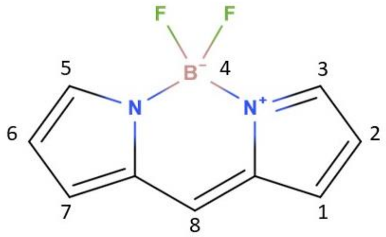

Figure 2.1: Unsubstituted BODIPY moiety.

The BODIPY (4,4-difluoro-4-bora-3a,4a-diaza-s-indacene) core (**Figure 2.1**) has attracted considerable attention in research due to its exceptional chemical plasticity, which allows synthesis through various strategies and tailoring of its properties for specific functions. Substituents, for example, can modulate its aromatic character, resulting in bathochromic or hypsochromic spectral shifts, while others can reduce sensitivity to environmental factors such as temperature and viscosity. As a result, the photophysical behavior of BODIPY derivatives can be precisely tuned, facilitating processes including charge (electron) transfer, energy transfer, and triplet-state population. In other words, through a rational molecular design approach, BODIPY derivatives can be tailored to meet the specific requirements of applications involving organic dyes. Substituents play a crucial role not only in maintaining stability, for instance, by extending the lifetime of electronic states, but also in preventing photodegradation of the molecule.

The potential of such structural modifications is well illustrated in renewable energy applications. For example, a study [34] demonstrated that the performance of dye-sensitized solar cells is strongly influenced by both the position of donor-group substitution and the strength of their electron-donating ability. These factors enhance intermolecular charge transfer (CT) by lowering the LUMO energy level. In particular, an N-methoxyphenyl carbazole unit conjugated to a 2-cyanoacrylate BODIPY module exhibited the highest photovoltaic performance, which was attributed to its broader absorption profile and improved light-harvesting capacity in the visible region when adsorbed onto the TiO_2 surface. Francis D'Souza et al. [35] demonstrated that incorporating BODIPY into a supramolecular triad (C_{60}Im–ZnP–BODIPY) significantly enhances photoinduced electron transfer (PET). In this system, the BODIPY unit acts as an efficient energy donor due to its strong spectral overlap with zinc porphyrin, enabling rapid and high-yield energy transfer ($k_{ENT} = 9.2 \times 10^9$ s^{-1}; the rate constant for singlet–singlet energy transfer from BODIPY to ZnP, with $\Phi_{ENT} = 0.83$) to generate the singlet-excited ZnP. This excited state subsequently transfers an electron to the fullerene acceptor, producing a long-lived CS state (lifetime ≈ 5 ns) with desirable absorption in the near-infrared (~1000 nm). These results highlight how structural modification of BODIPY, by integrating it with porphyrins and fullerenes, optimizes electron transfer, thereby improving light-harvesting efficiency and enabling effective charge separation across the solar spectrum. Another example [36] is the substitution of polydisperse polymers with soluble, conjugated BODIPY derivatives, which enables independent tuning of key photovoltaic parameters such as light absorption, open-circuit voltage, and hole transport. The control of these parameters facilitates the fabrication of bulk heterojunction solar cells with broad absorption profiles and smaller energy-level gaps. However, the efficiency achieved with BODIPY-based devices is still outperformed by a cell employing an oligothiophene donor containing diketopyrrole, which reached a power conversion efficiency of 3.0%.

BODIPY dyes are well known for their strong fluorescence across various solvents, attributed to their rigid, planar, and aromatic structure as well as small Stokes shift (5–20 nm) [37], with the first singlet excited state (S_1) at 2.44 eV in ethanol [38]. The introduction of a phenyl substituent at the meso position significantly reduces fluorescence ($\Phi_F = 0.035$ in dichloromethane, 0.018 in methanol, S_1 at 2.47 eV in dichloromethane, 2.49 eV in methanol) [39]. The mechanism behind this fluorescence quenching has been explored through semiempirical computations. This study [40] reveals the formation of metastable states and non-radiative conformers from the optimized S_1 state, leading to a biphasic lifetime decay. The topology of the potential energy surface (PES) indicates that non-emissive behavior is favorable, as a low-lying conical intersection between the ground state and the relaxed S_1 state is accessible. Furthermore, the rotational energy barrier for the phenyl ring is small, permitting free rotation together with a bending of the BODIPY core. Another study [41] has reported that the optimal ground-state (S_0) geometry of this system features a phenyl ring twisted by approximately 55° relative to the core. In contrast, the first excited-state (S_1)

geometry is nearly planar, with the core–ring dihedral angle approaching 0°. The constrained PES of the S_1 state along the torsional coordinate in the gas phase was found to be significantly flatter than that of S_0, with only a small barrier near 55°, suggesting that relaxation from different excited-state conformations is possible. In methanol, the S_1 PES is red-shifted and exhibits only two minima, located close to the S_0 minima. This solvent-dependent behavior has been interpreted as favoring nonradiative deactivation pathways over radiative decay in polar environments. In contrast, in solvents of lower polarity, the influence of solvation on the excited-state PES appears weaker, and the balance between radiative and nonradiative processes is less well defined. The absorption spectrum computed with time-dependent density functional theory (TDDFT) (BLYP, CAM-B3LYP) using the 6-311++G(2d,2p) basis set is blue shifted compared to experimental data. The deviation originates from the incomplete description of electron correlation with DFT; however, the long-range corrected functional CAM-B3LYP performs better than the generalized gradient approximation functional BLYP [41]. The attachment of methyl groups at the positions C_1 and C_7 of the BODIPY core or at the para-positions of the phenyl group increases the quantum yield of fluorescence ($\Phi_F = 0.65$ in methanol, 0.93 in toluene) [38], leading to relatively long fluorescence lifetimes (>1 ns) [38]. The methyl substituents prevent the rotation of the phenyl, reducing the loss of energy through non-radiative decay; however, it does not enhance the spin-orbit coupling (6.3×10^{-4} cm^{-1}) [42]. The inclusion of iodine at positions 2 and 6 induces a bathochromic shift (from 2.47 eV to 2.31 eV in toluene) and promotes ISC ($k_{ISC} = 4 \times 10^9$ s^{-1}) [43]. The addition of further iodine on para-phenyl decreases the fluorescence lifetime from 3.80 ns to 0.21 ns. The Kohn-Sham orbitals for these molecules calculated with CAM-B3LYP reveal that S_1 and T_1 correspond to π-π* transitions, which indicates that an El-Sayed spin-orbit coupling (SOC) is not considered as a possible ISC pathway in these systems. The optimized excited state geometries of S_1 and T_1 differ significantly near the meso-carbon for iodine-substituted BODIPY compounds, in particular with a BODIPY-phenyl rotation angle going from 61.51° to 79.81°. Moreover, a decrease in adiabatic energy difference between the S_1 and T_1 states (from 1.57 eV to 1.45 eV) is also observed.

The introduction of heteroatoms such as nitrogen or sulfur into the BODIPY core via electrophilic substitution has been shown to reduce fluorescence efficiency by activating PET pathways. However, when these substituents interact with metal ions or under certain pH conditions, the PET process can be suppressed, thus maintaining the strong fluorescence characteristic of BODIPY dyes [44]. An earlier investigation [45] reported that BODIPY substituted with a phenyl–nitrogen dioxide group at the meso position exhibits strongly quenched fluorescence in protic polar solvents (Φ_F = 0.035 in ethanol, 0.014 in methanol, and 0.38 in tetrahydrofuran). The higher emission in tetrahydrofuran was attributed to fluorescence from the locally excited state of the BODIPY core. In contrast, in highly polar methanol, fluorescence is strongly quenched owing to stabilization of a weakly emissive charge-transfer state, which facilitates nonradiative deactivation pathways.

For push–pull type BODIPY compounds [45], comparison of the frontier orbital energies of donor and acceptor units is crucial for rationalizing electron transfer during the oxidative PET pathway. In meso-phenyl-NO_2-substituted BODIPYs, the nearly orthogonal arrangement of the BODIPY and nitrophenyl units (dihedral angle ≈ 88°) allows them to behave as independent chromophores. Following photoexcitation of the BODIPY core, electron transfer from the BODIPY LUMO to the nitrophenyl LUMO can generate a CS state, which either undergoes CR or ISC via back electron transfer with spin inversion (radical-pair ISC mechanism). DFT calculations, however, indicate that $E(LUMO_{Ph\text{-}NO2}) > E(LUMO_{BOD})$, making the back electron transfer energetically unfavorable, which explains the inefficient singlet oxygen (O_2) generation observed. Hu et al. [46] confirmed that the inclusion of NO_2 closer to the BODIPY core increases the red-shift of the maximum absorption λ_{abs}. However, the increase in solvent polarity causes a slight blue shift (S_1 at 2.47 eV in acetonitrile, 2.45 eV in n-hexane) and stabilizes the CS state. Moreover, the assessment of PET thermodynamic driving force reveals some requirement for triplet state formation. However, these requirements are not satisfied for BODIPY derivatives bearing EWG, since E_{gap}(BODIPY) > E_{gap}(EWG) and E_{LUMO}(BODIPY) > E_{LUMO}(EWG) upon photoexcitation of the BODIPY core [46]. The insertion of EDG (OMe, I) on the para phenyl does not affect the extinction coefficients; however, it induces a slight blue shift and destabilizes the LUMO of the compounds, which increases the fluorescence quantum yields and singlet oxygen production. DFT calculations, performed using PBE1PBE/6-31+G(d,p), show an increase in the HOMO-LUMO gap going from EDG-BODIPY dyes to EWG-BODIPY dyes by 0.2-0.6 eV (**Figure 2.2**). This in turn inhibits the electron transfer from the LUMO of the excited BODIPY fluorophore to the LUMO of the benzene moiety and therefore switches on the fluorescence of the BODIPY moiety [47].

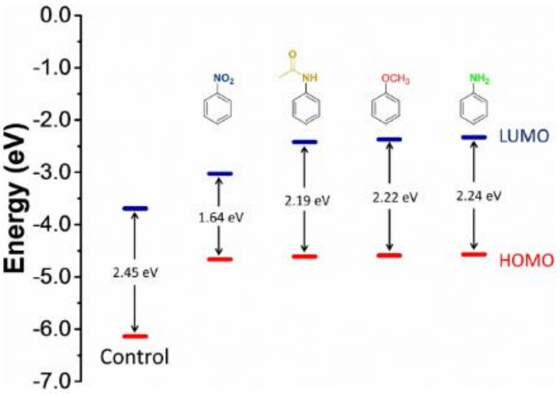

Figure 2.2: Energy level of substituted BODIPY dyes [48].

Computational studies at the M06-2X/6-31G(d,p) level indicate that the unpaired electron in the reduced BODIPY core is primarily localized at the 8-position (≈ 32%) and to a lesser extent at the 1,7-positions (≈ 24%) [37]. Substitution with either methyl or chloride groups has only a minor influence, with spin density variations below 1%. The presence of a methyl group makes the dye more difficult to reduce, shifting the reduction potential by roughly 100–150 mV toward more negative values. Systematic investigations into substitution effects on BODIPY reduction potentials revealed that modification at the 3-position produces the largest negative shift, followed by substitution at the 8- and 1-positions. In general, EWGs stabilize the LUMO and thereby facilitate reduction, while EDGs destabilize the LUMO and impede reduction. Bard and colleagues [49] demonstrated that the introduction of a cyano group at the 8-position, through its inductive electron-withdrawing effect, lowers the reduction potential by approximately 300 mV compared to a methyl-substituted analogue. In contrast, strongly donating substituents such as diethylamine induce the reverse effect.

2.2 Halogenated BODIPY compounds

The ground state of the majority of organic molecules is a singlet, while the excited states are either singlets or triplets. In theory, transitions between states with the same spin value are permitted, but transitions between states with opposing spin values are forbidden. During fluorescence, the spin-permitted radiative process deactivates S_1 to S_0 and competes with internal conversion and with intersystem crossing. As BODIPY dyes are fluorescent compounds, they usually have relatively weak SOCs and, consequently, a low population rate of the lowest triplet state.

Several factors can be tuned in order to increase the SOCs and ISCs between singlet and triplet states:

1. The SOC is proportional to Z^4, where Z is the atomic number. Therefore, the introduction of heavy atoms will increase the SOCs (i.e., heavy atom effect).
2. If the singlet-triplet non-radiative transition is accompanied by a change in the orbital characters (e.g., $^1\pi\pi^* \rightarrow {}^3n\pi^*$) the SOCs will likely be large (i.e., El-Sayed rule).
3. The energy gap between the triplet and singlet states should be small (i.e., energy gap law).

Organic photosensitizers with efficient ISC and stable triplet excited states play an essential role in a variety of applications such as triplet-triplet annihilation upconversion, photodynamic therapy, and hydrogen production. A prevalent strategy in the creation of such dyes is the incorporation of heavy atoms (e.g., transition metals or halogens) that increase ISC through SOC interactions. In recent years, other ISC enhancement strategies have emerged and are actively investigated. Among them, exciton coupling and singlet fission, as well as the production of triplet excited states by PET in heavy-atom-free molecules, have garnered special interest since they permit the construction of photosensitizers with adjustable triplet state and fluorescence quantum yields [50].

In theory, non-radiative processes may create a triplet state through either radical-pair ISC due to exchange interaction corresponding to antibonding orbital overlap [51] or spin-orbit CT. The latter happens if the system is compact and the donor and acceptor moieties involved in CT are orthogonal. This leads to a change in orbital angular momentum during the transition, which can be compensated by an electron spin-flip in order to satisfy the rule of total angular momentum conservation. The radical-pair ISC is likely to take place in natural photosynthetic reaction centers and in various electron donor-acceptor complexes with large separation distances (e.g., > 15 Å) and weak electronic coupling between the donor and acceptor subunits. During this process, upon photoexcitation, a singlet CT state is created that decays to an intermediate singlet CT state, followed by a triplet CT state [52]. For strong electronic coupling, hyperfine structure is favored, leading to a direct conversion to the lowest CR triplet state. Related to this concern, Wang et al. [53] compared two BODIPY–TEMPO dyads with different linkers. The study reveals that the fluorescence of the BODIPY unit was quenched in the dyads. The quantum yield for dyad 1 attained 29%, while for dyad 2 it is limited to 5%. The triplet-state lifetimes of the dyads were 190 and 62 µs, respectively. Quantum yields of singlet oxygen formation for dyads 1 and 2 were estimated to be 14% and 56%, respectively. These results indicate that the second linker length is optimal for achieving both efficient ISC and a stable triplet state [53].

For halogenated compounds, the presence of a high–atomic-number atom induces a significant enhancement of spin-forbidden processes. In particular, incorporation of iodine at the 2,6-positions of a BODIPY dye bearing a phthalimido or amino substituent on the phenoxyoctyl group at the meso position leads to a marked increase in singlet oxygen generation (Φ_Δ ~ 0.76), whereas unsubstituted BODIPY exhibits weak singlet oxygen production (Φ_Δ ~ 0.06) [54]. Another systematic study [55] has documented the increase of the ISC rate constant for BODIPY scaffolds, incorporating iodine at the 2 and 6 positions to reach a rate of 18.3×10^{-8} s^{-1}, surpassing its equivalents with H, Kr, and Cl. This value is approximate since it is assumed that vibrational, rotational, or collisional deactivation of the S_1 state is negligible in frozen matrices (T = 77 K). A correlation between the heavy atom effect and the rate of generation of singlet oxygen was noticed, which is perfectly in line with theoretical predictions for the halogenation effect [55]. This correlation has also been shown to enhance hydrogen production in an experimental investigation [25] that aimed to assess the effectiveness of BODIPY compounds as photosensitizers. The study unveiled an increase in oxidation potential for iodinated dyads, which makes them active for H_2 production in acidic aqueous solutions [25] compared to BODIPY compounds bearing hydrogen as a substituent.

In 2005, Nagano synthesized 2,6-diiodoBODIPY [56] as a photosensitizer for photodynamic therapy, which can be considered one of the first investigations of the 2,6-diiodoBODIPY compound. The latter was characterized by strong visible light absorption (molar absorption coefficients $\varepsilon = 110\,000$ $M^{-1}.cm^{-1}$ at 535 nm) and a low fluorescence quantum yield ($\Phi_F = 0.02$ in methanol). Even though the triplet formation was not explicitly measured using nanosecond transient absorption spectroscopy, the previous results and the high singlet oxygen ($^1O_2$) yield indicate that the ISC process is efficient. Moreover, this compound exhibits low susceptibility to being oxidized, which reflects good stability compared to Rose Bengal.

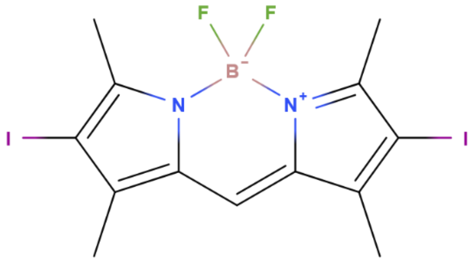

Figure 2.3: 2,6-DiiodoBODIPY as the organic triplet photosensitizer [56].

2.3 BODIPY dyes in photocatalytic H_2 evolution

Several studies have reported the integration of BODIPY dyes as photosensitizers in solar-to-hydrogen conversion systems; while some demonstrated good performance of the architecture, others observed poor or negligible efficiency:

Previous investigations [25] showed H_2 production of about 930 and 622 μmol after 6 hours of irradiation from halogenated BODIPY scaffolds bearing 8-hydroxyl-quinoline or phenylamine moiety at the meso-position, with cobaloxime as the catalyst and ascorbic acid as the electron donor in the acidic aqueous solutions. It reveals that in basic conditions, phenylamine functions as a donor and quenches the singlet or triplet BODIPY state intramolecularly, which relaxes to the ground state and hinders electron transfer to the catalyst, whereas in acidic solution, the protonation of the donor restricts intramolecular electron transfer and promotes an intermolecular pathway from phenylamine to the catalyst. This output exemplifies the effect of experimental conditions on H_2 formation. Similarly, Pat Sabatini [57] reported a turnover number of ~700 for a homogeneous photocatalytic system, with a BODIPY dye as the photosensitizer and triethanolamine (TEOA) as the SED in aqueous organic media. Such systems are likely to operate via the reduction of the excited state of PS, in which PS* is reduced by TEOA to form PS^-, followed by oxidative quenching involving electron transfer from PS^- to the catalyst. Quantum calculations reveal that the introduction of halogen stabilizes the HOMO and LUMO levels, which also prolongs the lifetime of the triplet states.

Dura et al. [58] succeeded in designing iodinated BODIPY dyes as photosensitizers in multicomponent catalytic systems with comparable activity to organometallics, very long-term stability by the introduction of a mesityl substituent, and maintaining functionality for more than 10 days. This compound exhibits a transition at 550 nm and an overall volume of H_2 produced higher than $[\{Pd(PPh_3)Cl_2\}_2]$ [58].

In reference [59], the incorporation of BODIPY units into a conjugated polymer backbone via intramolecular connection alters their excited-state behavior. Indeed, while the unsubstituted BODIPY unit has a conventional high fluorescence, the polymerized BODIPY dyes produce wider and red-shifted absorption with quenched fluorescence, where electron transfer occurs via a non-radiative process, manifested by high ISC quantum yield ($\Phi_{ISC} \approx 0.91$) and long-lived triplet state (lifetime ≈ 61 µs). Measurements reveal that this process is mediated by a single CT intermediate between the BODIPY chromophores and the conjugated backbone, which is stabilized in polar solvents and facilitates triplet formation. The resulting long-lived triplet state does not have a pure CT character; however, it is populated via a CT pathway. Under visible-light irradiation ($\lambda > 420$ nm), the BODIPY-based polymer acts as an efficient chromophore and exhibits a redox potential sufficient to transfer electrons to the catalyst (cobaloxime), thereby generating H_2 rates up to 319 µmol h^{-1} g^{-1} in THF/H_2O mixtures.

Another study [60] examines two assemblies for photocatalytic H_2 generation. Assembly 1 is a benzofuran[b]-annulated BODIPY bearing a thienyl-cyanoacrylic acid anchoring group, whereas assembly 2 is a non-fused cyanoacrylic acid–substituted BODIPY. Both function as photosensitizers in a heterogeneous system comprising TiO_2 as the electron conductor and platinum nanoclusters as catalytic sites for proton reduction. The fused structure of assembly 1 stabilizes the HOMO and LUMO levels and results in a red-shifted absorption (λ_{MAX} = 605 nm). TDDFT analysis assigns λ_{MAX} to a HOMO-LUMO transition from the BODIPY core to the binding group, which ensures an efficient electron transfer to TiO_2 and enhances photostability. In contrast, assembly 2 undergoes rapid photobleaching.

The authors of reference [61] reported that the BODIPY–cobaloxime complexes, in which the chromophore (BODIPY dye) and the cobaloxime catalytic unit are linked via a Co–N(pyridyl) coordination bond, showed no photocatalytic turnover for H_2. TDDFT calculations explained this: upon photoexcitation, the 8th singlet excited state (S_8) is populated, corresponding to a BODIPY-centered transition with electron density shifting from the BODIPY core to the pyridyl fragment. However, this state rapidly undergoes non-adiabatic decay into dissociative states, leading to rupture of the Co–N(pyridyl) bond. As a result, the complex falls apart instead of transferring electrons to cobalt, and no H_2 is produced photochemically.

Chapter 3: Literature Review on Quantum Methods

3.1 Basic concepts in quantum mechanics

The foundations of quantum physics were established around the turn of the 20th century, following a period during which macroscopic phenomena were sufficiently elucidated by classical physics. The dynamics of mechanical systems were successfully interpreted using Newton's equations, while phenomena such as diffraction and interference were described in terms of Maxwell's equations of electromagnetism. However, inconsistencies began to emerge when classical theories failed to align with certain experimental observations and their theoretical predictions. The first major theoretical failure was the inability to explain the spectral distribution of thermal radiation emitted by heated solids, a phenomenon commonly modeled as blackbody radiation [62]. To address the problem of energy divergence at high frequencies, Max Planck in 1900 proposed an empirical formula, assuming that electromagnetic energy could only be emitted or absorbed in discrete quanta $\mathrm{E} = \mathrm{nh}\nu$, where $\mathrm{h} \approx 6.626\times10^{-34}$ J.s is Planck's constant [63]. Building on Planck's work, Albert Einstein proposed that light itself consists of discrete energy packets, later termed photons. This hypothesis successfully explained the photoelectric effect, the energy of electrons ejected from a metal surface upon photoexcitation depends on the frequency of the incident light rather than its intensity [64]. Einstein demonstrated that quantization applies not only to light but also to atomic vibrations [65]. He employed this concept to explain the temperature-dependent behavior of the specific heat of solids, thereby emphasizing the fundamental significance of energy quantization within crystalline structures [66, 67]. Soon after, Niels Bohr introduced the concepts of quantized energy levels and angular momentum to explain the discrete spectral lines observed in the hydrogen atom [68]. His model addressed both the stability of atomic orbits and the observed line spectra by postulating that angular momentum is quantized, given by $\mathrm{L} = \mathrm{n}\hbar$, where $\hbar = \frac{\mathrm{h}}{2\pi}$ and n is a positive integer [69]. Later, Wilson and Sommerfeld extended Bohr's model by imposing semiclassical quantization conditions on each periodic degree of freedom through action integrals, known as the Wilson–Sommerfeld quantization conditions [70]. This extension enabled the description of electron motion as elliptical orbits and incorporated special relativistic effects, resulting in a more accurate description of the fine structure in the hydrogen spectrum [71].

In modern quantum mechanics [72], the first postulate asserts that every classical observable is represented by a Hermitian operator. When the latter acts on a wavefunction, it yields an eigenvalue that corresponds to a measurable physical quantity, which is inherently probabilistic. Operators that commute with the Hamiltonian are associated with conserved quantities.

In the non-relativistic Schrödinger picture for hydrogen-like systems [72], the relevant operators include the Hamiltonian $\widehat{H}$, the orbital angular momentum operator $\hat{L}^2$,the spin operator $\hat{S}^2$, and their projections $\hat{L}_z$ and $\hat{S}_z$ correspond to measurements of energy, orbital angular momentum, spin, and angular momentum projections along the z-axis. To elaborate further, the Schrödinger equation for hydrogen is analytically solvable due to the central Coulomb potential. The wavefunction can be separated into an independent set of second-order differential equations using spherical coordinates, which are: the radial part, which ensures the quantization of the energy levels, while the angular and azimuthal parts describe the shape and the orientation of the atomic orbitals [73]:

$$\Psi_{n,l,m_l}(r,\theta,\phi) \sim e^{-\frac{2Zr}{na_\mu}} \left(\frac{2Zr}{na_\mu}\right)^{l} L_{n-l-1}^{2l+1}\left(\frac{2Zr}{na_\mu}\right) P_l^{m_l}(\cos\theta) e^{i m_l \phi} \qquad \textbf{(3.1)}$$

The radial equation, solved using associated Laguerre polynomials, determines the distribution of the electron’s probability density with distance from the nucleus and imposes the condition $l < n$, where n is the principal quantum number, which determines the total number of nodes of the wavefunction $\Psi_{n,l,m_l}(r,\theta,\phi)$. The angular solutions which determine the shape of the atomic orbitals (s, p, d…) involve Legendre polynomials and impose the quantum condition $|m_l| < l$. In equation **(3.1)**, Z is the nuclear charge, $a_\mu = \frac{4\pi\varepsilon_0\hbar^2}{\mu e^2}$ with μ the reduced mass of the electron-nucleus system, l is the orbital angular momentum quantum number and m_l the magnetic quantum number.

For $l \neq 0$, the hyperfine perturbation, arising from the interaction between the electron's magnetic moment and either an external magnetic field or the magnetic dipole moment of the nucleus, leads to a splitting of the energy levels and thus effectively lifts their degeneracy.

When spin–orbit interaction is included as a perturbation, the total angular momentum operator $\mathrm{J} = \mathrm{L} + \mathrm{S}$ becomes relevant and the observables L and S are no longer associated with conserved quantities, thus new good quantum numbers are introduced J and $\mathrm{m_J}$, corresponding to the eigenvalues of $\hat{\mathrm{J}}^2$ and $\hat{\mathrm{J}}_z$. Indeed, when Lorentz invariance is imposed in the relativistic formalism, the symmetry structure is extended from rotational invariance to full Lorentz symmetry, so that only the total angular momentum $\hat{\mathrm{J}}$ is conserved [74].

While the Schrödinger equation provides exact solutions for hydrogen in the form of single-electron spin orbitals, these solutions also serve as a cornerstone for modeling the electronic configurations of multi-electron atoms. Indeed, the quantum numbers n ,l, $\mathrm{m_l}$ and $\mathrm{m_S}$ remain valid descriptors of atomic orbitals in polyelectronic atoms. However, these quantum numbers are only approximate, because in real atoms the instantaneous electron–electron interactions break the spherical symmetry of the Coulomb potential assumed in the non-interacting model.

Electron configurations describe the distribution of electrons in an atom or molecule as a set of filled orbitals. At this stage, all orbitals characterized by the same quantum number n and l remain degenerate regardless of the quantum number $\mathrm{m_l}$. The primitive intuition for determining the ground state orbital is provided by the Aufbau principle [75], which proposes that orbitals are filled in order of increasing n, with electrons with higher l (within the same n) occupying the slightly higher sublevel. This rule takes into consideration the Pauli exclusion principle, which asserts that fermions that have an identical set of quantum numbers cannot occupy the same orbital sublevel. The Madelung rule introduces an improvement by assuming that the orbitals are filled in increasing $\mathrm{n} + \mathrm{l}$ order, starting from the smallest value of n. However, some cases [76] are not handled by the Madelung rule, such as chromium and copper, whose 3d levels are filled with 5 and 10 electrons, respectively. This anomaly is due to the overlooking of spin-orbit coupling, which arises from relativistic effects where n and l are no longer good quantum numbers (they do not commute with the total Hamiltonian). Another shortcoming of the Madelung rule is that it does not account for the stability of the structure, whereas Hund’s rule addresses this by predicting that, within a given subshell, electrons are primarily distributed singly among the degenerate orbitals with parallel spins, then paired up. This configuration tends to maximize spin multiplicity. For configurations with parallel spins, the spatial wavefunctions are antisymmetric; hence, electrons avoid each other and the electron–electron repulsion decreases [77]. However, a recent study emphasizes that the key factor for this decrease is increased electron–nuclear attraction caused by orbital contraction and enhanced penetration toward the nucleus in the high-spin state [78], which leads to a more stable electronic configuration. In the case of molecular oxygen (O_2), the presence of two unpaired electrons in antibonding orbitals explains its paramagnetism, a feature predicted by Hund’s rule. These principles not only determine atomic ground states but also underpin the arrangement of the elements in the periodic table and provide a foundation for theories of chemical bonding [79].

In general, the electronic configuration can be expressed using a mathematical formalism known as the Slater determinant [72, 80]. This formalism ensures an antisymmetric construction with respect to the exchange of electrons, thereby satisfying the Pauli exclusion principle. Each Slater determinant corresponds to a unique electronic configuration; however, the reverse is not necessarily true. Indeed, electronic configurations that exhibit degeneracy, such as those with partially filled orbitals, must be described by a linear combination of single Slater determinants in order to provide an accurate representation of the system.

$$\Psi(x_1, \ldots, x_N) = \frac{1}{\sqrt{N!}} \begin{vmatrix} \psi_1(x_1) & \psi_2(x_1) & \cdots & \psi_N(x_1) \\ \psi_1(x_2) & \psi_2(x_2) & \cdots & \psi_N(x_2) \\ \vdots & \vdots & & \vdots \\ \psi_1(x_N) & \psi_2(x_N) & \cdots & \psi_N(x_N) \end{vmatrix}. \quad \textbf{(3.2)}$$

While Hund’s rules provide a fundamental understanding of electron spin configurations and multiplicity in atomic and simple molecules, particularly for determining the ground state, they are insufficient for predicting the physical properties of molecular structures such as orbital energies and electron delocalization. The Hückel Molecular Orbital theory offers a first step beyond Hund’s qualitative framework by introducing a tight-binding approximation specific to π-electrons in conjugated planar molecules. By entirely neglecting electron–electron interactions due to their intractable nature and applying the variational method, Hückel effectively reduces the many-electron Schrödinger equation to a one-electron eigenvalue problem for π molecular orbitals [62]. Despite its simplicity, the Hückel method successfully captures key qualitative features of conjugated systems, offering insight into aromaticity, π-electron delocalization, and the resonance character of the molecule. To refine this approximation, the Pariser–Parr–Pople method extends the Hückel framework by partially incorporating electron–electron repulsion [81]. This is achieved by including the influence of inner-shell electrons through an effective core potential, analogous to the concept of screening in atomic structure, wherein the valence π-electrons move within a smeared-out potential generated by both the nucleus and inner electrons. All of these approximations, including more sophisticated extensions, are formulated within the framework of the Born–Oppenheimer approximation.

3.2 Born–Oppenheimer approximation

The fourth postulate of quantum mechanics states that the time-dependent Schrödinger equation describes how the quantum state of a system evolves over time. It is written as,

$$i\hbar\frac{\partial}{\partial t}\left|\Psi\left(t,\vec{r},\vec{R}\right)\right\rangle = \widehat{\mathcal{H}}\left|\Psi\left(t,\vec{r},\vec{R}\right)\right\rangle \qquad \textbf{(3.3)}$$

where $\widehat{\mathcal{H}}$ is the hermitian Hamiltonian operator corresponding to the exact total energy of the system, accounting for all particles and their interactions. The state vector $\Psi\left(t,\vec{r},\vec{R}\right)$ represents the time-dependent wavefunction of the system, containing all information about the quantum state as a function of time t, of electronic coordinates $\vec{r}$ and of nuclear coordinates $\vec{R}$.

In molecular systems, the wavefunction evolves in a stationary manner, multiplied by a time-dependent phase factor that does not affect observable quantities such as position, momentum, or energy. Consequently, the time-independent Schrödinger equation can be expressed as:

$$\widehat{\mathcal{H}}\left|\Psi\left(\vec{r},\vec{R}\right)\right\rangle = E_{tot}\left|\Psi\left(\vec{r},\vec{R}\right)\right\rangle \qquad \textbf{(3.4)}$$

In equation **(3.4)**, E_{tot} denotes the total energy of the system.

The non-relativistic Hamiltonian for a system of electrons and nuclei can be expressed in atomic units as:

$$\begin{aligned}\widehat{H} &= \widehat{T}_e + \widehat{T}_n + \widehat{V}_{ne} + \widehat{V}_{ee} + \widehat{V}_{nn}\\ &= \widehat{T}_e + \widehat{T}_n + V(\vec{r},\vec{R})\\ &= -\sum_{i=1}^{N}\frac{1}{2}\nabla_i^2 - \sum_{A=1}^{M}\frac{1}{2M_A}\nabla_A^2 - \sum_{i=1}^{N}\sum_{A=1}^{M}\frac{Z_A}{r_{iA}} + \sum_{i=1}^{N}\sum_{j>i}^{N}\frac{1}{r_{ij}} + \sum_{A=1}^{M}\sum_{B>A}^{M}\frac{Z_A Z_B}{R_{AB}}\end{aligned} \qquad \textbf{(3.5)}$$

In the preceding equation **(3.5)**, Z_A denotes the atomic number of nucleus A and M_A its mass as a ratio to the electron mass. The operators ∇_A^2 and ∇_i^2 are Laplacians with respect to the coordinates of the A-th nucleus and the i-th electron, respectively. The Hamiltonian consists of five terms, listed from left to right: $\widehat{T}_e$, the kinetic energy operator of the electrons; $\widehat{T}_n$, the kinetic energy operator of the nuclei; $\widehat{V}_{ne}$, the Coulomb attraction between electrons and nuclei; and $\widehat{V}_{ee}$, $\widehat{V}_{nn}$ represent the Coulomb repulsion between electrons and between nuclei, respectively.

The Born-Oppenheimer approach (BO) [82] aims to provide an approximate solution to the Schrödinger equation for systems with multiple degrees of freedom. The BO ansatz introduces a separation between nuclear and electronic motion, based on the fact that electrons move much faster than nuclei. As a result, the electronic configuration adjusts instantaneously to changes in nuclear positions. The total wavefunction is expanded in terms of a complete, orthogonal set of electronic eigenstates $\psi_i(\vec{r},\vec{R})$ that depend parametrically on the nuclear coordinates $\vec{R}$. The expansion coefficients are proportional to the nuclear wavefunction $\Phi_{n,i}(\vec{R})$, which describes vibrational and rotational motion.

$$\left|\Psi(\vec{r},\vec{R})\right\rangle = \sum_{i=1}^{\infty} \left|\Phi_{n,i}(\vec{R})\right\rangle \left|\psi_i(\vec{r},\vec{R})\right\rangle \quad \textbf{(3.6)}$$

For a stationary nuclear position $\vec{R}$, the electronic Hamiltonian can be solved by treating the nuclear kinetic energy as a constant.

$$(\widehat{T}_e + V(\vec{r},\vec{R})\left|\psi_i(\vec{r},\vec{R})\right\rangle = E_i(\vec{R})\left|\psi_i(\vec{r},\vec{R})\right\rangle; i = 1,2,\ldots,\infty \quad \textbf{(3.7)}$$

$E_i(\vec{R})$ corresponds to the electronic energy of the system in the state labeled by the electronic quantum number i.

This relation ensures the orthogonality of the electronic states, expressed as:

$$\int \psi_i^*(\vec{r},\vec{R})\psi_j(\vec{r},\vec{R})d\vec{r} = \delta_{ij} \quad \textbf{(3.8)}$$

At this stage, the total wavefunction expression is plugged into the Schrödinger equation in order to determine the nuclear equation:

$$\sum_{i=1}^{\infty} (\widehat{T}_e + \widehat{T}_n + V(\vec{r},\vec{R}))\left|\Phi_{n,i}(\vec{R})\right\rangle\left|\psi_i(\vec{r},\vec{R})\right\rangle = E_{tot}\sum_{i=1}^{\infty} \left|\Phi_{n,i}(\vec{R})\right\rangle\left|\psi_i(\vec{r},\vec{R})\right\rangle \quad \textbf{(3.9)}$$

The nuclear Laplacian with respect to nucleus A distributes over the product $\Phi_{n,i}(\vec{R})\psi_i(\vec{r},\vec{R})$ as follows:

$$\nabla_A^2\left(\Phi_{n,i}(\vec{R})\psi_i(\vec{r},\vec{R})\right) = \Phi_{n,i}(\nabla_A^2\psi_i) + 2(\nabla_A\Phi_{n,i})\cdot(\nabla_A\psi_i) + (\nabla_A^2\Phi_{n,i})\psi_i \quad \textbf{(3.10)}$$

We multiply equation **(3.9)** from the left by $\psi_j^*(\vec{r},\vec{R})$ and integrate over the electronic coordinates. Taking into account the orthonormality of the wavefunctions, this yields:

$$\hat{T}_n\Phi_{n,j} + E_j\Phi_{n,j} + \sum_{i=1}^{\infty} U_n^{i,j} = E_{tot}\Phi_{n,j} \qquad \textbf{(3.11)}$$

The term $U_n^{I,j}$ describes the coupling between electronic wavefunctions. These couplings are known as the first $(2\langle\psi_j|\nabla_A|\psi_i\rangle(\nabla_A\Phi_{n,i}))$ and second $(\langle\psi_j|\nabla_A^2|\psi_i\rangle\Phi_{n,j})$ non-adiabatic matrix elements, corresponding to the cases where $i \neq j$.

Within the adiabatic approximation, each molecular wavefunction is confined to a single potential energy surface. Thus, only the diagonal terms $(i = j)$ of the coupling matrix contribute, which implies that the first-order non-adiabatic coupling terms vanish, assuming no spatial degeneracy between the electronic states.

$$(\hat{T}_n + E_j + \langle\psi_j|\nabla_A^2|\psi_i\rangle)\Phi_{n,j} = E_{tot}\Phi_{n,j} \qquad \textbf{(3.12)}$$

In the BO approximation, the nuclei are much heavier than the electrons. As a result, the second derivative of the electronic wavefunction with respect to the nuclear coordinates $\vec{R}$ is neglected.

The resulting nuclear Schrödinger equation is:

$$\left(\hat{T}_n + E_j(\vec{R})\right)\Phi_{n,j}(\vec{R}) = E_{tot}\Phi_{n,j}(\vec{R}) \qquad \textbf{(3.13)}$$

This equation describes the motion of the nuclei on a restricted PES associated with the electronic state j. The function $\Phi_{n,j}$ represents the nuclear wavefunction, and its solutions correspond to quantized vibrational and rotational energy levels of the molecule; typically, the vibrational states are obtained within the harmonic oscillator approximation near the equilibrium geometry. The electronic Schrödinger equation determines the electron distribution and the PES at each stationary position $\vec{R}$.

Despite being a foundational paradigm for variational and approximate quantum chemical methods, facilitating the calculation of molecular properties such as structural optimization, vibrational frequencies, and excited-state characteristics for modern chemistry and enabling the determination of the exact Schrödinger solution for H_2^+ and one electron system [83], the BO approximation has inherent limitations. The adiabatic approach begins to fail when two electronic states (i.e., solutions to the electronic Schrödinger equation) become degenerate, resulting in an intersection or near-intersection of their corresponding PES. This breakdown, often observed in regions of strong non-adiabatic coupling, can be mitigated through the use of diabatic representations, such as the Mulliken–Hush diabatization scheme [84]. Furthermore, the BO approximation encounters significant challenges when applied to continuum states, where the assumptions underlying the separation of nuclear and electronic motion no longer hold [85].

3.3 Hartree-Fock method

Hartree–Fock theory (HF) is a variational approach that typically yields moderately reliable electronic-structure predictions [86] and serves as a baseline for more advanced electronic structure methods [87, 88]. However, it is generally outperformed by Density Functional Theory in terms of accuracy and computational demands [62, 89].

3.3.1 Variational method

The variational approach [82] is a fundamental method in quantum mechanics [90], although it is not universally applicable to all approximation schemes (MP2, CC). It states that the energy of a trial wavefunction should be higher than or equal to the exact ground state energy, regardless of whether the ground state is degenerate or non-degenerate. This principle ensures that the estimated energy does not diverge to unphysical values, such as infinity. In contrast to perturbative methods, wherein the correction of the reference state in highly perturbed systems can be problematic, the bound nature of the variational method enables a systematic improvement of the wavefunction to obtain a better estimation of the energy.

3.3.2 Hartree-Fock methodology

Whereas Hückel theory [82, 88] neglect electron-electron interactions to solve the Schrödinger equation, the Hartree approximation includes these interactions in an average way. It simplifies the many-electron wave function into a product of spin orbitals with decoupled degrees of freedom, where each electron moves in an average potential field created by the other electrons $\mathrm{i} \neq \mathrm{j}$:

$$\Psi^{\mathrm{Hartree}}(\mathrm{x}_1, \mathrm{x}_2, \dots, \mathrm{x}_\mathrm{N}) = \psi_\mathrm{i}(\mathrm{x}_1)\psi_\mathrm{j}(\mathrm{x}_2) \cdots \psi_\mathrm{k}(\mathrm{x}_\mathrm{N}) \tag{3.14}$$

In the first step, a non-interacting system is considered, in which the total Hamiltonian can be separated into a sum of single-electron Hamiltonians. This approximation ensures the feasibility of the Hartree method:

$$\hat{H} = \sum_{i=1}^{N} \hat{H}(i) \tag{3.15}$$

Here, the spin orbitals $\{\psi_j(x_i)\}$ form a set of eigenfunctions of the one-electron Hamiltonian $\hat{H}(i)$, such that :

$$\hat{H}(i)\psi_j(x_i) = \varepsilon_j \psi_j(x_i) \tag{3.16}$$

Thus, the total energy of a system with N electrons is given by: $E_{TOT} = \sum_j^N \varepsilon_j$

A key weakness of equation **(3.14)** is that it violates the Pauli exclusion principle, which requires the total spin–orbital wavefunction to be antisymmetric with respect to the exchange of any two electrons. While the spatial part of the wavefunction may be symmetric, the full wavefunction, including spin, must be antisymmetric to accurately describe fermions such as electrons, equation **(3.2)**.

Although the HF method is generally formulated for multi-electron systems, it is often first illustrated using the hydrogen molecule (H_2) due to the simplicity of the Slater determinant in this case [91]. In this context, we consider only electronic motion, under the BO approximation in atomic units,

$$\begin{aligned}\hat{H} &= \left(-\frac{1}{2}\nabla_1^2 - \sum_A \frac{Z_A}{r_{1A}}\right) + \left(-\frac{1}{2}\nabla_2^2 - \sum_A \frac{Z_A}{r_{2A}}\right) + \frac{1}{r_{12}} \\ &= \hat{H}(1) + \hat{H}(2) + \frac{1}{r_{12}}\end{aligned} \tag{3.17}$$

where $\hat{H}(1)$ is the operator related to the kinetic energy of electron 1 and its electrostatic interaction with nuclei, and $\frac{1}{r_{12}}$ is the electron–electron repulsion operator.

The first step is the evaluation of the average energy in the ground state $\langle\Psi_0|\hat{H}|\Psi_0\rangle$:

$$\begin{gathered}\langle\Psi_0|\hat{H}(1)|\Psi_0\rangle = \langle\Psi_0|\hat{H}(2)|\Psi_0\rangle \\ = \int dx_1 dx_2 \left[\frac{1}{\sqrt{2}}\left(\psi_1(x_1)\psi_2(x_2) - \psi_2(x_1)\psi_1(x_2)\right)\right]^* \hat{H}(1) \left[\frac{1}{\sqrt{2}}\left(\psi_1(x_1)\psi_2(x_2) - \psi_2(x_1)\psi_1(x_2)\right)\right]\end{gathered} \tag{3.18}$$

Evolving the expression and integrating over x_2 results in the elimination of some terms (either 1 or 0) due to the orthogonality of the orbitals. Thus:

$$\langle\Psi_0|\hat{H}(1)|\Psi_0\rangle = \int dx_1\psi_1^*(x_1)\hat{H}(1)\psi_1(x_1) + \int dx_1\psi_2^*(x_1)\hat{H}(1)\psi_2(x_1) \tag{3.19}$$

The evaluation of the expectation value of the operator r_{12}^{-1} yields:

$$\begin{aligned}\langle\Psi_0|r_{12}^{-1}|\Psi_0\rangle &= \int dx_1dx_2\left[\frac{1}{\sqrt{2}}\big(\psi_1(x_1)\psi_2(x_2) - \psi_2(x_1)\psi_1(x_2)\big)\right]^* r_{12}^{-1}\left[\frac{1}{\sqrt{2}}\big(\psi_1(x_1)\psi_2(x_2) - \psi_2(x_1)\psi_1(x_2)\big)\right]\\ &= \frac{1}{2}\int dx_1dx_2\{\psi_1^*(x_1)\psi_2^*(x_2)r_{12}^{-1}\psi_1(x_1)\psi_2(x_2) + \psi_2^*(x_1)\psi_1^*(x_2)r_{12}^{-1}\psi_2(x_1)\psi_1(x_2)\\ &\quad -\psi_1^*(x_1)\psi_2^*(x_2)r_{12}^{-1}\psi_2(x_1)\psi_1(x_2) - \psi_2^*(x_1)\psi_1^*(x_2)r_{12}^{-1}\psi_1(x_1)\psi_2(x_2)\}.\end{aligned} \tag{3.20}$$

Since the electrons are indistinguishable and $r_{12} = r_{12}$, interchanging the integration variables x_1 and x_2 demonstrates that the first and second terms are equal, as are the third and fourth terms. This results in a simplification of the equation **(3.20)**:

$$\begin{aligned}\langle\Psi_0|r_{12}^{-1}|\Psi_0\rangle = &\int dx_1dx_2\psi_1^*(x_1)\psi_2^*(x_2)r_{12}^{-1}\psi_1(x_1)\psi_2(x_2)\\ &-\int dx_1dx_2\psi_1^*(x_1)\psi_2^*(x_2)r_{12}^{-1}\psi_2(x_1)\psi_1(x_2)\end{aligned} \tag{3.21}$$

The first term, J_{12}, is the Coulomb integral, which represents the classical electrostatic repulsion between the charge distributions of electrons 1 and 2, while the second term K_{12} is the exchange integral, which arises from the exchange of electrons in the Slater determinant expansion. It enforces that two electrons with the same spin cannot occupy the same spatial orbital, serving as a correction to the Coulomb interaction due to the Pauli exclusion principle. Thus, the total energy of the H_2 molecule can be expressed as:

$$E = 2H_{11} + J_{12} - K_{12} \tag{3.22}$$

This expression can be extended to a closed-shell molecule with 2n electrons:

$$E = 2\sum_{i=1}^{n} H_{ii} + \sum_{i=1}^{n}\sum_{j=1}^{n}\left(2J_{ij} - K_{ij}\right) \tag{3.23}$$

For a doubly occupied spatial orbital I, $2H_{ii}$ is the sum of the electronic kinetic energy and the electron–nucleus potential energy contributed by the two electrons of opposite spin (α and β) in that orbital. The factor $2J_{ij}$ is the Coulomb repulsion between the charge densities of the electrons (1 and 2) occupying the spatial orbitals $\psi_i(1)$ and $\psi_j(2)$. The energy expression does not sum over individual electron pairs; instead, it integrates over continuous electron densities, so each electron interacts with the averaged charge cloud of the other occupied orbital, equation **(3.21)**. K_{ij} represents the exchange energy that arises from the antisymmetric character of the many-electron wavefunction; it has no classical analogue.

A quantum system naturally favors stability, with its electronic configuration filled from the lowest energy state upwards. Since the total energy of an approximate wavefunction is typically too high, minimizing the expectation value of the Hamiltonian provides an upper bound for the exact ground state energy. The average energy is minimized with respect to the molecular orbitals ψ or the atomic orbital coefficients, under the constraint that orbital orthogonality is preserved [62]. This can be achieved by introducing Lagrange multipliers, where S_{ij} represents the overlap between orbitals i and j (i.e., S_{ij}, typically 0 or 1 for orthonormal orbitals). The constraint is expressed in the Lagrangian formalism as:

$$\mathcal{L} = E + \sum_{i=1}^{n} \sum_{j=1}^{n} L_{ij}\left(S_{ij} - \delta_{ij}\right) = \text{constant}. \tag{3.24}$$

Upon performing the variational minimization with respect to the molecular orbitals and then diagonalizing the resulting matrix, the calculation yields a set of pseudo-eigenvalue equations. These are referred to as pseudo-eigenvalue equations because the Hartree-Fock operator depends on the orbitals upon which it acts, making the problem inherently nonlinear and self-consistent.

$$\hat{F}\psi_i(1) = \varepsilon_i \psi_i(1) \tag{3.25}$$

The Fock operator $\hat{F}(1)$ in the HF formalism acts on the spin orbital $\psi_i(1)$, where (1) refers to the coordinates of electron 1, which occupies the orbital ψ_i. It can be expressed in terms of the one-electron Hamiltonian $\hat{h}(1)$, the Coulomb operators $\hat{J}_j(1)$, and the exchange operators $\hat{K}_j(1)$.

$$\hat{F}(1)\psi_i(1) = \hat{h}(1)\psi_i(1) + \sum_{j=1}^{n} \left[\hat{J}_j(1)\psi_i(1) - \hat{K}_j(1)\psi_i(1)\right] \tag{3.26}$$

The operators are explicitly written as:

$$\hat{h}(1)\psi_i(1) = \left(-\frac{1}{2}\nabla_1^2 - \sum_{A} \frac{Z_A}{r_{1A}}\right)\psi_i(1) \tag{3.27}$$

$$\hat{J}_j(1)\psi_i(1) = \left[\int \psi_j^*(2)\frac{1}{r_{12}}\psi_j(2)dx_2\right]\psi_i(1) \tag{3.28}$$

$$\hat{K}_j(1)\psi_i(1) = \left[\int \psi_j^*(2)\frac{1}{r_{12}}\psi_i(2)dx_2\right]\psi_i(1) \tag{3.29}$$

In principle, the molecular orbitals and their energies can be determined iteratively, based on equation **(3.26)**. The process begins with an initial guess for the orbitals, which serves as the zeroth approximation. The Fock operator is applied to this guess to calculate the corresponding energy, from which improved orbitals are obtained. These updated orbitals are then reintroduced into the Fock operator to yield successive values of the energies ε_I and orbitals ψ_i. This cycle continues until the values of ε and ψ no longer change.

In the restricted configuration approach, there are n molecular orbitals used to describe $2n$ electrons, where each molecular orbital can be expressed as a linear combination of m atomic orbitals. These atomic orbitals are typically centered on the nuclei, normalized, and linearly independent, but they are generally not orthogonal to one another.

Each molecular orbital ψ_I is written as:

$$\psi_i = \sum_{s=1}^{m} c_{si}\phi_s \tag{3.30}$$

Substituting the molecular orbital expansion into the set of Fock equations, and then multiplying each resulting equation on the left by ϕ_r^* for $r = 1, \ldots, m$, followed by integration over all electronic coordinates, yields a set of $m*m$ equations,

$$\sum_{s=1}^{m} c_{si}F_{rs} = \sum_{s=1}^{m} c_{sn}S_{rs}\varepsilon_i \tag{3.31}$$

where $i = 1, \ldots, m$ corresponds to each molecular orbital level.

The Fock matrix elements and overlap integrals are given by:

$$F_{rs} = \int \Phi_r^*\hat{F}\phi_s dx_1 \text{ and } S_{rs} = \int \Phi_r^*\phi_s dx_1 \tag{3.32}$$

Given a well-defined atomic-orbital basis set, solving the HF equations provides the molecular orbital coefficients (and their associated orbital energies), and then the resulting wavefunction can be used to calculate various molecular properties.

A key drawback of the generalized eigenvalue equation is that it does not follow the standard form. Since the atomic basis functions are not orthonormal (being centered on different nuclei), the overlap matrix S must be orthogonalized,

$$HC = SC\varepsilon \overset{\text{orthogonalization}}{\rightarrow} H'C' = C'\varepsilon \tag{3.33}$$

with $C' = S^{\frac{1}{2}}C$ and $S^{-\frac{1}{2}}HS^{-\frac{1}{2}} = H'$. However, computing $S^{-\frac{1}{2}}$ directly is non-trivial. Instead, S is diagonalized as $S = PDP^{-1}$, where P is the eigenvector matrix and D is diagonal.

The Fock matrix elements F_{rs} depend on the molecular orbitals ψ_I, and thus on the coefficients C and the atomic basis functions ϕ_r. The explicit form is:

$$F_{rs} = \langle \phi_r(1)|\hat{H}^{core}(1)|\phi_s(1)\rangle + \sum_{j=1}^{n} \left[2\langle \phi_r(1)|\hat{J}_j(1)|\phi_s(1)\rangle - \langle \phi_r(1)|\hat{K}_j(1)|\phi_s(1)\rangle\right] \quad \textbf{(3.34)}$$

The first term is not changed since it contains only the kinetic energy operator, the nuclear charges, and the coordinates of the electron, whereas the second and the third terms can be extended by replacing each molecular orbital ψ_I by its linear combination of atomic orbitals ϕ_I (equation **(3.30)**) in equations **(3.28)** and **(3.29)**, this yields:

$$\langle \phi_r(1)|\hat{J}_j(1)|\phi_s(1)\rangle = \sum_{t=1}^{m} \sum_{u=1}^{m} c_{tj}^{*} c_{uj} \int\int \frac{\phi_r^{*}(1)\phi_s(1)\phi_t^{*}(2)\phi_u(2)}{r_{12}} dx_1 dx_2 \quad \textbf{(3.35)}$$

$$\langle \phi_r(1)|\hat{K}_j(1)|\phi_s(1)\rangle = \sum_{t=1}^{m} \sum_{u=1}^{m} c_{tj}^{*} c_{uj} \int\int \frac{\phi_r^{*}(1)\phi_u(1)\phi_t^{*}(2)\phi_s(2)}{r_{12}} dx_1 dx_2 \quad \textbf{(3.36)}$$

These terms **(3.35)** and **(3.36)** are called two-electron integrals over molecular orbitals and involve four basis functions centered on the nuclei.

By substituting the latter terms into expression **(3.31)**, one obtains the Roothaan equation **(3.37)**, which serves as the principal framework for optimizing molecular structures and estimating the system's minimum total energy. After supplying the program with a proposed set of basis functions, each integral in the Fock matrix F_{rs} is computed. Subsequently, the orthogonalization of the overlap matrix is performed, leading to the formulation of the standard eigenvalue problem F'_{rs} (equation **(3.33)**). Diagonalizing F'_{rs} yields an initial approximation of the energy eigenvalues and the corresponding eigenvectors. If the resulting density matrix differs from the initial guess, the procedure is iterated until self-consistency is achieved and convergence is reached.

$$F_{rs} = H_{rs}^{core}(1) + \sum_{t=1}^{m} \sum_{u=1}^{m} P_{tu} \left[(rs|tu) - \frac{1}{2}(ru|ts)\right] \quad \textbf{(3.37)}$$

In equation **(3.37)**, P_{tu} is the density matrix.

Geometry optimization can yield misleading results when a saddle point on the PES is mistakenly identified as a minimum. To correctly characterize stationary points, it is essential to evaluate both the gradient (e.g., root-mean-square force) and the Hessian matrix. At the HF level, this involves differentiating the Roothaan equations with respect to nuclear coordinates or expansion coefficients, using the Hellmann–Feynman theorem to compute the forces.

$$g^{H-F} = \left\langle \Psi \left| \frac{\partial F_{rs}}{\partial R_A} \right| \Psi \right\rangle \tag{3.38}$$

Equation **(3.38)** yields the contribution to the force acting on nucleus A, while the second derivative,

$$H = \frac{\partial^2 F_{rs}}{\partial R_A^2} > 0 \tag{3.39}$$

It enters the electronic part of the total Hessian matrix. This second derivative is critical for vibrational analysis and for verifying that a stationary point corresponds to a true energy minimum rather than a saddle point.

Several iterative methods exist to update nuclear coordinates for energy minimization on the PES [82]. The Quasi-Newton method (QN), often implemented within a Raphson-type framework, is a prominent example. It constructs an approximate local quadratic model of the PES around the current geometry using data from previous iterations (energy, gradient and often an approximate Hessian matrix). This model predicts the step displacement $\Delta R_A = -H_k^{-1} g_k^{H-F}$ towards the estimated minimum. While QN methods are highly efficient in terms of convergence rate near the minimum and generally more accurate than simpler methods due to their use of curvature information, they are computationally more expensive per iteration than the Steepest Descent method. This expense arises primarily from the need to build, update, and invert (or solve linear equations involving) the Hessian approximation.

3.4 Basis set

A molecule consists of atoms bonded together. When isolated, atoms occupy atomic orbitals, and their electron configurations follow Hund’s rule and the Aufbau principle. When atoms combine, their atomic orbitals overlap and interact. This interaction leads to constructive interference (forming bonding molecular orbitals) and destructive interference (forming antibonding molecular orbitals). The wavefunctions of atomic orbitals, which describe the electronic behavior of electrons within a specific physical system, are explicitly represented by mathematical functions known as basis sets. The latter are used to approximate the molecular orbitals.

The earliest basis sets in quantum chemistry were the eigenfunctions of the hydrogen-atom Hamiltonian, chosen for their analytical simplicity. For elements in the first and second rows of the periodic table, these basis functions typically consist of hydrogen-like s and p orbitals [92]. One of the simplest models, the Hückel basis set, employs only p-type orbitals to construct π orbitals [82]. These functions, known as Slater-type orbitals, scale as:

$$\psi(\mathrm{r}) \propto \mathrm{e}^{-\zeta|\mathrm{r}-\mathrm{R_A}|} \quad \textbf{(3.40)}$$

where ζ is the Slater orbital exponent and $|\mathrm{r}-\mathrm{R}_A|$ is the distance of the electron from nucleus.

Although physically accurate, STOs functions present significant computational challenges, particularly in evaluating two-electron integrals. In 1950, Boys proposed replacing Slater-type orbitals with Gaussian-type orbitals of the form [93]:

$$\psi(\mathrm{r}) \propto \mathrm{e}^{-\alpha|\mathrm{r}-\mathrm{R_A}|^2} \quad \textbf{(3.41)}$$

The product of two Gaussians centered on different nuclei is itself a Gaussian, which simplifies the evaluation of molecular integrals. To overcome the limitations of Gaussian orbitals in describing the correct radial behavior, contracted Gaussian functions were introduced. These are linear combinations of primitive Gaussian functions with carefully chosen contraction coefficients, optimized to approximate the shape of Slater-type orbitals. For example, a single STO can be represented using several 1s Gaussian primitives with suitable contraction coefficients. These basis sets combine the computational efficiency of Gaussians with the physical accuracy of Slater orbitals.

The performance of a basis set attains high accuracy when it satisfies two conditions: (1) completeness to describe atomic orbital structures correctly, and (2) the ability to capture all physical effects influencing molecular orbitals (e.g., polarizability, electron affinity).

Basis sets can be classified into several groups:

STO-3G [62, 94] is a minimal basis set in which chemical bonding is described by a contracted Gaussian basis set formed from primitive Gaussian functions, all weighted with the same α exponent for both core and valence shells. Minimal basis sets lack the accuracy and flexibility to represent electron density distribution between nuclei in chemical bonds. To improve the self-consistent field (SCF) flexibility, the valence shell can be split into inner and outer components with different orbital exponents. For example, the STO for a $2s$ atomic orbital is written as:

$$\psi_{2s}(r) = \psi_{2s}^{STO}(r, \zeta_1) + \lambda\psi_{2s}^{STO}(r, \zeta_2) \tag{3.42}$$

where λ consists of the weight of the contribution.

Similarly, in a double-zeta basis set, each valence atomic orbital is represented by two basis functions with different orbital exponents: one more contracted and one more diffuse. This splitting increases the flexibility of the orbital description while still allowing a linear parametrization of the basis functions [56]. Beyond this, polarized basis sets are constructed by adding orbitals with higher angular momentum quantum numbers (l) to account for the distortion of electron density caused by bonding with other atoms. For example, adding a set of d functions to the 6-31G(d) basis set for carbon and oxygen improves the representation of molecular properties in alcohol-based molecules [95].

Moreover, species such as anions, hydrogen-bonded dimers, weakly bound supramolecular assemblies, and molecules containing lone electron pairs exhibit pronounced electron density at large distances from the nuclei [96]. To compute this, additional Gaussian functions with small exponents are included to slow the decay of the wavefunction far from the nuclei. This is indicated by "+" for heavy atoms only, and "++" for both heavy and hydrogen atoms (e.g., 6-31++G) [97]. For structures containing elements from the third row of the periodic table, evaluation of two-electron repulsion integrals can be tedious due to the large number of electrons. To simplify the simulation, a one-electron Fock operator is used to account for the average effect of core electrons on the valence electrons; this is known as an effective core potential basis set [98].

Large basis sets of triple- or quadruple-zeta type, such as def2-TZVP or def2-QZVP, offer superior accuracy by incorporating extensive polarization and diffuse functions, which allow for more precise modeling of electron distribution effects. However, they come with a significant increase in computational cost. Thus, their use is most justified when high precision is required [99].

3.5 Correlation energy

The HF method treats each electron as moving in the mean Coulomb field generated by all other electrons. While the exchange interaction, arising from the Pauli exclusion principle, incorporates correlation between electrons of the same spin (the Fermi hole), it omits the correlated motion of electron pairs, particularly those with opposite spin. The correlation energy can be defined as follows:

$$\mathrm{E_{corr}} = \mathrm{E_{exact}} - \mathrm{E_{HF}} \tag{3.43}$$

The impact of electron correlation can vary substantially depending on the electronic structure. For the N_2 molecule, it accounts for only about 0.5% of the total electronic energy at the ground-state equilibrium geometry, yet it contributes nearly 50% of the binding energy [100]. Improving upon the HF method requires understanding the distinct forms of correlation underlying these discrepancies.

Dynamical correlation stems from instantaneous Coulomb repulsion between electrons, and its magnitude decreases exponentially with increasing bond length [101]. Static correlation occurs when multiple quantum states have the same electronic energy but different quantum numbers (degenerate states). In such cases, HF cannot determine which state should be occupied, and its single-determinant description fails. Therefore, a multideterminant treatment is required. Static correlation commonly appears in bond dissociation [102], in d/f-block elements, block metallic elements [103] and the equilibrium geometries of systems such as acenes [104].

Transitioning from a closed-shell to an open-shell description via the unrestricted Hartree–Fock (UHF) method improves the treatment of near-degenerate systems and singlet diradicals. UHF allows α and β electrons to occupy different spatial orbitals, capturing correlation effects absent in restricted Hartree–Fock (RHF).

In the RHF approach, the electrons in H_2 are restricted to occupy the same bonding orbital, an assumption that works reasonably well near the equilibrium geometry but fails at dissociation, where strong static correlation becomes significant.

In the ground state of H_2, the paired electrons occupy the bonding molecular orbital,

$$\sigma = \frac{1}{\sqrt{2}}[\phi_\mathrm{A} + \phi_\mathrm{B}] \tag{3.44}$$

where ϕ_A and ϕ_B are the 1s type function on hydrogen A and B , respectively. The HF ground-state wavefunction ψ_0 is then constructed as a product of two such σ orbitals (one for each electron) and the singlet spin function:

$$\psi_0 = \frac{1}{\sqrt{2}}\sigma(\vec{r}_1)\sigma(\vec{r}_2)[\alpha(1)\beta(2) - \beta(1)\alpha(2)] \quad \textbf{(3.45)}$$

The spatial molecular part expands as:

$$\sigma(\vec{r}_1)\sigma(\vec{r}_2) = \frac{1}{2}\begin{bmatrix} \phi_A(\vec{r}_1)\phi_A(\vec{r}_2) + \phi_A(\vec{r}_1)\phi_B(\vec{r}_2) \\ +\phi_B(\vec{r}_1)\phi_A(\vec{r}_2) + \phi_B(\vec{r}_1)\phi_B(\vec{r}_2) \end{bmatrix} \quad \textbf{(3.46)}$$

The ionic terms $\phi_A(\vec{r}_1)\phi_A(\vec{r}_2)$ and $\phi_B(\vec{r}_1)\phi_B(\vec{r}_2)$ do indeed represent both electrons localized on the same atom, while the covalent terms $\phi_A(\vec{r}_1)\phi_B(\vec{r}_2)$ and $\phi_B(\vec{r}_1)\phi_A(\vec{r}_2)$ represent electrons on different atoms. Upon bond dissociation, the ionic terms become unphysical, leading to an overestimation of the energy within the HF approximation.

The correct dissociation limit of the singlet wavefunction is:

$$\frac{1}{2}[\phi_A(\vec{r}_1)\phi_B(\vec{r}_2) + \phi_B(\vec{r}_1)\phi_A(\vec{r}_2)][\alpha(1)\beta(2) - \beta(1)\alpha(2)] \quad \textbf{(3.47)}$$

In the UHF approach for H_2, the occupied orbitals for α and β-spin electrons are expressed as linear combinations of the RHF bonding and antibonding molecular orbitals [91]:

$$\begin{aligned} \psi^\alpha &= -\sin\theta\,\sigma_+ + \cos\theta\,\sigma_- \\ \psi^\beta &= \sin\theta\,\sigma_+ + \cos\theta\,\sigma_- \end{aligned} \quad \textbf{(3.48)}$$

Here θ is a variational parameter that determines the optimal mixing of bonding and antibonding orbitals to minimize the total UHF energy.

The orbital mixing described above allows UHF to capture static correlation effects, particularly in the dissociation limit. However, the resulting UHF wavefunction is generally not an eigenfunction of the total spin-squared operator $\hat{S}^2$, where S is the total spin angular momentum. As a result, the expectation value $< \hat{S}^2 >$ is typically larger than the value for a pure spin state, a phenomenon known as spin contamination. This contamination arises from the mixture with higher-spin components. To address this problem, projection operator techniques can be applied to the UHF wavefunction, yielding a spin-adapted form whose $< \hat{S}^2 >$ more closely matches the exact $S(S+1)\hbar^2$ result for the pure spin state [73].

3.6 MP2 correction

One of the earliest methods developed to account for dynamical electron correlation was introduced by Møller and Plesset in 1934 [105]. This approach, known as Møller–Plesset perturbation theory (MPn), applies Rayleigh–Schrödinger perturbation theory to the electronic Hamiltonian. The index n denotes the order of the perturbation, typically ranging from 2 to 6. In this framework, electron correlation is treated as a perturbative correction to the HF reference, allowing electrons to be excited from occupied to virtual molecular orbitals. These excitations enable a more accurate description of the electronic structure, as they reduce the electron-electron repulsion and stabilize the system. The total Hamiltonian is thus expressed as the sum of the unperturbed HF Hamiltonian, defined by the Roothaan equations, and a perturbative correction that captures correlation effects.

$$\hat{H} = \hat{H}_0 + \lambda \hat{H}_1 \qquad \textbf{(3.49)}$$

where λ is a scaling factor for the perturbative Hamiltonian $\hat{H}_1$. The zeroth order Hamiltonian operator $\hat{H}_0$ is considered to be the sum of one-electron Fock operators for non-interacting system:

$$\hat{H}_0 = \sum_{i}^{N} H_{ii} + \sum_{i}^{N} V^{HF}(i) \qquad \textbf{(3.50)}$$

When applied to the unperturbed HF wavefunction $\hat{H}_0$ yields the sum of the occupied orbital energies, equal to:

$$\hat{H}_0 \Psi^{(0)} = \sum_{i}^{occ} \varepsilon_i \Psi^{(0)} \qquad \textbf{(3.51)}$$

The zeroth-order energy, $E_0^{(0)}$, corresponds to the sum of the one-electron energies associated with the occupied spin orbitals.

$$E_0^{(0)} = \sum_{i}^{occ} \varepsilon_i \qquad \textbf{(3.52)}$$

However, this summation counts the electron–electron repulsion twice and therefore requires correction when evaluating the total HF energy.

In general, the perturbative correction can be expressed as:

$$\hat{H}_1 = \hat{H} - \hat{H}_0$$
$$\hat{H}_1 = \sum_{i}^{occ} \sum_{j>i}^{occ} \frac{1}{r_{ij}} - \sum_{i}^{occ} \sum_{j}^{occ} \left(J_{ij} - K_{ij}\right) \qquad \textbf{(3.53)}$$

The first-order correction to the energy is written as:

$$E_0^{(1)} = \langle \Psi_0 | \hat{H}_1 | \Psi_0 \rangle$$
$$= \left\langle \Psi_0 \left| \sum_{i<j} \frac{1}{r_{ij}} \right| \Psi_0 \right\rangle - \left\langle \Psi_0 \left| \sum_{i}^{occ} \sum_{j}^{occ} \left(J_{ij} - K_{ij}\right) \right| \Psi_0 \right\rangle \qquad \textbf{(3.54)}$$

Using the Slater–Condon rule for the exact electron–electron repulsion operator, the equation becomes:

$$\begin{aligned}E_0^{(1)} &= \frac{1}{2}\sum_{i,j}([ii|jj]-[ij|ji]) - \sum_{i,j}([ii|jj]-[ij|ji]) \\ &= -\frac{1}{2}\sum_{i,j}([ii|jj]-[ij|ji]) \\ &= -\frac{1}{2}V^{HF}\end{aligned} \quad \textbf{(3.55)}$$

where [ii|jj] is the Coulomb integral and [ij|ji] is the exchange integral.
Thus, the first-order energy correction in HF theory accounts for the electron–electron repulsion in a way that avoids double counting.

To account for electron correlation beyond the mean-field approximation, the method employs second-order Møller–Plesset (MP2) perturbation theory, which describes the contribution of configurations generated by the excitation of one or more electrons. In this framework, an excited Slater determinant is formed by substituting one or more occupied orbitals in the HF determinant with virtual orbitals. The second-order energy correction is then given by:

$$E_0^{(2)} = \sum_{a\neq 0}\frac{|\langle\Psi_0|\hat{H}_1|\Psi_a^{(0)}\rangle|^2}{E^{(0)}-E_a^{(0)}} \quad \textbf{(3.56)}$$

where $\Psi_a^{(0)}$ is a Slater determinant representing an excitation relative to Ψ_0.

According to Brillouin's theorem, the off-diagonal elements of the Fock matrix between the reference determinant and any singly excited determinant vanish. This occurs because the HF determinant is an eigenfunction of the Fock operator, and the molecular orbitals are orthonormal. Thus:

$$\langle\Psi_0|\hat{H}_1|\Psi_r^a\rangle = 0 \quad \textbf{(3.57)}$$

Consequently, MPn theory does not include contributions from singly excited configurations (whether singlet or triplet), as their coupling with the HF reference vanishes by Brillouin's theorem. In MP2, the first-order correction to the wavefunction, and thus the second-order correction to the energy, arises solely from doubly excitations, corresponding to simultaneous electron transitions from occupied orbitals i, j to virtual orbitals l, s.

The excited-state wavefunction is represented as a sum over doubly excited configurations:

$$\sum_{a\neq 0} \left|\Psi_a^{(0)}\right| = \sum_{i<j} \sum_{l<s} \left|\Psi_{ij}^{ls}\right| \tag{3.58}$$

where the summation is restricted such that each electron is counted only once.

Thus, the second correction is expressed as:

$$E_0^{(2)} = \sum_{i<j}^{occ} \sum_{l<s}^{vir} \frac{\langle \Psi_0|\hat{H}_1|\Psi_{ij}^{ls}\rangle\langle \Psi_{ij}^{ls}|\hat{H}_1|\Psi_0\rangle}{E_0 - E_{ij}^{ls}} \tag{3.59}$$

where $E_{ij}^{ls} = \varepsilon_l + \varepsilon_s - \varepsilon_i - \varepsilon_j$ denotes the orbital energy difference associated with an electronic transition from occupied orbitals i, j to virtual orbitals l, s, as approximated by Koopmans' theorem.

Using Dirac bra–ket notation for the antisymmetrized two-electron integrals, the second-order energy correction can be written as:

$$E_0^{(2)} = \sum_{i<J} \sum_{l<s} \frac{|< li|sj > - < lj|si > |^2}{\varepsilon_l + \varepsilon_s - \varepsilon_i - \varepsilon_j} \tag{3.60}$$

The overall MP2 energy is:

$$\begin{aligned} E_0^{MP2} &= E_0^{(0)} + E_0^{(1)} + E_0^{(2)} \\ &= -\frac{1}{2} V^{HF} + E_0^{(2)} \end{aligned} \tag{3.61}$$

A key limitation of MPn theory is its poor treatment of static correlation, such as the energy associated with homolytic bond dissociation into two radicals [88]. In such cases, the reference wavefunction is strongly multiconfigurational, and the correlation cannot be treated as a small perturbation. Even the description of dynamical correlation in open-shell systems can lead to significant spin contamination [106]. Moreover, because MPn methods are non-variational, the computed total energy may fall below the exact ground-state energy, yielding positive rather than consistently negative corrections. Finally, the computational cost increases steeply with perturbation order, rendering higher-order MPn methods computationally demanding.

3.7 Coupled cluster method

Coupled cluster (CC) theory was first developed in nuclear physics and later extended to quantum chemistry. Its key advantage is the ability to capture all types of electron correlation (single, double, triple, quadruple, etc), analogous to full configuration interaction (FCI) when all excitations are included. In CC theory, the wavefunction is expressed as an exponential expansion of a reference wavefunction, ensuring size extensivity with respect to the number of electrons[89], in contrast to FCI, which employs a linear combination of electronic configurations.

$$\Psi_{CC} = e^{\hat{T}}\psi_0 \tag{3.62}$$

The cluster operator is $\hat{T}$ a non-Hermitian excitation operator expressed using creation ($a^\dagger$) and annihilation (a) operators within the second quantization formalism, analogous to the harmonic oscillator framework.

$$\begin{aligned} \hat{T}_1\psi_0 &= \sum_{i}^{occ}\sum_{l}^{vir} t_i^l \psi_i^l \\ \hat{T}_2\psi_0 &= \sum_{i<j}^{occ}\sum_{l<s}^{vir} t_{ij}^{ls}\psi_{ij}^{ls} \end{aligned} \tag{3.63}$$

In equation **(3.63)**, t_i^l and t_{ij}^{ls} are the amplitudes for single and double excitations, respectively. It can be extended to higher excitation order in a similar way.

The $e^{\hat{T}}$ operator is given by the Taylor series:

$$e^{\hat{T}} = 1 + \hat{T} + \frac{1}{2}\hat{T}^2 + \frac{1}{6}\hat{T}^3 + \cdots = \sum_{k=0}^{\infty}\frac{1}{k!}\hat{T}^k \tag{3.64}$$

It can be expanded as :

$$\begin{aligned} e^{\hat{T}} = 1 + \hat{T}_1 + \left(\hat{T}_2 + \frac{1}{2}\hat{T}_1^2\right) + \left(\hat{T}_3 + \hat{T}_2\hat{T}_1 + \frac{1}{6}\hat{T}_1^3\right) \\ + \left(\hat{T}_4 + \hat{T}_3\hat{T}_1 + \frac{1}{2}\hat{T}_2^2 + \frac{1}{2}\hat{T}_2\hat{T}_1^2 + \frac{1}{24}\hat{T}_1^4\right) + \cdots \end{aligned} \tag{3.65}$$

The first term yields the reference HF state, while the second term accounts for all singly excited configurations. $\hat{T}_2$ and $\hat{T}_1^2$ correspond to simultaneous two-electron excitations and to disconnected doubly excitations arising from the product of two single excitations, respectively. $\hat{T}_3$ and $\hat{T}_2\hat{T}_1^2$ generate triple excitations, whereas $\hat{T}_4$ and $\hat{T}_3\hat{T}_1$ correspond to connected and disconnected quadruple excitations, respectively.

The time-independent Schrödinger equation, when applied to the coupled-cluster (CC) wavefunction, can be written as:

$$\hat{H}e^{\hat{T}}\psi_0 = Ee^{\hat{T}}\psi_0 \tag{3.66}$$

To determine the excitation amplitudes, the average total energy can be obtained through the variational principle, similar to the conventional HF approach.

$$E_{CC}^{var} = \frac{\langle \Psi_{CC} | \hat{H} | \Psi_{CC} \rangle}{\langle \Psi_{CC} | \Psi_{CC} \rangle} = \frac{\langle e^{\hat{T}} \psi_0 | \hat{H} | e^{\hat{T}} \psi_0 \rangle}{\langle e^{\hat{T}} \psi_0 | e^{\hat{T}} \psi_0 \rangle} \quad \textbf{(3.67)}$$

However, the calculations are tedious and complex for higher orders, involving many non-vanishing terms. An alternative way to simplify the expression is to project the coupled-cluster wavefunction onto the reference wavefunction and multiply by ψ_0^*:

$$\begin{aligned} E_{CC} &= \left\langle \psi_0 \left| \hat{H} \left(1 + \hat{T}_1 + \hat{T}_2 + \frac{1}{2} \hat{T}_1^2 \right) \right| \psi_0 \right\rangle \\ E_{CC} &= \langle \psi_0 | \hat{H} | \psi_0 \rangle + \langle \psi_0 | \hat{H} | \hat{T}_1 \psi_0 \rangle + \langle \psi_0 | \hat{H} | \hat{T}_2 \psi_0 \rangle + \frac{1}{2} \langle \psi_0 | \hat{H} | \hat{T}_1^2 \psi_0 \rangle \end{aligned} \quad \textbf{(3.68)}$$

According to Brillouin’s theorem equation **(3.57)**, the HF matrix elements between occupied and virtual orbitals vanish; hence, all term containing singly excitation $\langle \psi_0 | \hat{H} | \psi_i^a \rangle$ are zero. Moreover, expansions beyond $\hat{T}_2^2$ terminate due to the Slater–Condon rules. Although the singly excited contribution does not appear explicitly in E_{CC}, it is implicitly included through orbital relaxation effects [107].

Thus, the remaining contributions are the non-correlated energy and the correlation from double excitations.

$$E_{CC} = E_0 + \sum_{i<j}^{occ} \sum_{a<b}^{vir} \left(t_{ij}^{ab} + t_i^a t_j^b - t_i^b t_j^a \right) \langle \psi_0 | \hat{H} | \psi_{ij}^{ab} \rangle \quad \textbf{(3.69)}$$

Even after simplification, the excitation amplitudes remain unknown. To determine their values, Jiří Čížek [108] proposed projecting the Schrödinger equation onto the complete set of excited determinants, encompassing all types of excited states. Prior to this, the HF energy is assumed to be an eigenvalue of the similarity-transformed hermitian Hamiltonian $e^{-\hat{T}} \hat{H} e^{\hat{T}}$. This procedure leads to a set of linear algebraic equations:

$$\begin{gathered} \langle \psi_0 | e^{-\hat{T}} \hat{H} e^{\hat{T}} | \psi_0 \rangle = E \langle \psi_0 | \psi_0 \rangle = E \\ \langle \Phi_i^a | e^{-\hat{T}} \hat{H} e^{\hat{T}} | \Phi_0 \rangle = E \langle \psi_i^a | \psi_0 \rangle = 0 \\ \langle \Phi_{ij}^{ab} | e^{-\hat{T}} \hat{H} e^{\hat{T}} | \Phi_0 \rangle = E \langle \psi_{ij}^{ab} | \psi_0 \rangle = 0 \\ \langle \Phi_{ijk}^{abc} | e^{-\hat{T}} \hat{H} e^{\hat{T}} | \Phi_0 \rangle = E \langle \psi_{ijk}^{abc} | \psi_0 \rangle = 0 \\ \langle \psi^* | e^{-\hat{T}} \hat{H} e^{\hat{T}} | \psi_0 \rangle = E \langle \psi^* | \psi_0 \rangle = 0 \end{gathered} \quad \textbf{(3.70)}$$

CC theory is recognized as one of the most accurate methodologies for predicting excitation energies, often outperforming Time-Dependent Density Functional Theory calculations. However, the high computational cost and time requirements have motivated the development of truncated CC methods. The most common truncated model is CCSD, which neglects excited determinants of order higher than doubles; it remains highly accurate but is primarily efficient for small molecular systems. Methods such as CC2 compute single excitation energies at the CC level while treating double excitations with an MP2 correction to reduce computational demands. CC2, in particular, offers improved results compared to MP2 by lowering spin contamination [109]. Additional efficiency and accuracy can be achieved by incorporating techniques such as Spin-Component Scaling, Scaled Opposite Spin, Domain-based Local Pair Natural Orbitals, and/or the Resolution of Identity approximation [110–112].

3.8 Density functional theory

In contrast to molecular modeling methods based on the spring model and to ab initio approaches that approximate the electronic wavefunction, density functional theory (DFT) is formulated in terms of the explicit dependence of the total energy on a functional of the electron density $\rho(\vec{r})$. The latter represents the probability distribution of electrons in a system and constitutes a physically observable quantity that can be reconstructed from experimental techniques such as X-ray or electron diffraction [113]. Notably, it depends only on three spatial coordinates, regardless of molecular size. These properties enable DFT to achieve accuracy comparable to that of ab initio methods, often with greater computational efficiency for large systems such as biomolecules and polymeric materials. Moreover, DFT can be extended to treat more complex scenarios, including spin-polarized systems [114] and electronic band-structure calculations [115].

$$\rho(\vec{r}_1) = N\int |\Psi(\vec{r}_1, \vec{r}_2, \dots, \vec{r}_N)|^2 d\vec{r}_2 d\vec{r}_3 \cdots d\vec{r}_N. \tag{3.71}$$

Equation **(3.71)** gives the probability of finding an electron with arbitrary spin in the volume element around $\vec{r}_1$, with N as the normalization factor (i.e., number of electrons).

3.8.1 The Thomas-Fermi model

The first density-functional description of matter traces back to the independent works of Thomas and Fermi (1927) [73], who used quantum-statistical methods to relate the local electron density to a local Fermi momentum. In the Thomas–Fermi (TF) model, an atom is treated as a locally uniform electron gas and it was formulated as a “tiny cubic of side L”, each containing several electrons N from the total N_e. These electrons are assumed to be homogeneously distributed and behave like particles in a 3D box, with quantized energy given by:

$$E_{n_1n_2n_3} = \frac{\hbar^2\pi^2}{2m_eL^2}(n_1^2 + n_2^2 + n_3^2), n_1, n_2, n_3 \in \mathbb{N}. \tag{3.72}$$

where n_1, n_2, n_3 are quantum numbers. The total number of quantum states with energy below a certain value corresponds to the volume of a sphere of radius n_{max} in (n_1, n_2, n_3) space. At $T = 0$ each state is occupied by up to two electrons (Pauli principle), and the highest occupied level defines the local Fermi energy. Passing to the continuum and imposing local homogeneity yields the familiar uniform-electron-gas relations:

$$k_F(\vec{r}) = [3\pi^2\rho(\vec{r})]^{\frac{1}{3}}, t(\vec{r}) = \frac{3}{10}(3\pi^2)^{\frac{2}{3}}\frac{\hbar^2}{m_e}\rho^{\frac{5}{3}}(\vec{r}) \tag{3.73}$$

where $k_F(\vec{r})$ is the Fermi wave number and $t(\vec{r})$ is the kinetic-energy density of a uniform electron gas. Integrating $t(\vec{r})$ and adding electron–nucleus attraction and classical electron–electron repulsion yields the Thomas-Fermi functional:

$$E_{TF}[\rho] = C_F\int \rho^{\frac{5}{3}}(\vec{r})d\vec{r} + \int v_{ext}(\vec{r})\rho(\vec{r})d\vec{r} + \frac{1}{2}\int\int \frac{\rho(\vec{r})\rho(\vec{r}')}{|\vec{r} - \vec{r}'|}d\vec{r}d\vec{r}' \tag{3.74}$$

with $C_F = \frac{3}{10}(3\pi^2)^{\frac{2}{3}}\hbar^2/m_e$ and $v_{ext}(\vec{r}) = -\frac{Ze^2}{r}$

The TF formalism neglects exchange–correlation effects. While the total energy in this approach depends only on four variables (three spatial coordinates and spin), reducing the computational cost compared to methods that treat each electron explicitly, it fails to correctly predict bonding energies, which implies an unstable structure, prone to dissociation into atoms. Consequently, it is only qualitatively reliable for describing valence shells in metallic systems, where electrons can be approximated as a delocalized electron cloud.

In 1930, Dirac derived an expression for the local exchange energy of a uniform electron gas:

$$E_x^{Dirac}[\rho] = -C_x\int \rho^{\frac{4}{3}}(\vec{r})d\vec{r}, C_x = \frac{3}{4}\left(\frac{3}{\pi}\right)^{\frac{1}{3}} e^2 \tag{3.75}$$

leading to the Thomas–Fermi–Dirac theory. Historically, Bloch (1929) obtained an equivalent local-exchange form slightly earlier [89]. Later, Slater (1951) introduced a method that scales the Dirac exchange by an empirical factor. It improves on TF by incorporating exchange effects [116], and can be used within the SCF procedure of HF calculations. It saw applications to atoms, molecules, and solids, but it still omits correlation and does not correct the fundamental bonding deficiencies. Later, both were largely superseded in practical electronic-structure work by Kohn–Sham DFT (1965) with modern exchange–correlation approximations [82].

3.8.2 Density functional formalism

3.8.2.1 Hohenberg–Kohn theorem

The first Hohenberg–Kohn theorem establishes that all properties of a many-electron ground state are uniquely determined by its electron density $\rho(\vec{r})$. In this framework, the electron cloud is subjected to the electrostatic potential of the nuclei, treated as an external potential $V_{ne}(\vec{r})$. Indeed, there exists a one-to-one correspondence between $\rho(\vec{r})$ and $V_{ne}(\vec{r})$ (up to an additive constant) [62, 82]. The total energy functional can thus be expressed as:

$$E[\rho(\vec{r})] = E_{HK}[\rho(\vec{r})] + \int V_{ne}(\vec{r})\rho(\vec{r})d\vec{r} \tag{3.76}$$

where $E_{HK}[\rho(\vec{r})]$ is an universal functional comprising the kinetic energy and the electron–electron interaction energy of the interacting system.

The second Hohenberg–Kohn theorem, analogous to the variational principle for wavefunctions, states that for any trial density $\tilde{\rho}(\vec{r})$ satisfying the N-representability condition, the corresponding total energy is greater than or equal to the true ground-state energy, with equality achieved only for the exact ground-state density. Minimization of $E[\rho]$ under the constraint that the total number of electrons is fixed at N is achieved via the method of Lagrange multipliers, introducing μ such that:

$$\frac{\delta}{\delta\rho(\vec{r})}\left[E[\rho] - \mu\left(\int \rho(\vec{r})d\vec{r} - N\right)\right] = 0 \tag{3.77}$$

leading to the Euler–Lagrange equation:

$$\frac{\delta E_{HK}[\rho(\vec{r})]}{\delta\rho(\vec{r})} + V_{ne}(\vec{r}) = -\mu \tag{3.78}$$

Here, μ is identified as the chemical potential of the electron cloud in the external nuclear potential. In practice, the exact solution of this equation is unattainable because the precise form of $E_{HK}[\rho(\vec{r})]$ for an interacting system is unknown.

Unlike the variational HF method, which guarantees that the calculated energy is always an upper bound to the exact ground-state energy, density functional theory employs practical approximations to the universal functional $E_{HK}[\rho(\vec{r})]$ and these approximations may occasionally produce total energies that are slightly lower than the true ground-state value.

3.8.2.2 The Kohn-Sham energy

Kohn–Sham [82] separates the exact electronic energy into two parts (within the BO approximation): a fictitious non-interacting system whose ground-state electronic density matches that of the real interacting system, a correction term incorporating exchange and correlation effects as a functional of the electron density, which are neglected in HF theory:

$$E[\rho(\vec{r})] = T_e[\rho(\vec{r})] + J[\rho(\vec{r})] + V_{ne}[\rho(\vec{r})] + E_{XC}[\rho(\vec{r})] \quad \textbf{(3.79)}$$

$$E[\rho(\vec{r})] = T_e[\rho(\vec{r})] + \frac{1}{2}\int\int \frac{\rho(\vec{r})\rho(\vec{r}')}{|\vec{r}-\vec{r}'|} d\vec{r}d\vec{r}' + V_{ne}[\rho(\vec{r})] + E_{XC}[\rho(\vec{r})] \quad \textbf{(3.80)}$$

Here, $T_e[\rho(\vec{r})]$ is the kinetic energy of the non-interacting electrons, $J[\rho(\vec{r})]$ is the classical Coulomb repulsion, and $V_{ne}[\rho(\vec{r})]$ represents the interaction between electrons and the static nuclear field.

Due to the absence of a known explicit kinetic energy functional in terms of the electron density, Kohn–Sham reintroduces a set of non-interacting single-electron orbitals, which are solutions to independent linear wavefunction equations known as the Kohn–Sham equations:

$$\left(-\frac{1}{2}\nabla^2 + V_{KS}(\vec{r})\right)\Psi_i^{KS} = \varepsilon_i\Psi_i^{KS} \quad \textbf{(3.81)}$$

where V_{KS} is an effective potential incorporating J, V_{ne} and E_{XC} effects.

The KS orbitals do not necessarily have a direct physical interpretation; they serve as an intermediate construct to reproduce the exact ground-state electron density of the interacting system.

To solve the Kohn–Sham equations, a SCF procedure must be employed. An initial guess for the density, calculated from semiempirical or lower-level HF results, is used to determine the Kohn–Sham operator, where

$$V_{KS}(\vec{r}) = \frac{\delta E_{KS}[\rho(\vec{r})]}{\delta\rho(\vec{r})} \quad \textbf{(3.82)}$$

In the next step, the molecular orbitals are expanded in a linear combination of atomic orbitals, leading to a matrix eigenvalue equation of dimension $l \times l$ (involving l^2 one-electron integrals and, l^4 two-electron integrals), analogous to the Roothaan equations. Solving this equation yields the coefficients that express the Kohn–Sham orbitals as linear combinations of the original, non-orthogonal basis functions, along with the corresponding orbital energies. The updated electron density is then computed as:

$$\rho = 2\sum_{i=1}^{\frac{N}{2}} |\psi_i^{KS}|^2 \qquad \textbf{(3.83)}$$

for restricted closed-shell configurations.

This process is repeated until self-consistency is reached. The accurate evaluation of the XC potential matrix is non-trivial due to the complexity of $E_{HK}[\rho(\vec{r})]$, which generally cannot be integrated analytically. In practice, the integration domain is partitioned into atom-centered grids, each defined by concentric radial shells and associated spherical angular points.

3.8.2.3 Exchange correlation functional

Kohn-Sham density functional theory is the predominant method for calculating electronic structures of both ground and excited states, generally offering reliable accuracy. The exchange–correlation $E_{XC}[\rho(\vec{r})]$ functional incorporates corrections for the kinetic-energy difference between interacting and noninteracting electrons, self-interaction errors, and quantum-mechanical electron–electron repulsion. However, while density functional theory is formally an exact theory, practical calculations often exhibit inaccuracies due to approximations in $E_{XC}[\rho(\vec{r})]$ functional. Furthermore, the accuracy of these calculations can depend on factors such as system size and the character of intra- or intermolecular interactions, encompassing covalently bonded systems, ionic crystals, and metallic clusters. The $E_{XC}[\rho(\vec{r})]$ functionals are commonly classified into five categories according to Jacob's ladder, based on their level of sophistication and the type of parameters employed [117]. Lower rungs primarily rely on empirical parameters fitted to experimental databases (e.g., atomization energies, ionization potentials, electron affinities). Higher rungs incorporate rigorous physical constraints, theoretical parameters, and non-local contributions (like exact exchange or virtual orbitals), while still often employing some empirical fittings. In general, climbing the ladder improves the balance between accuracy and transferability, albeit at the expense of increased computational cost.

- Rung 1: Local density approximation:

The simplest approximation for $E_{XC}[\rho(\vec{r})]$ is the local density approximation (LDA). The underlying idea is to represent the inhomogeneous electron density of a molecule as a collection of infinitesimal regions, each approximated by a homogeneous electron gas with the local density at that point. The total exchange–correlation energy is then obtained by integrating over the entire space:

$$E_{XC}[\rho(\vec{r})] = \int \rho(\vec{r})\varepsilon_{XC}[\rho(\vec{r})]d\vec{r} \tag{3.84}$$

where $\varepsilon_{XC}[\rho(\vec{r})]$ denotes the exchange–correlation energy per electron for a uniform electron gas of density $\rho(\vec{r})$. In the case of open-shell systems treated using the unrestricted formalism, the spatial orbitals for spin-up (α) and spin-down (β) electrons differ. As a result, the functional depends explicitly on the spin densities:

$$E_{XC} = E_{XC}[n_\alpha, n_\beta] \tag{3.85}$$

Here, the corresponding exchange–correlation potentials are obtained by taking derivatives with respect to each spin density individually, rather than with respect to the total electron density.

Despite neglecting non-local van der Waals interactions, LDA often gives surprisingly good agreement with experimental reference values for surface properties (such as surface energy and work function) of alkali and transition metals [118]. This accuracy arises from systematic error cancellation, as the overestimation of the exchange energy and the underestimation of the correlation energy tend to offset each other. However, LDA performs poorly when the electron density exhibits rapid spatial variations. In such cases, it typically overestimates cohesive energies, underestimates lattice constants for molecular solids, and fails to capture weak dispersion interactions [119, 120].

- Rung 2: Generalized gradient approximation

The generalized gradient approximation (GGA) introduces semi-local effects by making the exchange–correlation energy dependent not only on the electron density ρ but also on its spatial gradient, $\nabla\rho$. This additional dependence allows GGA to provide a more reliable treatment of phenomena like electron delocalization in covalent bonding and specific classes of noncovalent interactions.

The functional is separated into exchange and correlation components, which are modeled independently:

$$\mathrm{E_{XC}^{GGA} = E_{X}^{GGA} + E_{C}^{GGA}} \quad \textbf{(3.86)}$$

For example, the BLYP [121] functional combines Becke's 1988 (B88) exchange functional with the Lee–Yang–Parr (LYP) correlation functional. The LYP functional, developed by Lee, Yang and Parr, is derived from the Colle–Salvetti correlation energy formula [122], originally formulated to reproduce the correlation energy of the helium atom using its HF wavefunction. Thus, it is not strictly an ab initio method. However, it succeeds in reducing the self-interaction error [123].

- Rung 3: Meta-generalized gradient approximation

Meta-generalized gradient approximations (meta-GGAs) extend GGAs by including, in addition to the electron density and its first derivative, the Laplacian (second derivative), which captures the spatial curvature of the density. However, the Laplacian can be numerically unstable. A common alternative is to use the kinetic-energy density, which is typically more stable, while remaining implicitly dependent on the density Laplacian. It can be expressed as follows:

$$\mathrm{E_{Kinetic}}(\vec{\mathrm{r}}) = \sum_{\mathrm{i}}^{\mathrm{occ}} \frac{1}{2} |\nabla \psi_{\mathrm{i}}^{\mathrm{KS}}|^2 \quad \textbf{(3.87)}$$

where $\psi_{\mathrm{i}}^{\mathrm{KS}}$are self-consistent Kohn-Sham orbitals.

SCAN is an example of a meta-GGA functional, which improves accuracy over conventional GGAs, particularly for lattice constant and weak bonds [124].

- Rung 4: Hybrid functional

Beyond meta-semi-local effects, Axel Becke demonstrated that the accuracy of electronic energy calculations can be improved by incorporating a fraction of exact HF exchange into pure DFT functionals[125] .

This approach is grounded in the adiabatic connection formalism, in which the exchange–correlation energy is expressed as:

$$\mathrm{E_{XC}} = \left\langle \Psi(\emptyset) \middle| \hat{\mathrm{V}}_{\mathrm{XC}}(\emptyset) \middle| \Psi(\emptyset) \right\rangle \quad \textbf{(3.88)}$$

Where Ø is a continuous integral parameter that scales the electron–electron interaction, with the lower bound Ø=0 corresponding to the noninteracting Kohn–Sham reference system and the upper bound Ø=1 corresponding to the fully interacting physical system. Here, the operator $\widehat{V}_{XC}(Ø)$ is the exchange correlation potential:

$$V_{XC}(\vec{r}) = \frac{\delta E_{XC}[\rho(\vec{r})]}{\delta\rho(\vec{r})} \quad \textbf{(3.89)}$$

To evaluate equation **(3.88)**, an integral should be calculated. The values of E_{XC} at the endpoints Ø={0,1} are well-known, while modeling E_{XC} for 0<Ø<1, which corresponds to the intermediate portion of the adiabatic connection integral, is challenging.

Hybrid functionals address this issue by interpolating between the two coupling-strength limits, replacing a fraction of the approximate DFT exchange with HF-like exact exchange evaluated using Kohn–Sham orbitals, rather than HF orbitals, in order to avoid additional computational overhead.

$$E_{XC}^{hybrid} \approx aE_X^{HF} + bE_{XC}^{DFT} \quad \textbf{(3.90)}$$

In general the coefficients in hybrid exchange–correlation functionals are determined either empirically, by fitting to experimental properties such as atomization energies, ionization potentials, proton affinities, and total atomic energies of small molecules, or theoretically, based on principles such as the adiabatic connection formalism (equation **(3.88)**).

The fraction of HF exchange is adjusted to optimize accuracy for the specific molecular system or type of interaction. In certain cases, introducing long-range correction helps maintain a balanced description of the electronic structure [126, 127].

- *Low HF: For example, TPSSh (10%) and B3LYP (20%):*

TPSSh (10% HF exchange; meta-GGA with Tao–Perdew–Staroverov–Scuseria exchange + modified PBE correlation) incorporates a kinetic-energy density term, improving its accuracy for transition metals and systems with static correlation (e.g., spin states in organometallic complexes) [128].

B3LYP (20% HF exchange; B88 exchange + LYP correlation) performs well in organic and main-group chemistry due to its refined parametrization for bond energies, vibrational frequencies, and aromatic systems [129, 130].

- *Moderate HF: For example, PBE0 (25%):*

The PBE0 hybrid functional is effective for semiconductors and transition metal compounds. It exhibits strong performance in the accurate computation of band gap predictions and bulk moduli for materials like Ge, Si, $BaTiO_3$, and β-GaN compared to GGA [131]. PBE0 was evaluated for a series of transition-metal hydrides (bond lengths and vibrational frequencies) and transition-metal halides (dipole polarizabilities). These properties show good accuracy, with root mean square relative errors of 0.008, 0.058, and 0.104, respectively, compared to experimental data [132].

- High HF: For example, BMK (42.8%), MN15 (44%), and M06-2X (54%):

BMK (Boese-Martin for Kinetics) has about 42.8% HF exchange and is built to deal with thermochemistry and kinetics calculations, especially barrier heights in reaction mechanisms. It shows balanced accuracy for reaction energetics and transition state calculations [133].

MN15 is a hybrid meta-GGA functional with 44% HF exchange and is one of the more recent additions to the Minnesota family of functionals. Performance benchmarks indicate that MN15 yields low mean unsigned errors across single-reference and inherently multiconfigurational (near degenerate states) systems, making it one of the most generally reliable functionals for various chemical challenges [134]. Moreover, M06-2X, part of the Minnesota functional family, is empirically parameterized with a dataset that includes dispersion forces and non-covalent interactions. Benchmark studies show M06-2X provides interaction energies for weakly bound complexes that are closer to high-level wavefunction methods like CCSD(T), outperforming many traditional DFT functionals [135].

The limitation of hybrid functionals is that they can produce spurious, unphysical interactions when the calculated exact HF fraction deviates from the expected asymptotic behavior $1/r$. This issue is addressed by partitioning the exact HF contribution into short-range and long-range components, with appropriate adjustments applied to each [87].

- Rung 5: Double-hybrid functional

Double-hybrid density functionals improve the description of dynamic electron correlation by incorporating a perturbative second-order Møller–Plesset (MP2) correlation term, evaluated using Kohn–Sham orbitals, into the exchange–correlation energy expression [87].

A recent study on the vertical excitation energies of BODIPY dyes demonstrates that spin-scaled, long-range-corrected double-hybrid functionals, particularly SOS-ωB2GP-PLYP, SCS-ωB2GP-PLYP, and SOS-ωB88PP86, effectively address the long-standing DFT overestimation problem for these compounds, achieving mean absolute errors within the chemical-accuracy threshold (~0.1 eV) when benchmarked against experimental data [136].

3.9 Time-dependent density functional theory

The determination of excited-state properties, including excitation energies, frequency-dependent response functions, and absorption or emission spectra, is essential for understanding diverse spectroscopic phenomena. Within the Kohn–Sham framework, one approach for this purpose is the Configuration Interaction Singles method based on DFT orbitals (DFT/CIS), developed by Grimme. Although this method lacks a rigorous theoretical foundation and is applicable to a limited range of systems, it has shown reasonable accuracy for organic molecules, including aromatic hydrocarbons as large as pentacene, with deviations from experimental values typically within a few tenths of an electronvolt [137]. In contrast, the EOM-CC method delivers high accuracy for small systems but is computationally impractical for larger molecular systems owing to its steep scaling with system size.

Another promising method for studying time-evolving quantum systems is Time-Dependent Density Functional Theory (TDDFT). This approach extends the framework of ground-state DFT to systems evolving from a fixed initial quantum state under the influence of a time-dependent external potential $V'_{ext}(\vec{r},t)$, analogous to the time-dependent Schrödinger equation:

$$i\frac{\partial}{\partial t}\Psi(t) = \hat{H}(t)\Psi(t) \qquad \textbf{(3.91)}$$

The external perturbation is typically represented as a Taylor expansion around the initial time t_0. The response of the quantum system depends on the magnitude of this perturbation. For small perturbations, the system operates within the linear-response (LR) regime, where the changes in observable properties are a linear functional of the external perturbation strength:

$$\delta O = \int \chi(\vec{r},\vec{r}',\omega)\delta V'_{ext}(\vec{r}',\omega)d\vec{r}' \qquad \textbf{(3.92)}$$

Here χ is the LR function (a functional kernel) and $\delta V'_{ext}$ is the perturbing potential. However, for larger perturbations, the linear approximation breaks down, and the TDDFT equations must be explicitly propagated in time to accurately capture the system’s nonlinear dynamical behavior. In such cases, a full time-dependent solution is required.

3.9.1 Runge-Gross theorem

Similar to the Hohenberg–Kohn theorem for ground-state DFT, the Runge–Gross theorem establishes a one-to-one mapping between the time-dependent electron density $\rho(\vec{r}, t)$ of a many-body system (evolving from a fixed initial wavefunction Ψ_0 at t_0= 0) and the external potential $V'_{ext}(\vec{r}, t)$.

Since the time-dependent wavefunction differs from the initial state only by a time-dependent phase factor, we can write:

$$\Psi(t) = e^{-i\beta(t)}\Psi[\rho, \Psi_0](t). \qquad \textbf{(3.93)}$$

where $\frac{d\beta(t)}{dt} = C(t)$ is a real, time-dependent function.

Thus, any physical observable of the system, represented by a hermitian operator $\widehat{\Omega}(t)$, can be expressed as a functional of the density $\rho(\vec{r}, t)$ and the initial state Ψ_0.

$$\langle\Psi(t)|\widehat{\Omega}(t)|\Psi(t)\rangle = \Omega[\rho, \Psi_0](t) \qquad \textbf{(3.94)}$$

To establish the Runge–Gross theorem, it is necessary to demonstrate that two distinct time-dependent external potentials, $V'_{1,ext}$ and $V'_{2,ext}$ which differ by more than a purely time-dependent function $C(t)$ must give rise to different time-dependent particle densities, $\rho_1(\vec{r}, t)$ and $\rho_2(\vec{r}, t)$, even when both evolve from the same initial many-body state Ψ_0.

As a preliminary condition, each external potential must be analytic in time around the initial instant t = 0, allowing Taylor expansion:

$$V_{n,ext}(\vec{r}, t) = \sum_{m=0}^{\infty} \frac{1}{m!} V_{n,m}(\vec{r}) t^m$$

$$\text{where} \qquad V_{n,m}(\vec{r}) \equiv \left.\frac{\partial^m V_n(\vec{r}, t)}{\partial t^m}\right|_{t=0} \qquad \textbf{(3.95)}$$

First, they apply the k-th time derivative to the Heisenberg equation of motion for the current density operator. This shows that the initial k-th derivatives of the current densities differ when the corresponding external potentials are not spatially constant. Next, they differentiate the continuity equation k+1 times, revealing that this difference in the current densities implies an initial difference in the (k+1)-th time derivatives of the charge densities. Mathematically, since the time-Taylor expansions of two different potentials must differ at some order (equation **(3.95)**), there exists a minimal integer k>0 at which their derivatives differ by a constant, which implies the charge densities necessarily become distinct for arbitrarily small time.

In contrast to HF and ground-state density functional theory, the derivation of the Runge–Gross theorem is more involved because the variational principle for the total energy is no longer applicable, and the energy is not a conserved quantity in the time-dependent case. This necessitates the introduction of a new quantity, the quantum mechanical action, defined as:

$$\mathrm{A}[\Psi] = \int_{\mathrm{t}_0}^{\mathrm{t}_1} \mathrm{dt} \left\langle \Psi(\mathrm{t}) \middle| \mathrm{i}\frac{\partial}{\partial \mathrm{t}} - \widehat{\mathrm{H}}(\mathrm{t}) \middle| \Psi(\mathrm{t}) \right\rangle \qquad \textbf{(3.96)}$$

where seeking the $\Psi(t)$ solution of the time-dependent Schrödinger equation, that makes the action functional stationary.

For practical applications, TDDFT cannot solve the full interacting Schrödinger equation. Instead, it uses a system of noninteracting particles moving under an effective local potential $\mathrm{V}_{\mathrm{KS}}(\vec{\mathrm{r}},\mathrm{t})$. This potential is chosen in such a way that the electron density of the noninteracting system matches that of the interacting system. The noninteracting particles then evolve according to the time-dependent Kohn-Sham equation:

$$\frac{\partial}{\partial \mathrm{t}} \Psi_{\mathrm{i}}^{\mathrm{KS}}(\vec{\mathrm{r}},\mathrm{t}) = \left[-\frac{1}{2}\nabla^2 + \mathrm{V}_{\mathrm{KS}}(\vec{\mathrm{r}},\mathrm{t})\right] \Psi_{\mathrm{i}}^{\mathrm{KS}}(\vec{\mathrm{r}},\mathrm{t}) \qquad \textbf{(3.97)}$$

where $\Psi_{\mathrm{i}}^{\mathrm{KS}}(\vec{\mathrm{r}},\mathrm{t})$ is the Kohn–Sham orbital for the i-th electron in the noninteracting reference system. The Kohn–Sham potential is typically decomposed into distinct contributions:
The Hartree (classical Coulomb) potential $\mathrm{J}[\rho(\vec{\mathrm{r}},\mathrm{t})]$, the external potential $\mathrm{V}_{\mathrm{ne}}[\rho(\vec{\mathrm{r}},\mathrm{t})]$, and the exchange-correlation potential $\mathrm{V}_{\mathrm{XC}}[\rho(\vec{\mathrm{r}},\mathrm{t})]$.

$$\mathrm{V}_{\mathrm{KS}}(\vec{\mathrm{r}},\mathrm{t}) = \mathrm{J}[\rho(\vec{\mathrm{r}},\mathrm{t})] + \mathrm{V}_{\mathrm{ne}}[\rho(\vec{\mathrm{r}},\mathrm{t})] + \mathrm{V}_{\mathrm{XC}}[\rho(\vec{\mathrm{r}},\mathrm{t})] \qquad \textbf{(3.98)}$$

In the TDDFT framework, $\mathrm{V}_{\mathrm{XC}}[\rho(\vec{\mathrm{r}},\mathrm{t})]$ incorporates all essential many-body corrections beyond the mean-field approximation. In ground-state DFT, $\mathrm{V}_{\mathrm{XC}}[\rho(\vec{\mathrm{r}})]$ is obtained by taking the first functional derivative of the exchange–correlation energy $\mathrm{E}_{\mathrm{XC}}[\rho(\vec{\mathrm{r}})]$ with respect to the static density $\rho(\vec{\mathrm{r}})$. In contrast, in TDDFT, the ground-state variational principle is no longer valid; instead, $\mathrm{V}_{\mathrm{XC}}[\rho(\vec{\mathrm{r}},\mathrm{t})]$ is derived from the functional derivative of the quantum-mechanical action $\mathrm{A}[\Psi]$ with respect to the time-dependent density $\rho(\vec{\mathrm{r}},\mathrm{t})$.

$$\mathrm{V}_{\mathrm{XC}}([\rho],\tau) = \frac{\delta \widetilde{\mathrm{A}}_{\mathrm{XC}}[\rho]}{\delta\rho(\vec{\mathrm{r}},\tau)} |\rho_{(\vec{\mathrm{r}},\tau)} \qquad \textbf{(3.99)}$$

where τ is the Keldish pseudotime.

In most practical TDDFT applications, the exact functional form of the external potential $V_{ne}[\rho(\vec{r},t)]$ is not a primary concern, since it is fixed by the particular physical system being investigated. However, the exchange–correlation potential $V_{XC}[\rho(\vec{r},t)]$ presents the main challenge, since it depends not only on the electron density ρ_0 but also on the exact initial many-body wavefunction Ψ_0 of the interacting system corresponding to the time-dependent Kohn–Sham system. The exact form of $V_{XC}[\rho(\vec{r},t)]$ is highly complex, but if it were known, it could be used to solve any time-dependent problem involving interacting electrons. One way to address this complexity is to assume that the exchange–correlation potential responds instantaneously to changes in the electron density over time. This approach is known as the adiabatic approximation.

Linear response theory is a common approach for handling small perturbations caused by a weak external potential. It is frequently applied in spectroscopy, where the system's response to a weak external field is used to extract excitation spectra (e.g., Zeeman and Stark effects at the atomic level).

Suppose a system of interacting particles initially occupies its ground state. At time $t_0 = 0$, it is subjected to a first-order external perturbation. The time-independent ground-state density then responds to the total time-dependent external field:

$$V_{ext} = V_{ne} + v_1(\vec{r},t) \tag{3.100}$$

The time-dependent density $\rho(\vec{r},t)$ can be expressed as a Taylor expansion:

$$\rho(\vec{r},t) = \rho_0(\vec{r}) + \rho_1(\vec{r},t) + \rho_2(\vec{r},t) + \cdots \tag{3.101}$$

Here, $\rho_1(\vec{r},t)$ is the first-order perturbation in the density, while higher-order terms such as $\rho_2(\vec{r},t)$ are neglected.

The first-order density change in the frequency domain can be written as:

$$\rho_1(\vec{r},\omega) = \int S(\vec{r},\vec{r}',\omega)v_1(\vec{r}',\omega)d\vec{r}' \tag{3.102}$$

where $S(\vec{r},\vec{r}',\omega)$ is the density–density response function, defined in the time domain as:

$$S(\vec{r},t,\vec{r}',t') = -i\theta(t-t')\langle\Psi_0|\left[\hat{\rho}_{H_0}(\vec{r},t),\hat{\rho}_{H_0}(\vec{r}',t')\right]|\Psi_0\rangle \tag{3.103}$$

The step function $\theta(t-t')$ enforces causality by ensuring that the system's response occurs only after the perturbation is applied. Meanwhile, the commutator of density operators allows for the mixing of quantum states.

In the TDDFT framework, the linear density response is obtained by evaluating the response of the time-independent, non-interacting Kohn–Sham reference system, denoted as $S_0^{(KS)}$, to an effective time-dependent perturbation potential. This potential includes a monochromatic dipole field applied along the z -direction as the external perturbation:

$$v_1(\vec{r}, t) = A\vec{e}_z \sin(\omega t) \tag{3.104}$$

By inserting the unperturbed Kohn-Sham orbitals into the linear density–density response function, one obtains:

$$S^{(KS)}(\vec{r}, \vec{r}', \omega) = \lim_{\gamma \to 0} \sum_{i,j} \left(f_j - f_i\right) \frac{\Phi_i(\vec{r})\Phi_i^*(\vec{r}')\Phi_j(\vec{r}')\Phi_j^*(\vec{r})}{\omega - \left(\varepsilon_i - \varepsilon_j\right) + i\gamma} \tag{3.105}$$

Equation **(3.105)** has a pole at $\omega = \varepsilon_i - \varepsilon_j$. f_I and f_j are the usual Fermi occupation numbers, ε_I and ε_j are the Kohn-Sham energies (non-interacting system).

3.9.2 Casida's linear-response formalism

In 1995, Casida formulated a non-Hermitian eigenvalue problem to describe the transitions between occupied and unoccupied Kohn–Sham orbitals, based on the LR Time-Dependent Density Functional Theory (LR-TDDFT) and the adiabatic approximation to the exchange–correlation potential functional [138]. He derived an equation for the dynamic response of the Kohn–Sham density matrix to an external perturbation. In this context, the excited-state density can be viewed as the functional derivative of the excited-state energy with respect to the perturbing external potential. The resulting dynamic equation is:

$$\begin{pmatrix} A & B \\ B^* & A^* \end{pmatrix} \begin{pmatrix} X \\ Y \end{pmatrix} = \omega \begin{pmatrix} -1 & 0 \\ 0 & 1 \end{pmatrix} \begin{pmatrix} X \\ Y \end{pmatrix} \tag{3.106}$$

where $A_{ia,jb} = (\epsilon_a - \epsilon_i)\delta_{ij}\delta_{ab} + K_{ia,jb}$ and $K_{ia,jb}$ are the Coulomb and exchange-correlation contributions. $B_{ia,jb} = K_{ia,bj}$ represents coupling between transitions involving excitations and de-excitations. X_{ia} is the amplitude of the excitation from occupied orbital i to a virtual orbital j. Y_{ia} is the amplitude of the de-excitation and ω is the excitation energy.

By solving Casida's equations within the framework of LR-TDDFT, several important electronic and spectroscopic properties of molecular systems can be obtained:

- *Excitation energies:*

The eigenvalues of Casida's matrix correspond to the excitation energies of the system.

- *Oscillator strengths:*

These define the probability of electronic transitions from occupied to unoccupied (virtual) states and therefore determine the intensity of absorption bands in a spectrum. In atomic units, the oscillator strength is given by:

$$\mathrm{f} = \frac{2}{3} \sum_{\alpha = x,y,z} \omega \, |\langle \Psi_0 | \hat{\mu}_\alpha | \Psi_k \rangle|^2 \tag{3.107}$$

where $\hat{\mu}_\alpha$ is the α component of the dipole operator.

- *Frequency-dependent polarizability:*

Combining excitation energies with oscillator strengths allows the calculation of the frequency-dependent polarizability tensor. This tensor, representing the second derivative of the excited-state energy with respect to an external electric field, characterizes the system's linear response to time-dependent electromagnetic fields and is directly related to its optical properties.

- *Excited-state potential energy surfaces:*

Casida's approach enables the construction of BO PESs for excited states by combining ground-state total energies with excitation energies. These surfaces are crucial for modeling photochemical processes and understanding reaction dynamics.

By neglecting the off-diagonal terms $B_{ia,jb}$, which represent the coupling between excitation and de-excitation processes, and considering only single excitations (transitions from occupied to unoccupied orbitals), Casida's equations can be transformed into a Hermitian form, making them more tractable to solve. This simplification, known as the Tamm–Dancoff approximation (TDA), reduces the dimensionality of the problem by half and improves numerical stability, particularly for systems with near-degenerate states or small singlet–triplet energy gaps. However, it may yield inaccurate results for oscillator strengths and double excitations due to its violation of the Thomas–Reiche–Kuhn (TRK) sum rule [139].

Extensive research has evaluated the performance of the TDA across different systems and properties. A systematic comparison of TDA, full TDDFT, and the RPA showed that TDA reliably reproduces experimental absorption and emission spectra, including band shapes, peak positions, and 0–0 transition energies, for medium-sized conjugated molecules, particularly when used in combination with the B3LYP functional [140]. Another study demonstrated that

TDA outperforms full TDDFT in calculating non-adiabatic couplings for systems exhibiting Jahn–Teller, Renner–Teller, or accidental conical intersections. This improvement is attributed to TDA's partial mitigation of errors from the local density approximation through error-cancellation effects [141].

For open-shell radicals lacking pronounced double-excitation or multireference character, TDA combined with double-hybrid functional SOS-ωB88PP86 achieves a mean absolute deviation of 0.12–0.14 eV compared to high-level theoretical reference data. This conclusion stems from a study evaluating 20 functionals spanning the fourth to fifth rungs of Jacob's Ladder (e.g., hybrid to double-hybrid functionals [142].

While the TDA offers computational efficiency, its applicability is limited in systems requiring precise treatment of electron correlation effects. By neglecting de-excitation processes, TDA cannot accurately describe systems dominated by double excitations or multireference character, leading to errors in calculated oscillator strengths and transition dipole moments. Furthermore, TDA tends to overestimate excitation energies, particularly for low-energy singlet states, by approximately 0.02–0.25 eV compared to full TDDFT [143]. These limitations make TDA less reliable for spectroscopic studies of strongly correlated systems or those with extensive electron delocalization, where full TDDFT or advanced wavefunction-based approaches (e.g., CASSCF, NEVPT2) are often required for quantitative accuracy [144].

3.10 Solvation model

The study of isolated molecular structures in the gas phase is relatively simple from a theoretical and computational standpoint and allows the probing of the intrinsic properties of molecules, independent of external influences. However, when the purpose is to understand how a realistic environment affects a system, solvent effects must be included. Interactions between the chemical system and its surroundings can induce a range of physical changes, such as solvatochromic shifts, energy quenching, geometrical distortions, or aggregation in flexible structures. These modifications alter spectral and thermodynamic properties and may redirect chemical reactions along different pathways.

In quantum chemical computations, solvent effects can be treated using two main approaches: implicit and explicit models.

Implicit solvation models are the most common and widely applied [62, 145, 146]. In these models, the solvent is represented as a continuous dielectric medium surrounding the solute, which is placed inside a cavity. Each atom of the solute is assigned a sphere whose radius is determined by fitting to experimental solvation Gibbs free energies. The model assumes that the solute responds to the solvent's polarizability in the same way that the solvent responds to the solute's polarizability. The electrostatic interaction between solute and solvent is computed by solving the Poisson equation self-consistently [147]. Mennucci and Tomasi simplified this approach by introducing an infinite dielectric constant as a boundary condition [148].

Although implicit models are grounded in physical principles, they generally require empirical corrections to capture non-electrostatic contributions, such as van der Waals interactions and cavitation energies. For example, the solvation model based on density (SMD) refines the polarizable continuum model (PCM) framework by incorporating hydrogen-bonding effects [149]. In TDDFT combined with PCM, the LR approach typically estimates solute rearrangement from the transition dipole moment. By contrast, the state-specific (SS) approach determines the solvation effect from the change in charge density between the ground and excited states [150]. LR methods become less accurate when the charge density difference is large, as in strongly polar excited states or charge-transfer states. In such cases, SS methods improve accuracy by treating solvent polarization self-consistently [151].

Explicit solvation models, on the other hand, represent each solvent molecule (or at least each solute–solvent interaction site) individually. This approach is crucial in quantum dynamics simulations, where specific hydrogen-bonding interactions or other anisotropic solute–solvent effects significantly influence the system's behavior [152].

3.11 Photophysical properties

Within the framework of the BO approximation, the total energy of a molecule in a given electronic state depends on its nuclear configuration, which is represented by the corresponding potential energy surface. Transitions between electronic states are governed by selection rules, specifically $\Delta S = 0$ (total spin conservation) and $\Delta L = 0, \pm 1$ (change in the orbital angular momentum quantum number). This approximation provides both a qualitative and a quantitative foundation for understanding molecular structure, energetics, and reactivity [62, 87].

When a PES is approximated as harmonic near its minimum, the resulting vibrational Schrödinger equation yields solutions expressed in terms of orthonormal wavefunctions, which are products of Hermite polynomials and Gaussian functions, characteristic of the quantum harmonic oscillator.

Beyond the BO approximation, nonadiabatic couplings (NACs) between electronic states are taken into account to describe processes such as IC and ISC. These radiationless transitions are facilitated by nuclear motion through regions where potential energy surfaces approach closely (e.g., conical intersections), where the BO approximation collapses. Vibrational relaxation within an electronic state generally proceeds more rapidly than these nonradiative transitions; thus, molecules often undergo such processes from the lowest vibrational level of the excited state.

According to the Franck-Condon (FC) principle, radiative electronic transitions occur vertically between PESs, with no instantaneous change in nuclear coordinates or vibrational quantum states. This vertical transition arises because the timescale for electronic transitions (absorption or fluorescence) is significantly shorter than that required for nuclear reorganization. Consequently, during the transition, the nuclei can be considered stationary (the BO approximation holds instantaneously), and the electronic transition dipole moment is evaluated at a fixed nuclear geometry.

Following the transition, the redistribution of electronic charge alters the Coulombic forces within the molecule, which in turn modifies the vibrational wavefunctions. The simultaneous change in both electronic and vibrational states constitutes a vibronic transition. The FC principle plays a central role in interpreting the intensity distribution of vibronic transitions, which is influenced by factors such as molecular symmetry, torsional distortions, and temperature.

The probability of a transition is directly related to the square of the overlap integral between the vibrational wavefunctions $<\psi_{\nu}|\psi_{\nu'}>$ of the electronic states involved, multiplied by the square of the transition dipole moment. The vibrational overlap is determined by the shapes of the PESs and by the displacement of their equilibrium positions during the transition.

Case 1: if $\mathrm{Q_e} = \mathrm{Q_{e'}}$ where $\mathrm{Q_e}$ and $\mathrm{Q_{e'}}$ are the equilibrium internuclear distances of the lower and upper PES, respectively, and the surfaces lie vertically above one another, the most intense transition corresponds to the 0–0 band. In this case, the overlap integral, arising from the overlap of two bell-shaped functions involves no significant change in nuclear position or vibrational kinetic energy during the transition. In contrast, the higher vibrational transitions have several positive and negative contributions in the overlap integral, resulting in lower intensity.

Case 2: if $\mathrm{Q_e} > \mathrm{Q_{e'}}$: the vibrational overlap is no longer maximal for the 0–0 transition. Instead, maximum overlap occurs when a higher vibrational level of the upper PES lies vertically above the ground vibrational state of the lower PES. The overlap decreases as the number of vibrational modes increases.

Case 3: if $\mathrm{Q_e} \gg \mathrm{Q_{e'}}$: the most probable transition corresponds to the overlap of the ground vibrational state of the lower PES with a much higher vibrational level of the upper PES, which may even lie in the continuum region.

Upon photoexcitation, a higher excited singlet state ($\mathrm{S_n}$, n >1) may be populated. These higher excited states generally possess weak oscillator strengths and undergo rapid nonradiative relaxation to the first excited singlet state ($\mathrm{S_1}$). This behavior is consistent with Kasha's rule, which states that emission typically occurs from the lowest excited singlet state, regardless of the excitation wavelength. From the $\mathrm{S_1}$ state, further relaxation to the electronic ground state ($\mathrm{S_0}$) can occur either radiatively, via fluorescence, or nonradiatively through IC.

Within this framework, the electronic transition between the lower and upper electronic states can be expanded in terms of the normal vibrational modes of the molecule:

$$\mu^{\mathrm{S_0S_1}}(\mathrm{Q}) = \mu_0^{\mathrm{S_0S_1}} + \sum_{\mathrm{k}}^{\mathrm{N_{vib}}} \left(\frac{\partial \mu^{\mathrm{S_0S_1}}}{\partial \mathrm{Q_k^{S_0}}}\right)_{\mathrm{Q^{S_0}}} \mathrm{Q_k^{S_0}} + \cdots \qquad \textbf{(3.108)}$$

In the FC region, the transition dipole moment is treated as independent of nuclear displacement, and only the zeroth-order term in its expansion is retained. In contrast, higher-order terms, known as Herzberg–Teller (HT) contributions, allow weak or dipole-forbidden transitions to occur by breaking molecular symmetry through vibronic coupling. In practice, the HT approximation becomes relevant when the transition dipole moment is small, since the HT contribution to $\mu_0^{\mathrm{S_0S_1}}$ never vanishes, and the vibrational wavefunctions are mixed.

A linear transformation can relate the normal mode coordinates of the excited electronic state to those of the ground state, where J is the Duschinsky rotation matrix, describing the mixing of vibrational modes between the two states, and k is the displacement vector, accounting for the shift in equilibrium geometry.

$$\mathrm{Q}^{\mathrm{S}_1} = \mathrm{J}\mathrm{Q}^{\mathrm{S}_0} + \mathrm{k} \qquad \textbf{(3.109)}$$

For large or flexible molecular systems, where substantial structural changes occur during electronic transitions, representing the transformation of normal modes between electronic states solely through a linear combination of rotation matrices and displacement vectors becomes both challenging and potentially inaccurate.

To evaluate radiative and non-radiative decay rates, a rigorous understanding of vibronic spectra is essential. These spectra are governed by the Fermi's golden rule, derived from first-order time-dependent perturbation theory. The probability of transition between initial state i and final state f of the total wavefunction under a perturbation can be expressed as :

$$\mathrm{k}_{\mathrm{if}} = \frac{2\pi}{\hbar} |\langle \Psi_{\mathrm{f}} | \widehat{\mathrm{H}}' | \Psi_{\mathrm{i}} \rangle|^2 \rho \qquad \textbf{(3.110)}$$

where:

- $\widehat{\mathrm{H}}'$is the perturbation Hamiltonian, which may represent external perturbations responsible for radiative transitions (e.g., interaction with an electromagnetic field), or intrinsic perturbations such as NACs or SO interactions in the case of non-radiative transitions.
- ρ is the density of final states at the energy corresponding to the transition.

If we assume that the PES is approximated as a parabolic shape, then the vibrational wavefunctions can be constructed as products of eigenstates of one-dimensional harmonic oscillators along the normal modes. In this framework, the NACs between electronic states is formally given by the matrix elements of the nuclear derivative operator acting on the total molecular wavefunctions.

By introducing the BO approximation, the total molecular wavefunction can be decoupled into separate electronic and nuclear (vibrational) wavefunctions, and the total non-adiabatic coupling can be written as:

$$\mathrm{NAC} = -\hbar^2 \sum_{k} \left\langle \Psi_f \Theta_{f\nu_f} \middle| \frac{\partial \Psi_i}{\partial Q_{ik}} \frac{\partial \Theta_{i\nu_i}}{\partial Q_{ik}} \right\rangle \tag{3.111}$$

where Q_{ik} are the normal modes of the electronic state i.

Assuming that the electronic coupling dominates over the vibronic coupling and that it remains independent of the vibrational degrees of freedom. The rate equation can be written as:

$$k_{if} = \frac{2\pi}{\hbar} \sum_{\nu_i,\nu_f} P_{i,\nu_i}(T) |V_{if}|^2 \left| \langle \Theta_{i,\nu_i} | \Theta_{f,\nu_f} \rangle \right|^2 \delta(E_{i\nu_i} - E_{f\nu_f}) \tag{3.112}$$

where V_{if} is the electronic non-adiabatic coupling, E is the energy and $\langle \Theta_{i,\nu_i} | \Theta_{f,\nu_f} \rangle$ are the FC overlaps and $P_{i,\nu_i}(T)$ is the density of states.

To determine the rates and spectra, two primary formalisms have been proposed: the time-independent (TI) and time-dependent (TD) approaches. The TI method facilitates the identification of individual vibrational mode contributions to the spectra, while the TD approach is computationally less demanding. The latter uses the Fourier transformation of a time correlation function to extract vibrational integrals and spectra, and it can be represented as:

$$L'(\omega) = \frac{1}{2\pi} \int dt e^{\mp it\left(\frac{\Delta E_{AD}}{\hbar} - \omega\right)} \chi(t,T) g'(t) \tag{3.113}$$

where $g'(t)$ is the broadening function and $\chi(t,T)$ the transition dipole correlation function which depends on the initial and the final vibrational Hamiltonian, the partition function and the time parameter.

Applying the Fermi Golden rule and TI formalism k_{IC} can be written as :

$$k_{IC}(\Delta E_{AD}) = \frac{2\pi}{\hbar} \sum_{\nu_i,\nu_f} \frac{e^{-\frac{E^{ES}_{\nu_i}}{k_B T}}}{Z} |\langle \Psi_{ES}, \Theta_{ES,\nu_i} | \hat{V} | \Psi_{GS,\nu_f}, \Theta_{GS,\nu_f} \rangle|^2 \delta\left(\Delta E_{AD} + E^{ES}_{\nu_i} - E^{GS}_{\nu_f}\right) \tag{3.114}$$

where $e^{-\frac{E^{ES}_{\nu_i}}{k_B T}}$ accounts for the thermal population of the initial vibrational states in the excited state, consistent with a Boltzmann distribution at temperature T and $\delta\left(E_{AD} + E^{ES}_{\nu_i} - E^{GS}_{\nu_f}\right)$ ensures the conservation of the energy during electronic transition. Z denotes the partition function, which incorporates contributions from all vibrational states.

Different physical phenomena can give rise to distinct broadening profiles in spectral lines. For instance, the uncertainty in the transition energy, governed by the Heisenberg uncertainty principle and directly related to the finite lifetime of the excited state, results in a Lorentzian line shape. In contrast, interactions with the surrounding environment, such as thermal fluctuations or inhomogeneous broadening mechanisms, typically lead to a Gaussian distribution of the transition energies. The phenomenological broadening is taken into account through the TD formalism and appears as a replacement of δ in the TI method:

$$\begin{aligned} \mathrm{k_{IC}(t)} &= \frac{1}{2\pi}\int_{-\infty}^{\infty} \mathrm{dt e^{i\Delta E_{AD}} g'(t) k'_{ic}(t)} \\ \mathrm{k'_{IC}(t)} &= \frac{2\pi}{\hbar}\frac{1}{\mathrm{Z}}\mathrm{Tr}\left[\mathrm{e}^{(\mathrm{it}-\beta)\hat{\mathrm{H}}^{\mathrm{ES}}}\hat{\mathrm{V}}_{\mathrm{i,f}}\mathrm{e}^{-\mathrm{it}\hat{\mathrm{H}}^{\mathrm{GS}}}\hat{\mathrm{V}}^{\dagger}_{\mathrm{i,f}}\right] \end{aligned} \qquad \textbf{(3.115)}$$

Similar to internal conversion, which is facilitated by vibronic coupling, radiationless decay can also proceed via ISC, driven by the magnitude of SOC and the energy gap between the singlet and triplet states. Several studies have shown that the ISC rate outcompetes other chemical processes and is less prone to broadening variations and anharmonic effects [153, 154].

In terms of phenomenology, SOC arises from the interaction between the magnetic moments generated by an electron's spin angular momentum (S) and orbital angular momentum (L), resulting in shifts in atomic and molecular energy levels.

When the spin-orbit interaction is weak relative to the electrostatic interactions among electrons, it can be treated as a perturbation. In this regime, the total spin (S) and total orbital angular momentum (L) from all electrons are summed individually, and then coupled together to form the total angular momentum (J). This scenario is known as L-S coupling (or Russell-Saunders coupling) and applies primarily to lighter elements, including those in the first row of transition metals [155].

Conversely, when the spin-orbit interaction is significantly stronger than the electrostatic interactions, each electron's individual spin ($\mathrm{S_i}$) and orbital angular momentum ($\mathrm{L_i}$) couple to form a total angular momentum ($\mathrm{J_i}$) for each electron. This regime is termed J-J coupling and typically applies to heavier atoms, such as lanthanides and actinides, where relativistic effects become substantial.

However, mathematically it is described by coupling matrix elements as shown in the expression:

$$\hat{H}_{SO}^{(0)} = \frac{1}{2m_e^2c^2}\sum_{A}\sum_{i}\frac{Z_A}{r_{ij}^3}\left(\hat{r}_{iA}\times\hat{p}_i\right)\cdot\hat{s}_i - \frac{1}{2m_e^2c^2}\sum_{i}\sum_{j\neq i}\frac{1}{r_{ij}^3}\left(\hat{r}_{ij}\times\hat{p}_i\right)\cdot\left(\hat{s}_i + 2\hat{s}_j\right) \qquad \textbf{(3.116)}$$

where A, i and j represent the nuclear and electronic indices, Z_A denotes the nuclear charge, $\hat{p}$ and $\hat{s}$ the electron momentum and spin operators, respectively, and $\hat{r}$ the position vector operator. Additionally, m_e and c correspond to the electron mass and the speed of light, respectively. In this representation, the first and second terms of the spin–orbit Hamiltonian ($\hat{H}_{SO}$) are associated with contributions arising from one-electron and two-electron integrals, respectively. The first term called ''one electron integral", represents the interaction of the spin of electron i with the magnetic field produced by the motion of nucleus A. The second term accounts for relativistic spin–orbit interactions between electrons. It describes how the spin of electron i couple to the magnetic field produced by the motion of electron i in the magnetic field generated by electron j, and vice versa. The treatment of two-electron spin–orbit interactions is computationally complex. To facilitate practical calculations, a strategy analogous to the HF approximation is employed, in which the Hamiltonian is partitioned into electrostatic and exchange-like effective potentials. This approach allows the two-electron terms to be approximated in a mean-field framework, reducing the computational cost while retaining essential relativistic effects [156].

The rate of intersystem crossing (k_{ISC}) can be derived using Fermi's Golden Rule and expressed in the following form:

$$k_{ISC} = \frac{2\pi}{\hbar Z}\left|\langle\psi_f|\hat{H}_{SOC}|\psi_i\rangle\right|^2 \times \sum_{\nu_i,\nu_f} e^{-\frac{E_{ij}}{k_B T}}\left|\langle\Theta_{i,\nu_i}|\Theta_{f,\nu_f}\rangle\right|^2\delta\left(E_{i\nu_i} - E_{f\nu_f}\right) \qquad \textbf{(3.117)}$$

Here E_{ij} corresponds to the total energy of a specific vibrational level j within a given electronic state i. In this framework, the SOC matrix element between the initial and final electronic states is included, along with a Dirac delta function that ensures energy conservation between vibrational levels of the two electronic states.

Chapter 4: Computational Investigation of Neutral BODIPY Dyes

4.1 Introduction

The development of a water-splitting two-compound system based on BODIPY dye chromophores requires a thorough understanding of the underlying electronic states involved in the process. As a first step, it is necessary to evaluate the photochemical behavior of this dye upon photoexcitation in the Franck–Condon region and the subsequent relaxation pathways. Previous studies have primarily focused on the lowest singlet and triplet states of BODIPY dyes, particularly their vertical excitation energies, 0–0 transitions, and evaluation of radiative photophysical properties [157–159]. However, investigations addressing higher singlet and triplet states remain scarce [160, 161]. The role of highly excited charge-transfer states is still contentious, particularly with respect to whether they promote activation or deactivation pathways. To tackle this concern, TDDFT calculations on the higher electronic states have been carried out and validated against ab initio DLPNO-STEOM-CCSD results. The results of this investigation were published in the reference [162]: A. Sbai, and J. Guthmuller, Phys. Chem. Chem. Phys. **26** (2024) 25925-25935, *Singlet and triplet excited states of a series of BODIPY dyes as calculated by TDDFT and DLPNO-STEOM-CCSD methods*. However, for convenience the present chapter provides a description of the main results and conclusions.

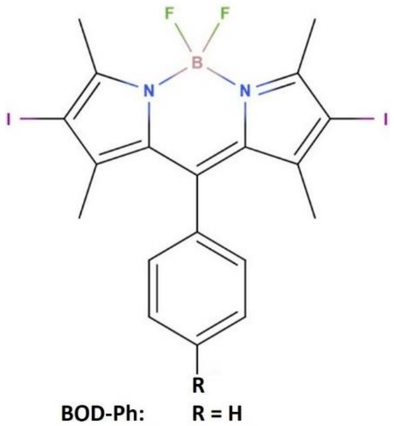

BOD-Ph: **R = H**
BOD-PhNO$_2$: **R = NO$_2$**
BOD-PhOH: **R = OH**

Figure 4.1: Structures of the investigated BODIPY compounds.

4.2 Singlet and triplet excited states of BOD-Ph at the S_0 geometry in a vacuum

The ground-state (S_0) geometry was optimized using the B3LYP exchange–correlation (XC) functional. Subsequently, single-point excited-state calculations were performed at the S_0 geometry of BOD-Ph (**Figure 4.1**) employing TDA-TDDFT with the B3LYP, MN15, SOS-PBE-QIDH, and SOS-ωPBEPP86 functionals. Since TDDFT methods have limitations in accurately capturing certain electronic effects, and vertical excitation energies are often poorly estimated within the TDDFT framework for specific cases. Therefore, benchmarking against high-level wavefunction-based methods is necessary. In this regard, DLPNO-STEOM-CCSD is particularly relevant, as it has been shown in previous studies to reproduce experimental absorption energies for the S_1 state of BODIPY dyes, with deviations of less than 0.1 eV [163]. The use of the TDA is further justified, as it enhances the numerical stability of triplet states and generally yields more reliable results compared to conventional TDDFT in this context [164, 165].

The lowest vertical excitation energies of the bright singlet state (S_1) and the dark triplet state (T_1), both corresponding to the $\pi_{BOD} \rightarrow \pi_{BOD}^*$ transition, are summarized in **Table 4.1**. The evaluation of these states is critical, as they play a central role in the photocatalytic activity cycle. Upon photoexcitation in the FC region, ISC from S_1 to the long-lived T_1 state can occur. Notably, TDA-TDDFT predicts vertical excitation energies that are systematically higher by about 0.3–0.7 eV compared to conventional TDDFT, in agreement with a previous report [159].

For the S_1 state, MN15 yields the highest excitation energy (3.02 eV), which can be attributed to its relatively large fraction of exact HF exchange (44%) in the XC functional. In contrast, the double-hybrid functionals SOS-PBE-QIDH and SOS-ωPBEPP86 yield lower vertical excitation energies compared to both MN15 and B3LYP. The comparison with experimental results obtained in dichloromethane (DCM) is justified, since the solvatochromic shift of the S_1 state is known to be small for BODIPY dyes (<0.1 eV) [159]. Among the methods tested, DLPNO-STEOM-CCSD provides the best accuracy overall, although it underestimates the vertical excitation energy by about 0.2 eV. This discrepancy is likely related to its truncation nature that neglects higher-order correlation effects. By contrast, among the TDA-TDDFT methods, SOS-ωPBEPP86 shows the closest agreement with experiment, albeit with an overestimation of ~0.3 eV relative to experiments. This performance can be ascribed to the MP2-based correction included in this functional, which accounts for doubly excitations. For the T_1 triplet state, the excitation energies calculated with TDA-TDDFT methods, benchmarked against DLPNO-STEOM-CCSD, show that MN15 provides the best agreement, with a deviation of about 0.2 eV.

Table 4.1 Vertical excitation energies (VEE), wavelengths (λ), oscillator strengths (f) of the lowest singlet (S_1) and lowest triplet (T_1) excited states calculated at the S_0 geometry with different methods in a vacuum.

	S_1 state			T_1 state	
Method	VEE (eV)	λ (nm)	f	VEE (eV)	λ (nm)
B3LYP	2.70	459	0.396	1.50	826
TDA B3LYP	2.88	430	0.372	1.62	768
TDA MN15	3.02	410	0.736	1.59	779
TDA SOS-PBE-QIDH	2.73	455	0.922	1.77	700
TDA SOS-ωPBEPP86	2.65	468	0.890	1.69	735
DLPNO-STEOM-CCSD	2.09	594	0.543	1.38	902
Exp.[a]	2.32	534			

[a] Experimental absorption maximum in DCM from ref [31].

An assessment of the accuracy of the vertical excitation energies of the 11 singlet and 12 triplet states, which may participate in the hydrogen production cycle, was performed by calculating the mean absolute deviations (MADs) for various functionals with the def2-SVP basis set, in comparison to the corresponding ab initio method (**Table 4.2**). Using the double-ζ def2-SVP basis set, the MN15 functional provides the lowest MAD values, 0.248 eV for the singlet states and 0.241 eV for the triplet states. In contrast, the double-hybrid functional SOS-ωPBEPP86 exhibits the largest deviations, with MADs of 0.314 eV (singlets) and 0.376 eV (triplets). However, when SOS-ωPBEPP86 is combined with the larger def2-TZVP basis set, the energies of CT and $\pi_{BOD} \rightarrow \sigma_I^*$ states decrease, leading to a significantly improved accuracy, with an MAD of 0.151 eV for the singlet states.

This analysis suggests that MN15 is not necessarily the most accurate overall, but it provides a balanced description at a lower computational cost. Moreover, unlike the double-hybrid functionals and the DLPNO-STEOM-CCSD method, MN15 also enables the optimization of excited-state geometries, which is an additional advantage.

Table 4.2 Mean absolute deviations (MAD) of TDA-TDDFT energies in comparison to DLPNO-STEOM-CCSD for the selected singlet and triplet states.

Method	Singlet MAD (eV)	Triplet MAD (eV)
B3LYP	0.543	0.478
TDA B3LYP	0.527	0.465
TDA MN15	0.248	0.241
TDA SOS-PBE-QIDH	0.197	0.257
TDA SOS-ωPBEPP86	0.314 (0.151[a])	0.376 (0.227[a])

[a] MAD for SOS-ωPBEPP86 calculated with the def2-TZVP basis set.

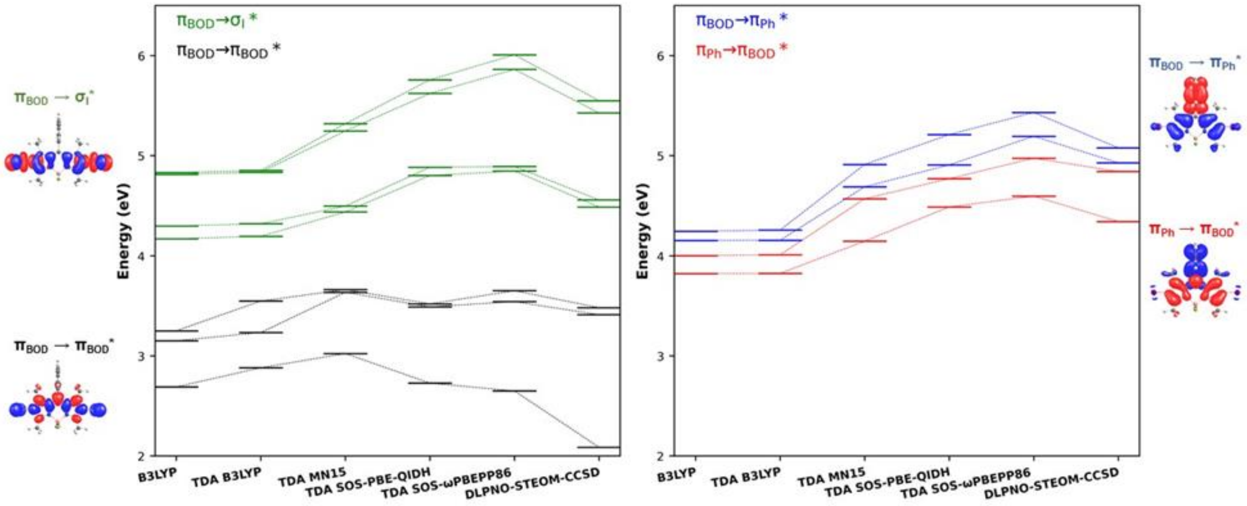

Figure 4.2: Singlet states vertical energy diagrams of BOD-Ph. Examples of charge density difference (CDD) for the different types of transitions, positive (electron) and negative (hole) values are indicated in red and blue colors, respectively.

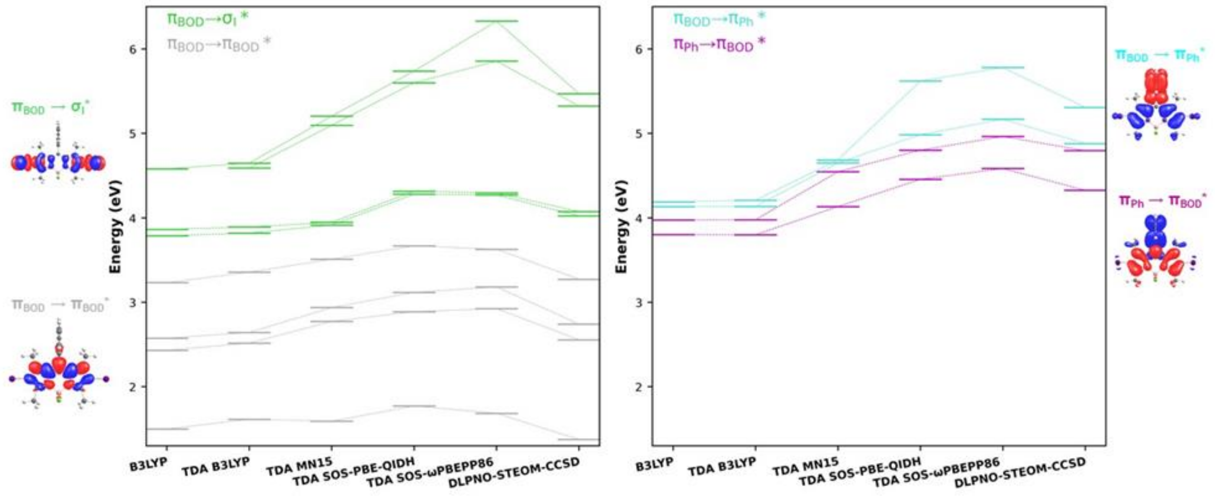

Figure 4.3: Triplet states vertical energy diagrams of BOD-Ph. Examples of charge density difference (CDD) for the different types of transitions, with positive (electron) and negative (hole) values, are indicated in red and blue colors, respectively.

Upon photoexcitation, the S_1 state is populated with an oscillator strength of f = 0.736 (MN15), which corresponds to the main absorption band observed in the experimental spectrum. The S_2 and S_3 states exhibit oscillator strengths of f = 0.067 and f = 0.496, respectively, indicating that secondary absorption bands are also likely.

Following photoexcitation, the relative energies of the singlet and triplet states determine which states are thermodynamically accessible for population. This simplified evaluation neglects the influence of energy barriers (transition states), electronic couplings (SOC and NACs), and possible conical intersections between states.

At first glance, it is evident that the long-lived triplet states with $\pi_{BOD} \rightarrow \pi_{BOD}^*$ character can be populated from the S_1, S_2, and S_3 states via ISC. In contrast, CT and dissociative states lie above 4 eV, indicating that these states are energetically inaccessible (**Figures 4.2** and **4.3**). However, this remains a limited observation, since the calculations were performed in the gas phase, whereas in realistic conditions factors such as substituents and solvent effects may significantly alter the energetic pathways.

4.3 Effects of the solvent and of substitution with OH and NO_2 groups

The MN15 XC functional was employed to investigate how substitution of the phenyl ring in BOD-Ph with either an EDG (OH) or an EWG (NO_2) influences the vertical excitation energies, and solvent effects were included by modeling DCM with the PCM approach (**Figures 4.4** and **4.5**). Initially, the S_0 geometry was optimized both in the gas phase and in solution. The key (BODIPY core)-phenyl rotational torsion obtained from this optimization differs by 11.8° compared to the geometry optimized with B3LYP. This deviation affects the CT and $\pi_{BOD} \rightarrow \pi_{BOD}^*$ transitions by less than 0.1 eV, whereas the $\pi_{BOD} \rightarrow \sigma_I^*$ excitation energies show differences of up to 0.17 eV.

The $\pi_{BOD} \rightarrow \pi_{BOD}^*$ and $\pi_{BOD} \rightarrow \sigma_I^*$ states are localized on the BODIPY core; thus, they are barely influenced by the substituents (NO_2 and OH) and the solvent, exhibiting only a subtle shift of about 0.1 eV. In contrast, the CT states are significantly affected by these factors. Specifically, the implicit interaction of the solute with the surrounding medium stabilizes all singlet and triplet $\pi_{Ph} \rightarrow \pi_{BOD}^*$ CT states (by up to 0.49 eV for the singlet states of BOD-PhNO$_2$), while it increases the energy of $\pi_{BOD} \rightarrow \pi_{Ph}^*$ CT states, with the singlet states of BOD-PhOH shifted upward by a maximum of 0.35 eV, relative to the vacuum reference. Furthermore, the attachment of an EDG (OH) or an EWG (NO_2) at the para position of the phenyl ring produces even more pronounced effects on the vertical excitation energies compared to unsubstituted BOD-Ph. Specifically, the lowest singlet and triplet $\pi_{Ph} \rightarrow \pi_{BOD}^*$ CT states are shifted downward upon OH substitution, with a maximum stabilization of 0.74 eV for the triplet state in DCM, whereas the $\pi_{BOD} \rightarrow \pi_{Ph}^*$ CT states are significantly destabilized. A reverse trend is observed upon NO_2 substitution. The most pronounced effect is found for the lowest singlet and triplet $\pi_{BOD} \rightarrow \pi_{Ph}^*$ CT states, which are stabilized by 1.54 and 1.51 eV, respectively, relative to BOD-Ph.

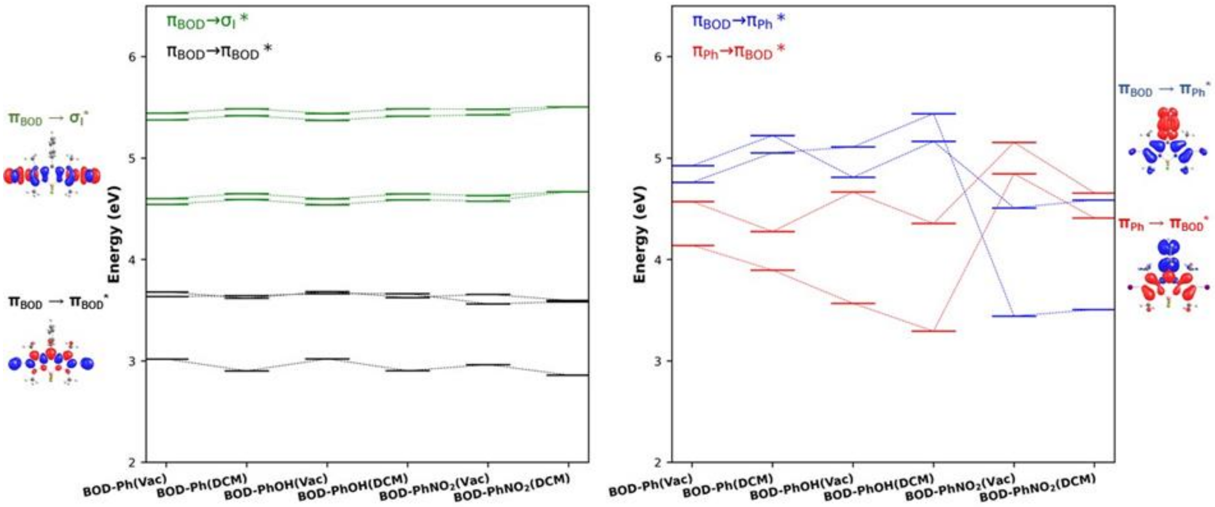

Figure 4.4: Singlet states vertical energy diagrams of BOD-Ph, BOD-PhOH, and BOD-PhNO$_2$ in vacuum and DCM calculated at the S_0 geometries with TDA-TDDFT (MN15), including CDD for the transitions.

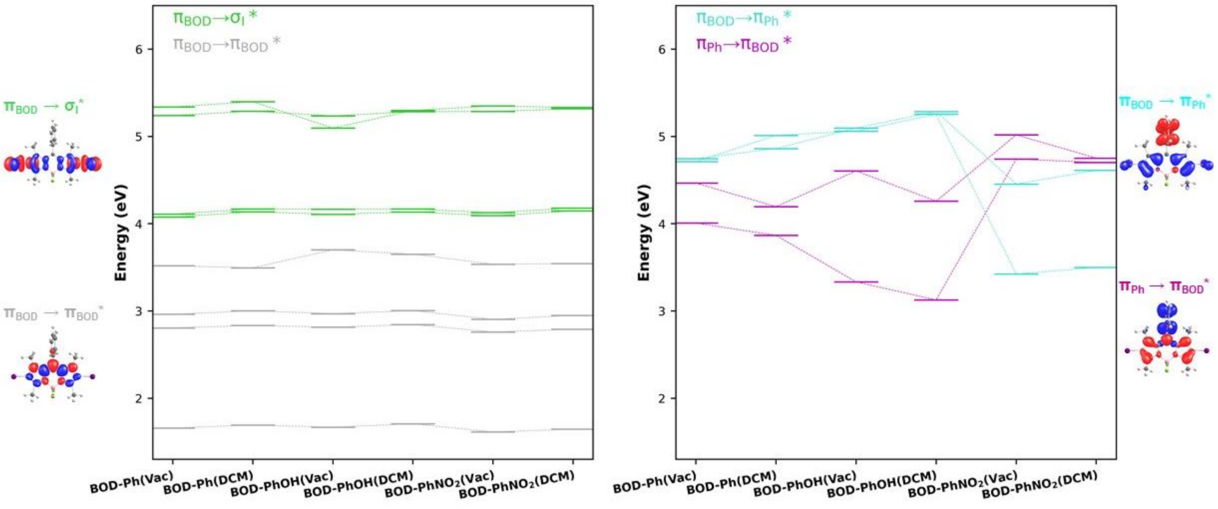

Figure 4.5: Triplet states vertical energy diagrams of BOD-Ph, BOD-PhOH and BOD-PhNO$_2$ in vacuum and DCM calculated at the S_0 geometries with TDA-TDDFT (MN15). including CDD for the transitions

Although these results demonstrate that the interplay between solvent effects and substitution leads to the stabilization of CT states, such states remain inaccessible from the S_1 state $\pi_{BOD} \rightarrow \pi_{BOD}^*$. For BOD-PhOH, the lowest singlet and triplet $\pi_{Ph} \rightarrow \pi_{BOD}^*$ states lie 0.39 and 0.23 eV above S_1 in DCM, respectively. In contrast, for BOD-$PhNO_2$, the lowest singlet and triplet $\pi_{BOD} \rightarrow \pi_{Ph}^*$ CT states are separated from S_1 by 0.65 and 0.64 eV in DCM, respectively.

The compound also exhibits a second absorption band, which lies energetically above the CT states of interest. For BOD-PhOH, this band is higher by 0.34–0.50 eV, whereas for BOD-$PhNO_2$ the difference is 0.07–0.08 eV. Consequently, the population of these CT states becomes possible upon excitation into the higher-lying band. A complete understanding of geometrical relaxation in the excited states is therefore essential for accurately interpreting the energetics of the non-radiative processes, as it defines the PES at its minima and helps prevent erroneous conclusions.

4.4 Relaxation pathways for non-reduced BODIPY dyes

To assess whether the energy levels undergo significant alterations upon structural relaxation and to clarify whether this relaxation facilitates reductive activation of the catalyst or instead inhibits electron transfer, the excited-state geometries of the three compounds were optimized using the MN15 functional in DCM. TDA-TDDFT single-point calculations were then performed within the equilibrium PCM framework, in contrast to the non-equilibrium approach employed for the vertical energy calculations discussed previously. **Figure 4.6** presents the energy diagrams for the S_0 state and the S_1 $\pi_{BOD} \rightarrow \pi_{BOD}^*$ state, as well as for the lowest singlet and triplet $\pi_{Ph} \rightarrow \pi_{BOD}^*$ and $\pi_{BOD} \rightarrow \pi_{Ph}^*$ CT states. Vibrational frequency analyses confirmed that all optimized geometries correspond to true minima on the PES, as no imaginary frequencies were found. For BOD-$PhNO_2$, the geometry optimization of the lowest singlet $\pi_{Ph} \rightarrow \pi_{BOD}^*$ CT state did not converge to a minimum and is therefore omitted.

At first glance, it is evident that the earlier conclusion, namely, that the CT states may be populated via excitation into the second absorption band, remains valid for the BOD-PhOH and BOD-$PhNO_2$ derivatives, whereas in BOD-Ph these states remain energetically higher.The S_1 state energy decreases slightly (< 0.1 eV) upon geometrical relaxation for all dyes, consistent with the typically small Stokes shifts observed for BODIPY dyes. In contrast, relaxation has a more pronounced effect on the CT states, with the singlet and triplet CT states decreasing in energy by 0.24 and 0.23 eV, respectively. Nevertheless, in BOD-Ph these states remain energetically inaccessible from S_1, as the lowest singlet and triplet CT states lie 0.75 and 0.77 eV above S_1, respectively.

The incorporation of the EWG into BOD–$PhNO_2$ induces a stabilization of the charge-transfer states $\pi_{BOD} \rightarrow \pi_{Ph}^*$ by 0.44 eV (singlet) and 0.42 eV (triplet) when compared at their optimized geometries relative to the S_0 equilibrium structure. However, the driving force (ΔG), estimated as the electronic energy difference between the S_1 minimum and the corresponding CT minima for the transitions $S_1 \rightarrow S(\pi_{BOD} \rightarrow \pi_{Ph}^*)$ and $S_1 \rightarrow T(\pi_{BOD} \rightarrow \pi_{Ph}^*)$, amounts to 0.51 and 0.49 eV, respectively. These positive energy gaps indicate that the population of the CT states from S_1 is not energetically favorable, thus rendering this pathway non-viable. While the CT states $\pi_{Ph} \rightarrow \pi_{BOD}^*$ feature a significant increase in energy, as concluded in the previous section.

For BOD-PhOH, the opposite behavior is observed, manifested by a stabilization of the ($\pi_{Ph} \rightarrow \pi_{BOD}^*$) states upon relaxation from the S_0 to the CT geometries, amounting to 0.26 eV (singlet) and 0.45 eV (triplet). The corresponding driving forces (ΔG), defined as the energy difference between the S_1 minimum and these CT minima, are 0.33 eV and 0.00 eV, respectively, which indicates the possibility of population of the $T(\pi_{Ph} \rightarrow \pi_{BOD}^*)$.

To evaluate the robustness of these results, we recomputed the single-point energies for BOD-PhOH at the DLPNO-STEOM-CCSD level of theory, using geometries optimized at the MN15 level. Overall, a similar trend was obtained. In contrast to MN15, which underestimates the energy of CT states (see part **4.2**) and thus predicts an accessible energetic barrier, DLPNO-STEOM-CCSD yields significantly larger ΔG of 0.65 eV and 0.43 eV for the $S_1 \rightarrow S(\pi_{Ph} \rightarrow \pi_{BOD}^*)$ and $S_1 \rightarrow T(\pi_{Ph} \rightarrow \pi_{BOD}^*)$ transitions, respectively. Therefore, contrary to the MN15 predictions, the ($\pi_{Ph} \rightarrow \pi_{BOD}^*$) states are energetically inaccessible at the DLPNO-STEOM-CCSD level.

Although the CT states of BOD-$PhNO_2$ and BOD-PhOH are not directly accessible from the S_1 minima, they are located only slightly above the S_1 state at their respective optimized geometries. Because the magnitude of the energy gap depends sensitively on the choice of correlation functional used to approximate the total energy, and given that even coupled-cluster methods may provide an incomplete treatment of correlation effects with errors on the order of 0.1–0.2 eV, CT states may indeed be energetically accessible in these compounds.However, the total energy diagram indicates that decay from the S_1 to the T_1 state is feasible, with a ΔG of about 1.07 eV. Thus, CT states will inevitably compete with the population of T_1 state for BOD-$PhNO_2$ and BOD-PhOH dyes. If the hypothesis that the population of the long-lived T_1 state is the key factor for catalyst reduction is correct, then the decreased turnover number of H_2 production in BOD-PhOH and BOD-$PhNO_2$ can be ascribed to the possibility of the population of CT states.

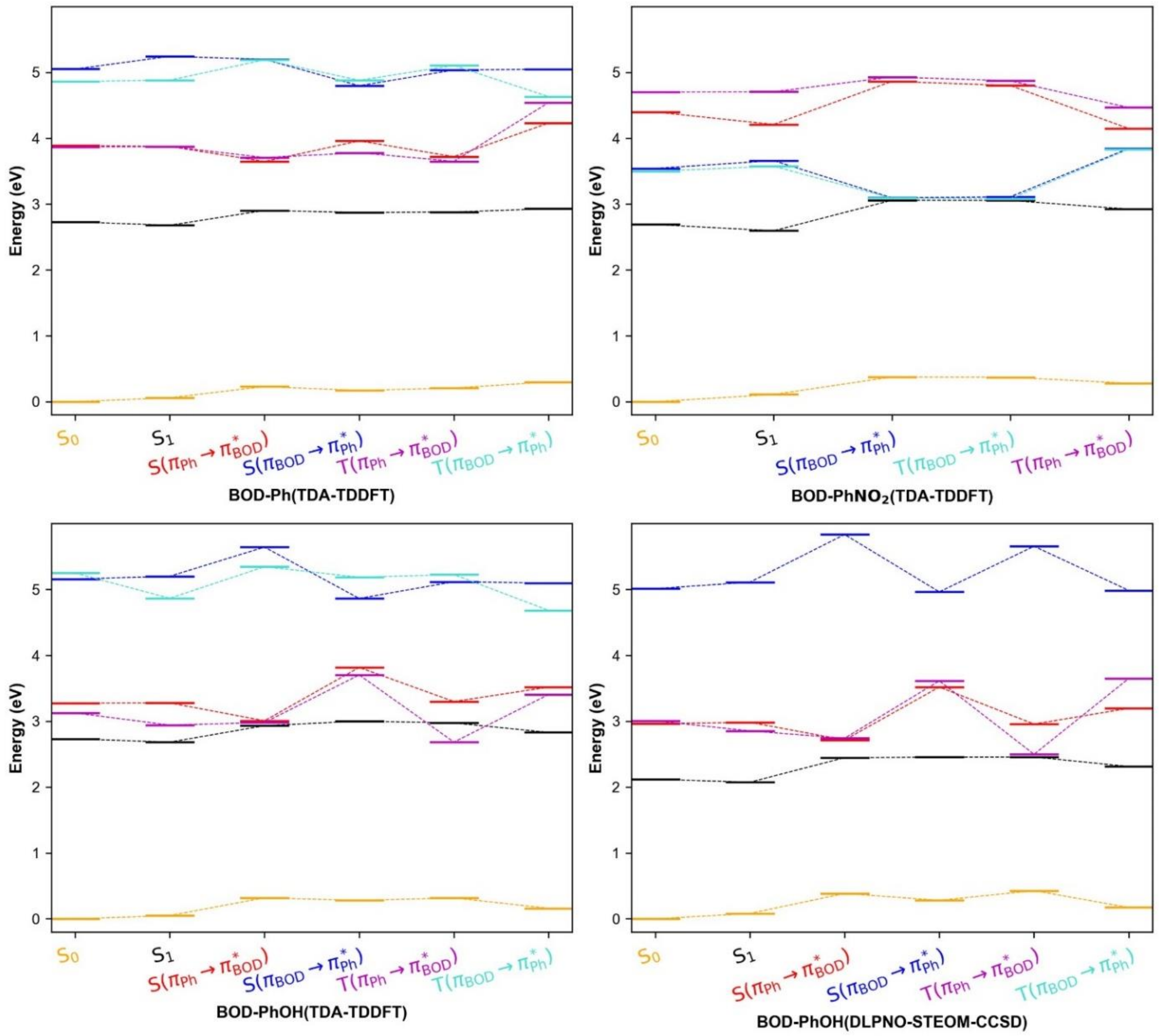

Figure 4.6: Energy diagrams for selected singlet and triplet states of BOD-Ph, BOD-PhOH, and BOD-$PhNO_2$. The calculations were performed at different geometries in DCM with TDA-TDDFT (MN15) and DLPNO-STEOM-CCSD.

4.5 Conclusion

MN15 shows good performance compared to DLPNO-STEOM-CCSD method, in contrast to double-hybrid functionals, which are highly sensitive to basis set errors and computationally more costly. This study emphasizes that CT states act as impediments to catalytic activity, whereas ISC between S_1 and T_1 promotes catalytic activation, with the latter likely dominating in the process for the three compounds. Thus, only a partially correlation between electron transfer pathways and the experimental turnover frequencies [31] is observed for BOD-PhOH and BOD-$PhNO_2$. To obtain an overall picture of the mechanism, the doublet CT states should be evaluated.

Chapter 5: Computational Results for the Reduced BODIPY Dyes

5.1 Introduction

Electronic states exhibiting doublet character are a subject of significant scientific interest and ongoing debate due to their promising applications across diverse research domains. These states play a pivotal role in several advanced technologies. Such states are central to enhancing the efficiency of proton reduction systems via redox-mediated processes [166] and to singlet fission, where doublet charge-transfer states can act as intermediates facilitating the generation of triplet excitons [167]. They also play key roles in thermally activated delayed fluorescence materials employing radical emitters through singlet–doublet electron transfer [168], in organic radical batteries that rely on rapid electron transfer [169], and in nonlinear optical spectroscopy under polarized light excitation [170]. These phenomena often involve materials such as organic radicals, which inherently exhibit an open-shell structure [171], and transition metal complexes, where interactions between unpaired d- or f-electrons and ligand-centered radicals give rise to doublet excited states [172].

Coupled-cluster methods are highly accurate for closed-shell systems, but they often struggle for open-shell species, especially when a strong multireference character is present. Their canonical costs, $\mathcal{O}(\mathrm{N}^6)$ for CCSD and $\mathcal{O}(\mathrm{N}^7)$ for CCSD(T), together with substantial memory demands, limit routine applications to modest system sizes. Multiconfigurational approaches (e.g., CASSCF followed by CASPT2 or NEVPT2) provide viable alternatives for systems with pronounced static correlation (including many open-shell doublets), but they require careful active-space selection and method-specific parameter choices [173]. Therefore, the results can be sensitive to these decisions. Spin-flip methods such as SF-EOM-CCSD can be effective for diradicals and bond-breaking by using a high-spin reference [174], yet, as truncated singles-and-doubles models, they may miss important higher-excitation effects (triples, quadruples). Their performance is also reference-state dependent, which limits their reliability to a relatively narrow class of problems.

Compared with correlated wave-function methods, DFT offers favorable computational cost owing to its parameterized nature. In the reference [142], the authors investigated doublet–

doublet excitation energies for 23 radical species, excluding states with pronounced multiconfigurational character. TDDFT calculations were carried out with both hybrid and double-hybrid functionals, and the results were benchmarked against UCC3/aug-cc-pVTZ using MADs. Among the tested functionals, the spin-opposite-scaled, range-separated double-hybrid SOS-ωPBEPP86 was among the best performers, yielding a MAD of 0.17 eV.

Although TDDFT has achieved considerable success in describing the electronic properties of singlet and triplet excited states, it faces significant challenges when applied to doublet states. These difficulties arise primarily from its inherent single-determinant framework and the limitations of the adiabatic approximation, particularly in the case of CT excitations, where the overlap between ground and excited states diminishes, and spin contamination becomes prominent. Despite these limitations, certain functionals, such as MN15 and SOS-ωPBEPP86, have shown promising performance and offer a balanced description for selected open-shell systems. While MN15 has demonstrated good accuracy for multireference states, and those involving Rydberg character [134], its application to doublet excitations remains relatively underexplored in the literature.

In general, the hydrogen production cycle involving BODIPY dyes as PSs is controversial. Two different hypotheses have been proposed to explain the cycle of hydrogen production involving reduced BOD-Ph compounds (see description in the introduction):

The first hypothesis [33] proposes that an electron released from the SED (e.g., ascorbic acid) occupies the LUMO of the bright singlet BOD-Ph state, resulting in a reduced form with a doublet ground state (S = 1/2). Upon photoexcitation of the reduced BOD-Ph, two primary pathways may occur: either a CT state is formed, leading to hydrogen production after electron transfer toward the catalyst, or a dissociative state arises, causing degradation of the compound. Indeed, a previous study [33] performed a TDDFT-PES relaxed scan along the torsional coordinate of the reduced BOD-Ph compound, using the PBE0/cc-pVTZ level of theory. This study indicated the potential for the population of the reduced charge-transfer state in BOD-Ph, while the PES along the carbon–iodine bond elongation was associated with a dissociative state, leading to cleavage of the compound.

The second hypothesis [175] suggests that the photoexcitation of the reduced compound populates a long-lived doublet state (centered on the BODIPY core), which is then followed by electron transfer to the catalytic center. In this hypothesis, the competing population of CT states is assumed to act as a deactivation channel and thus to hinder hydrogen production.

Therefore, in the present study, we employed the TDA within TDDFT to investigate doublet states that may be relevant to the reduced BOD-Ph cycles involved in hydrogen production. This approach offers a computationally efficient yet informative route to explore such states in complex molecular systems.

The initial phase of this study comprises a systematic comparison between TDA-TDDFT calculations on reduced BOD-Ph employing the meta-hybrid functional MN15 and the double-hybrid functionals SOS-PBE-QIDH and SOS-ωPBEPP86. The double-hybrid functionals incorporate MP2-like perturbative correlation to enhance the description of dynamical correlation effects in doublet states. Both methodologies are benchmarked against a high-level multiconfigurational wavefunction reference method (RASPT2) for excited states properties calculations of the relevant doublet states taken from the reference [33]. Ground state (D_0) geometry optimization was performed in the gas phase at the MN15/def2-SVP level, followed by vibrational frequency analysis and subsequent single-point TDA-TDDFT energy evaluations.

The second stage of the investigation examines the influence of solvation (DCM modeled with PCM) and electronic substituent effects (NO_2 and OH) on energy levels, oscillator strengths, and state-level ordering. This makes it possible to address certain experimental aspects that may influence the reduced states.

In the third step, the excited doublet states geometries relevant to the catalytic pathway are optimized. At each optimized geometry, TDDFT calculations determine the total electronic energies. These results enable qualitative comparison of the potential energy surfaces, facilitating the identification of active versus inactive reaction channels among the three molecular structures following photoexcitation.

5.2 Spin density

The spin density map is generated to localize the electron density of the unpaired electron. It is evident from **Figure 5.1** that the unpaired electron is predominantly on the SOMO of BOD-Ph (corresponding to the LUMO of the non-reduced compound).

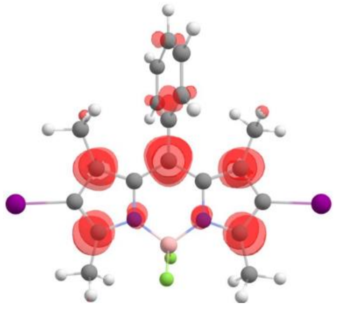

Figure 5.1: Spin density for the reduced BOD-Ph.

5.3 Effect of XC functionals on the reduced BODIPY dyes' energy levels

The properties of the ten lowest-lying doublet excited states of BOD-Ph were investigated using unrestricted density functional theory coupled with TDA-TDDFT calculations. Three XC functionals were tested, namely MN15, SOS-PBE-QIDH, and SOS-ωPBEPP86, which represent functionals from the fourth and fifth rungs of Jacob's ladder, and they were benchmarked against RASPT2 calculations from the reference [33]. The ground-state geometry (D_0) was optimized at the MN15/def2-SVP level in vacuum and employed for all subsequent TDA-TDDFT calculations. For MN15, TDA-TDDFT is also evaluated in comparison with conventional TDDFT. The optimized structure has a phenyl-(BODIPY core) torsion angle of approximately 115.95°.

The energies of the lowest excited states that may be relevant to the catalytic process are listed in **Table 5.1** and include:
D($\pi_{BOD} \rightarrow \pi^*_{BOD}$): localized within the BODIPY core and containing the unpaired electron.
D($\pi_{BOD} \rightarrow \pi^*_{Ph}$): doublet excitation that facilitates electron transfer from the BODIPY core to the phenyl moiety.
D($\pi_{BOD} \rightarrow \sigma_I^*$): associated with compound degradation via carbon–iodine bond cleavage.
D($\pi_{Ph} \rightarrow \pi^*_{BOD}$): electron transfer from the phenyl to the BODIPY core.

As presented in **Table 5.1**, TDA-TDDFT/MN15 calculations introduce a slight blueshift of ~0.05 eV relative to standard TDDFT/MN15. However, moderate discrepancies are observed in the computed oscillator strengths (f). Notably, the bright D($\pi_{BOD} \rightarrow \pi^*_{BOD}$) exhibits a substantial orbital contribution (49%) from the D($\pi_{BOD} \rightarrow \pi^*_{Ph}$) state in TDDFT calculations, considerably higher than the 18% contribution found using TDA-TDDFT. Furthermore, upon photoexcitation, absorption to the bright D($\pi_{BOD} \rightarrow \pi^*_{BOD}$) state ($f = 0.116$) and to the two low-lying $D(\pi_{BOD} \rightarrow \pi^{*}_{Ph})$ CT states (f = 0.055; 0.060) is allowed, indicating that population of both localized and CT states is possible.

Table 5.1 Excited states (TDA)-TDDFT(MN15/def2-SVP) for BOD-Ph. Vertical excitation energies (VEE), oscillator strength (f), spin ($<S^2>$).

	TDDFT/MN15			TDA-TDDFT/MN15		
States	VEE(eV)	f	$<S^2>$	VEE(eV)	f	$<S^2>$
$D(\pi_{BOD} \rightarrow \pi^{*}_{Ph})$	2.43	0.055	0.82	2.48	0.070	0.80
$D(\pi_{BOD} \rightarrow \pi^{*}_{Ph})$	2.44	0.060	0.80	2.48	0.020	0.80
$D(\pi_{BOD} \rightarrow \pi^{*}_{BOD})$	2.56	0.116	0.79	2.64	0.187	0.80
$D(\pi_{BOD} \rightarrow \sigma_{I}^{*})$	2.74	0.001	0.96	2.75	0.002	0.96
$D(\pi_{BOD} \rightarrow \sigma_{I}^{*})$	2.86	0.001	1.01	2.87	0.001	1.00
$D(\pi_{BOD} \rightarrow \pi^{*}_{BOD})$	3.37	0.005	0.84	3.42	0.003	0.84
$D(\pi_{BOD} \rightarrow \pi^{*}_{BOD})$	3.54	0.000	0.90	3.62	0.000	0.87
$D(\pi_{BOD} \rightarrow \pi^{*}_{BOD})$	3.73	0.034	1.45	3.85	0.029	1.07
$D(\pi_{BOD} \rightarrow \sigma_{I}^{*})$	3.86	0.003	2.11	3.90	0.001	2.31
$D(\pi_{BOD} \rightarrow \sigma_{I}^{*})$	3.88	0.000	2.23	3.94	0.000	2.41

Table 5.2 presents MADs for the four lowest excited states relative to the RASPT2 reference. The $D(\pi_{BOD} \rightarrow \pi^{*}_{Ph})$ transition (RASPT2 energy: 2.11, 3.54 eV) was excluded from the MADs calculation due to its strong mixing with the $D(\pi_{BOD} \rightarrow \pi^{*}_{BOD})$ state. MN15 yields the smallest MAD (0.08 eV), while SOS-PBE-QIDH and SOS-ωPBEPP86 exhibit larger deviations of 0.33 eV and 0.41 eV, respectively, even with employing a large basis set (def2-TZVP). Although TDA-TDDFT with MN15 generally provides a balanced description, it exhibits limitations for CT states. Specifically, in contrast to RASPT2 (**Table 5.3**), TDDFT predicts two nearly degenerate low-lying $D(\pi_{BOD} \rightarrow \pi^{*}_{BOD})$ states at 2.43 and 2.44 eV with MN15. This disagreement is likely related to the limitation of TDDFT in describing static correlation effects.

The study of the non-reduced compound showed that the CT excitations were underestimated by a MAD of 0.22 eV using the MN15 functional and overestimated by a MAD of 0.10 eV with the SOS-ωPBEPP86 functional. However, for the reduced BOD-Ph, CT states remain particularly challenging to describe, even with the inclusion of long-range corrections. Furthermore, higher spin contamination is observed when using the double-hybrid functionals (**Table 5.4**), which may impact the accuracy of the results.

Table 5.2 Mean absolute deviation (MAD) in eV of TDA-TDDFT in comparison to RASPT2.

States	TDDFT-MN15	TDA-TDDFT MN15	SOS-ωPBEPP86	SOS PBE-QIDH
$D(\pi_{BOD} \rightarrow \pi^{*}_{BOD})$	0.05	0.11	0.37	0.36
$D(\pi_{BOD} \rightarrow \sigma_{I}^{*})$	0.10	0.10	0.45	0.50
Average	0.08	0.10	0.41	0.33

Table 5.3 Excited state properties with RASPT2 method [33] with C_{2v}-restricted structure.

RASPT2		
States	VEE(eV)	f
$D(\pi_{BOD} \rightarrow \pi^{*}_{Ph})$	2.11	0.000
$D(\pi_{BOD} \rightarrow \pi^{*}_{BOD})$	2.49	0.183
$D(\pi_{BOD} \rightarrow \sigma_{I}^{*})$	2.58	0.000
$D(\pi_{BOD} \rightarrow \sigma_{I}^{*})$	2.83	0.000
$D(\pi_{BOD} \rightarrow \pi^{*}_{BOD})$	3.35	0.010
$D(\pi_{BOD} \rightarrow \pi^{*}_{Ph})$	3.54	0.150

Table 5.4 TDA-TDDFT calculations with double hybrid functionals (SOS-ωPBEPP86, SOS-PBEQIDH/def2-TZVP).

TDA-TDDFT (SOS-ωPBEPP86)				TDA-TDDFT (SOS-PBE-QIDH)			
States	VEE(eV)	f	$<S^2>$	States	VEE(eV)	f	$<S^2>$
$D(\pi_{BOD} \rightarrow \pi^{*}_{BOD})$	2.67	0.198	1.02	$D(\pi_{BOD} \rightarrow \pi^{*}_{BOD})$	2.69	0.198	0.99
$D(\pi_{BOD} \rightarrow \pi^{*}_{Ph})$	3.13	0.039	1.19	$D(\pi_{BOD} \rightarrow \pi^{*}_{Ph})$	2.87	0.032	1.06
$D(\pi_{BOD} \rightarrow \sigma_{I}^{*})$	3.28	0.000	1.98	$D(\pi_{BOD} \rightarrow \pi^{*}_{Ph})$	3.02	0.031	1.54
$D(\pi_{BOD} \rightarrow \pi^{*}_{Ph})$	3.35	0.019	3.35	$D(\pi_{BOD} \rightarrow \sigma_{I}^{*})$	3.08	0.000	1.71
$D(\pi_{BOD} \rightarrow \sigma_{I}^{*})$	3.40	0.000	2.15	$D(\pi_{BOD} \rightarrow \sigma_{I}^{*})$	3.24	0.000	1.89
$D(\pi_{BOD} \rightarrow \pi^{*}_{Ph})$	3.63	0.065	1.87	$D(\pi_{BOD} \rightarrow \pi^{*}_{Ph})$	3.81	0.052	2.19
$D(\pi_{BOD} \rightarrow \pi^{*}_{BOD})$	3.89	0.111	1.27	$D(\pi_{BOD} \rightarrow \pi^{*}_{BOD})$	3.86	0.008	1.45
$D(\pi_{BOD} \rightarrow \pi^{*}_{BOD})$	3.93	0.020	1.43	$D(\pi_{BOD} \rightarrow \pi^{*}_{BOD})$	3.98	0.000	1.65
$D(\pi_{BOD} \rightarrow \pi^{*}_{BOD})$	3.98	0.001	1.69	$D(\pi_{BOD} \rightarrow \pi^{*}_{BOD})$	4.02	0.001	1.74
$D(\pi_{BOD} \rightarrow \pi^{*}_{Ph})$	4.03	0.018	1.66	$D(\pi_{BOD} \rightarrow \sigma_{I}^{*})$	4.04	0.000	1.80

5.4 Effect of the substituents and the solvent on the reduced BODIPY dyes' energy levels

The MN15 XC functional was employed to investigate the influence of substituting the phenyl group with an EDG (OH) or an EWG (NO_2). The effect of DCM solvent was accounted for using the implicit PCM within the LR formalism to improve the accuracy of excited-state calculations. The electronic properties of the compounds (BOD-Ph, BOD-PhOH, and BOD-$PhNO_2$) are summarized in **Tables 5.5–5.7**. Upon transitioning from vacuum to solvent surroundings, it was found for BOD-Ph that the low-lying states $D(\pi_{BOD} \rightarrow \pi^{*}_{BOD})$ and $D(\pi_{BOD} \rightarrow \sigma_{I}^{*})$ are slightly destabilized by 0.07 and 0.18 eV, respectively. However, the effect of the solvent is more pronounced on the higher energy $D(\pi_{BOD} \rightarrow \pi^{*}_{Ph})$ and $D(\pi_{Ph} \rightarrow \pi^{*}_{BOD})$ states, causing energy shifts of +0.46 eV and −0.41 eV, respectively (**Figure 5.2**). Subsequently, the attachment of a NO_2 group to the phenyl ring results in a significant decrease in the vertical transition energy of the $D(\pi_{BOD} \rightarrow \pi^{*}_{Ph})$ by 1.03 eV compared to BOD-Ph. The latter state lies 0.98 eV below the bright state $D(\pi_{BOD} \rightarrow \pi^{*}_{BOD})$, implying that it is energetically accessible. However, a reverse trend is observed for $D(\pi_{Ph} \rightarrow \pi^{*}_{BOD})$ states, which are destabilized by 0.20 eV. This trend is consistent with that observed in the corresponding non-reduced compound. Incorporation of an OH substituent leads to an increase of 0.33 eV in the energy of the lowest $D(\pi_{BOD} \rightarrow \pi^{*}_{Ph})$ transition. The two lowest-lying excited states exhibit significant oscillator strengths, particularly in the case of BOD-PhNO_2 (f = 0.269 and 0.244) indicating that both the first and second electronic transitions are allowed and likely to contribute to the absorption spectrum.

Table 5.5 Excited state properties of reduced BOD-Ph at the D_0 geometry calculated in dichloromethane (PCM equilibrium solvation) with MN15.

States	Weight(%)	VEE(eV)	λ(nm)	f	$<S^2>$
$D(\pi_{BOD} \rightarrow \pi^{*}_{BOD})$	84	2.57	482	0.260	0.81
$D(\pi_{BOD} \rightarrow \pi^{*}_{Ph})$	95	2.77	447	0.072	0.81
$D(\pi_{BOD} \rightarrow \pi^{*}_{Ph})$	90	2.92	424	0.054	0.80
$D(\pi_{BOD} \rightarrow \sigma_{I}^{*})$	87	2.96	419	0.004	0.94
$D(\pi_{BOD} \rightarrow \sigma_{I}^{*})$	87	3.08	403	0.001	0.99
$D(\pi_{BOD} \rightarrow \pi^{*}_{BOD})$	88	3.47	357	0.002	0.85
$D(\pi_{BOD} \rightarrow \pi^{*}_{BOD})$	75	3.69	336	0.004	0.88
$D(\pi_{BOD} \rightarrow \pi^{*}_{BOD})$	52	3.82	324	0.019	1.05
$D(\pi_{BOD} \rightarrow \pi^{*}_{BOD})$	85	3.94	314	0.558	0.92
$D(\pi_{BOD} \rightarrow \sigma_{I}^{*})$	58	4.07	304	0.001	2.37
$D(\pi_{BOD} \rightarrow \pi^{*}_{Ph})$	47	4.69	264	0.007	1.80
$D(\pi_{BOD} \rightarrow \pi^{*}_{Ph})$	41	4.96	250	0.004	1.96

Table 5.6 Excited state properties of reduced BOD-PhOH at the D_0 geometry calculated in dichloromethane (PCM equilibrium solvation) with MN15.

States	Weight(%)	VEE(eV)	λ(nm)	f	$<S^2>$
$D(\pi_{BOD} \rightarrow \pi^{*}_{BOD})$	79	2.58	479	0.229	0.81
$D(\pi_{BOD} \rightarrow \pi^{*}_{Ph})$	87	2.82	439	0.084	0.81
$D(\pi_{BOD} \rightarrow \sigma_{I}^{*})$	90	2.93	423	0.001	0.95
$D(\pi_{BOD} \rightarrow \sigma_{I}^{*})$	86	3.03	409	0.013	0.95
$D(\pi_{BOD} \rightarrow \pi^{*}_{Ph})$	89	3.11	399	0.046	0.89
$D(\pi_{BOD} \rightarrow \pi^{*}_{BOD})$	88	3.50	354	0.001	0.85
$D(\pi_{BOD} \rightarrow \pi^{*}_{BOD})$	56	3.72	334	0.000	0.89
$D(\pi_{BOD} \rightarrow \pi^{*}_{BOD})$	43	3.76	329	0.065	1.04
$D(\pi_{Ph} \rightarrow \pi^{*}_{Ph})$	84	3.93	315	0.578	0.91
$D(\pi_{BOD} \rightarrow \pi^{*}_{BOD})$	48	3.99	310	0.070	1.61
$D(\pi_{Ph} \rightarrow \pi_{BOD}^{*})$	24	4.34	285	0.08	2.19
$D(\pi_{BOD} \rightarrow \pi^{*}_{Ph})$	69	4.75	261	0.014	2.08

Table 5.7 Excited state properties of reduced BOD-PhNO$_2$ at the D$_0$ geometry calculated in dichloromethane (PCM equilibrium solvation) with MN15.

States	Weight(%)	VEE(eV)	λ(nm)	f	$<S^2>$
D($\pi_{BOD} \rightarrow \pi^*_{Ph}$)	95	1.33	934	0.269	0.79
D($\pi_{BOD} \rightarrow \pi^*_{BOD}$)	70	2.31	536	0.244	0.79
D($\pi_{BOD} \rightarrow \pi^*_{Ph}$)	96	2.65	467	0.012	0.80
D($\pi_{BOD} \rightarrow \sigma_I^*$)	50	3.17	391	0.007	0.95
D($\pi_{BOD} \rightarrow \sigma_I^*$)	68	3.17	390	0.000	0.95
D($\pi_{BOD} \rightarrow \sigma_I^*$)	83	3.28	378	0.000	1.04
D($\pi_{BOD} \rightarrow \pi^*_{Ph}$)	59	3.33	373	0.011	2.55
D($\pi_{BOD} \rightarrow \pi^*_{Ph}$) D($\pi_{BOD} \rightarrow \pi^*_{BOD}$)	50 45	3.40	365	0.000	0.91
D($\pi_{Ph} \rightarrow \pi^*_{Ph}$)	46	3.42	362	0.024	2.26
D($\pi_{Ph} \rightarrow \pi^*_{Ph}$)	48	3.46	358	0.204	1.58

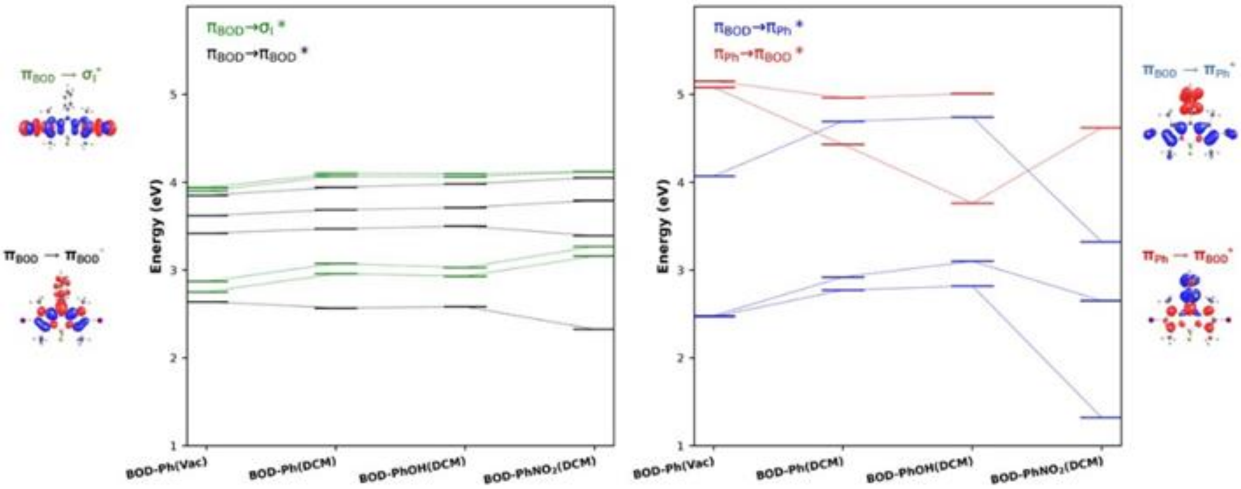

Figure 5.2: Doublet states vertical energy diagrams of BOD-Ph, BOD-PhOH and BOD-PhNO$_2$ in vacuum and DCM calculated at the D$_0$ optimized geometries with TDA-TDDFT (MN15). Examples of charge density difference (CDD) are shown for different types of transitions; positive (electron) and negative (hole) values are indicated in red and blue colors, respectively.

5.5 Excited states geometry optimization of the reduced compounds

The lowest-lying excited-state geometries for the three BODIPY dyes were optimized using the TDA-TDDFT approach in DCM employing the MN15 XC functional. Thereafter, adiabatic energies were calculated, using the equilibrium solvation model within the PCM framework at each corresponding geometry. Additional TDA-TDDFT calculations employing the SOS-ωPBEPP86 functional were done to compare the performance of the two XC functionals. **Figure 5.3** reports the prominent lowest electronic states possibly involved in the reduced catalytic activity. All the calculated vibrational frequencies are positive, confirming that the obtained geometries are minima of the PES. For the reduced BOD-PhNO$_2$, the lowest

$D(\pi_{BOD} \rightarrow \pi^*_{Ph})$ fails to converge to a true minimum of the PES; whereas the second $D(\pi_{BOD} \rightarrow \pi^*_{Ph})$ state geometry converged successfully. Therefore, for BOD-PhNO$_2$ the energies of both states (blue color) were included in **Figure 5.3** only at the optimized geometry.

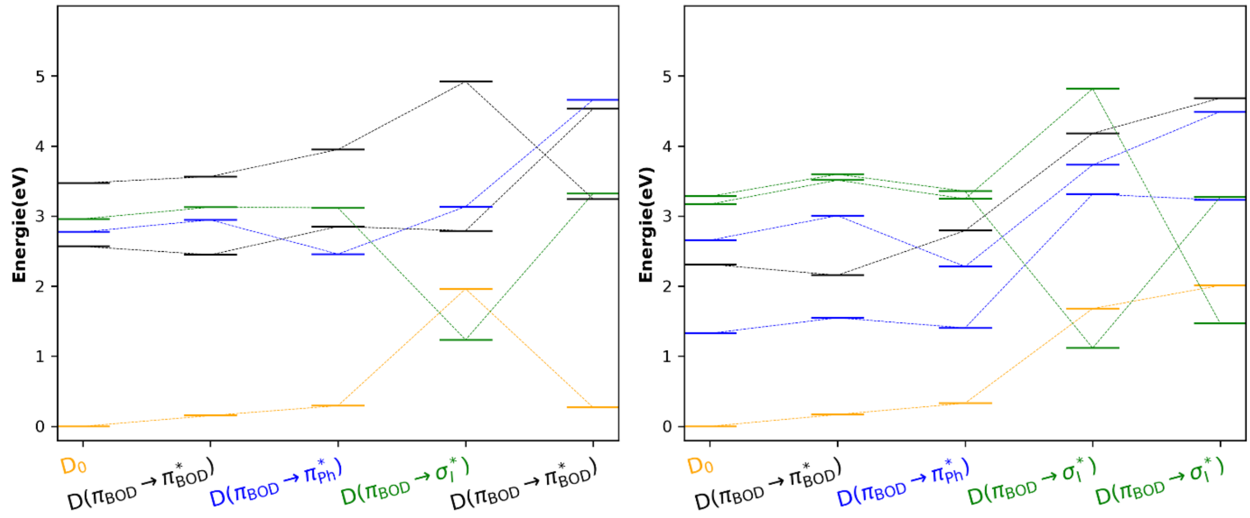

BOD-Ph(TDA-TDDFT)_MN15 **BOD-PhNO$_2$(TDA-TDDFT)_MN15**

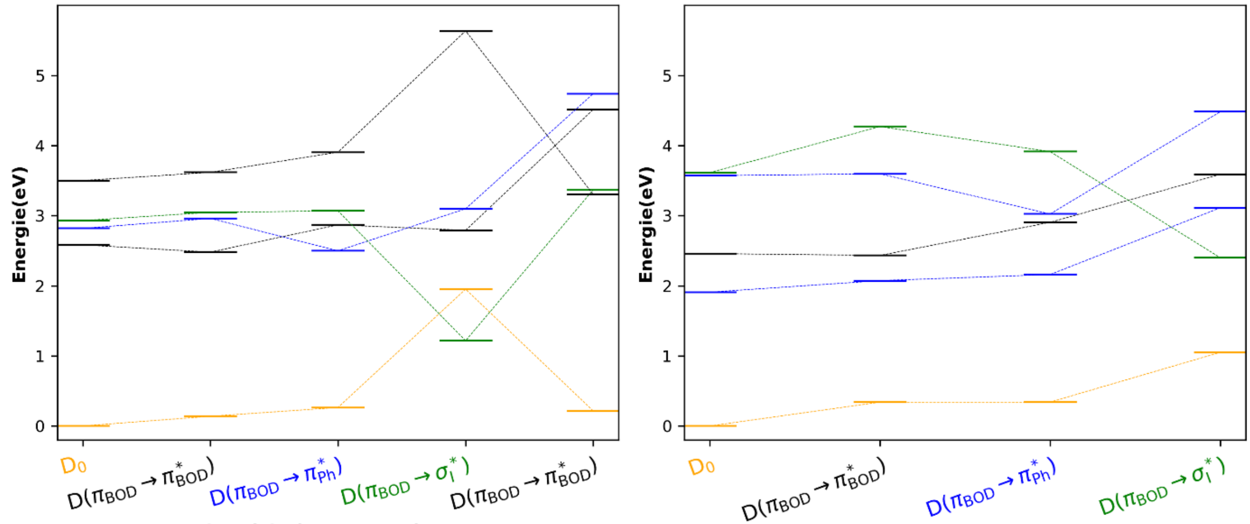

BOD-PhOH(TDA-TDDFT)_MN15 **BOD-PhNO$_2$(TDA-TDDFT)_SOS-ωPBEPP86**

Figure 5.3: Energy diagrams for selected doublet states of BOD-Ph, BOD-PhOH and BOD-PhNO$_2$. The calculations were performed at different geometries in DCM with TDA-TDDFT (MN15 and SOS-ωPBEPP86).

Table 5.8 Phenyl-(BODIPY core) torsion angle and C-I bond length for the three compounds at the optimized geometries.

Compounds	States	Angles(°)	C-I bond lengths (Å)
BOD-Ph	D_0	111.6	2.08
	$D(\pi_{BOD} \rightarrow \pi_{BOD}^*)$	122.1	
	$D(\pi_{BOD} \rightarrow \pi^*_{Ph})$	92.7	
	$D(\pi_{BOD} \rightarrow \sigma_I^*)$	100.8	2.82
BOD-PhOH	D_0	110.4	2.08
	$D(\pi_{BOD} \rightarrow \pi_{BOD}^*)$	114.8	
	$D(\pi_{BOD} \rightarrow \pi^*_{Ph})$	110.3	
	$D(\pi_{BOD} \rightarrow \sigma_I^*)$	100.8	2.82
BOD-PhNO$_2$	D_0	123.2	2.08
	$D(\pi_{BOD} \rightarrow \pi_{BOD}^*)$	134.9	
	$D(\pi_{BOD} \rightarrow \pi^*_{Ph})$	138.9	
	$D(\pi_{BOD} \rightarrow \sigma_I^*)$	104.8	2.82

Upon photoexcitation of the reduced BOD-Ph system, the locally excited doublet state $D(\pi_{BOD} \rightarrow \pi_{BOD}^*)$ is initially populated at the FC region corresponding to the ground-state (D_0) geometry, with an oscillator strength f of 0.26. This excited state subsequently relaxes to the same electronic configuration at its optimized geometry, exhibiting a torsional change of 10.5° and an energy stabilization of 0.12 eV. In contrast, the $D(\pi_{BOD} \rightarrow \pi^*_{Ph})$ state undergoes a higher decrease of 0.32 eV during relaxation and lies 0.01 eV above the optimized $D(\pi_{BOD} \rightarrow \pi_{BOD}^*)$ energy. This small energy gap suggests competitive population dynamics between the bright state $D(\pi_{BOD} \rightarrow \pi_{BOD}^*)$ and CT state $D(\pi_{BOD} \rightarrow \pi^*_{Ph})$. Moreover, the vibrational frequencies corresponding to phenyl rotation in these two optimized geometries are 38.3 and 41.2 cm^{-1}. These values lie below the thermal energy at room temperature ($kT = 209$ cm^{-1}), indicating that the rotational modes are readily populated under ambient conditions. However, previous studies of the non-reduced BOD-Ph compound indicate that the MN15 functional underestimates CT state energies. Consequently, the adiabatic energy of the CT state $D(\pi_{BOD} \rightarrow \pi^*_{Ph})$ is likely energetically inaccessible.

Dissociative states associated with C–I bond cleavage are predicted to be energetically inaccessible after photoexcitation and yield anomalously low adiabatic excitation energies. This behaviour is most plausibly an artefact of the TDA-TDDFT/MN15 approach, which does not capture static-correlation effects with sufficient accuracy at the predicted C-I bond length of 2.82 Å (**Table 5.8**).

BOD–PhOH exhibits the same energetic trend as BOD-Ph, with only slight deviations in the adiabatic excitation energies: 0.004 eV for $D(\pi_{BOD} \rightarrow \pi_{BOD}^*)$ and 0.005 eV for $D(\pi_{BOD} \rightarrow \pi^*_{Ph})$, respectively. The incorporation of an EWG (NO_2) at the para-position in BOD-PhNO_2 stabilizes the adiabatic energy of the D(π_{BOD} → π^*_{Ph}) transition by 0.79 eV relative to BOD-Ph, as evaluated at the D(π_{BOD}→π_{BOD}*) optimized geometry for the two compounds. Consequently, this lowest-energy D(π_{BOD} → π^*_{Ph}) state, at the optimized geometry D(π_{BOD} → π^*_{Ph}), becomes easily populated during relaxation, exhibiting a 0.91 eV energy gap relative to the D(π_{BOD} → π_{BOD}*) state, calculated at the ground state D_0 geometry. A difference of 15.7° in the torsion angle is observed between these two geometries. As with the previous compounds, the dissociative state remains inaccessible and exhibits an anomaly at its optimized geometry, which renders the prediction of dissociative pathways difficult.

Even though the total energies calculated with SOS-ωPBEPP86 are higher than those obtained with MN15 possibly owing to spin contamination, they globally retain the same energetic trend, confirming that the CT state D(π_{BOD} → π^*_{Ph}) is energetically easily accessible. Indeed, the adiabatic energies of the lowest states D(π_{BOD} → π_{BOD}*) and D(π_{BOD} → π^*_{Ph}) are increased by 0.3 and 0.52 eV at the D(π_{BOD} → π_{BOD}*) optimized geometry, relative to the MN15 results. However, at the optimized D(π_{BOD} → π^*_{Ph}) geometry, the lowest D(π_{BOD} → π^*_{Ph}) state lies 0.74 eV below the D(π_{BOD} → π_{BOD}*) state, yielding an energy gap of 0.31 eV compared to the D(π_{BOD} → π_{BOD}*) state at D_0 geometry, which is 0.6 eV smaller than the value calculated with MN15. Moreover, the adiabatic energy of the dissociative D(π_{BOD} → σ_I*) state is increased by 0.94 eV compared to the adiabatic energy calculated with MN15. This places this state significantly above the D_0 energy (4.27 eV) and near the adiabatic energy of the D(π_{BOD} → π_{BOD}*) state (0.04 eV). The stronger dependence of the D(π_{BOD} → σ_I*) state energy on the employed functional indicates that more advanced correlated methods should be used to characterize the energetic position of such states.

5.6 Conclusion

The assessment of the vertical energies of doublet excited states in vacuum using the meta-hybrid functional MN15 and double-hybrid functionals (SOS-PBE-QIDH, SOS-ωPBEPP86) shows that the MN15 functional provides a more balanced description, achieving a MAD of about 0.1 eV compared to RASPT2 calculations. However, all functionals — including the long-range corrected SOS-ωPBEPP86 — struggle to accurately describe doublet CT states. This limitation is likely due to the high spin contamination, where the doublet states are strongly mixed with triplet states.

CT states are particularly sensitive to structural rearrangements arising from equilibrated solvent–solute interactions between BOD–Ph and DCM. These interactions lead to a destabilization of the vertical energy of the D($\pi_{BOD} \rightarrow \pi^{*}_{Ph}$) state by 0.46 eV and a decrease of up to 0.41 eV for the D($\pi_{Ph} \rightarrow \pi^{*}_{BOD}$) state. Furthermore, the attachment of EWG (NO_2) and EDG (OH) stabilizes the D($\pi_{BOD} \rightarrow \pi^{*}_{Ph}$) state by 1.45 eV for BOD-$PhNO_2$ and the D($\pi_{Ph} \rightarrow \pi^{*}_{BOD}$) state by 0.67 eV for BOD-PhOH.

The relaxation pathways indicate that, upon photoexcitation in D($\pi_{BOD} \rightarrow \pi_{BOD}{*}$), the reduced BOD–Ph and BOD–PhOH compounds are more likely to release an electron to the catalytic center from the local excited state D($\pi_{BOD} \rightarrow \pi_{BOD}{*}$), whereas CT states are scarcely populated. In contrast, in the reduced BOD–$PhNO_2$ compound, the lowest CT state is energetically accessible, possibly opening an efficient non-radiative deactivation channel, which would explain the low turnover number for hydrogen generation obtained with this sensitizer [31].

These results are condition-dependent, as the catalytic turnover can vary significantly with experimental parameters. Factors such as the type of solvent, the nature of the substituent, and whether the photosensitizer and catalytic center are connected intra- or intermolecularly can all play a decisive role. From the above analysis of the electron transfer mechanism for the three reduced compounds, we may conclude that the results are in agreement with Hypothesis 2, whereby electron transfer to the catalytic center most likely occurs from the reduced bright state via intermolecular interactions, which initiates the water reduction process. In contrast, the tendency to populate CT states coincides with a decrease in the photocatalytic activity, ultimately leading to deactivation of the process, which contradicts Hypothesis 1. This is most evident in reduced BOD-$PhNO_2$, in which stabilization of the adiabatic energies of the short-lived CT states coincides with a steep decrease in catalytic activity. Indeed, the competition between the reduced bright state and the dark CT states decisively determines the fate of the catalytic activity.

Chapter 6: Photophysical Properties for BOD-Ph

6.1 Introduction to computational vibronic-coupling methods

The investigation of photophysical properties plays a crucial role in optimizing technological applications. Various pathways can lead to a diverse spectrum of applications, depending on the excited-state manifold and the mechanisms involved. According to Kasha's law, upon photoexcitation, the population of the lowest vibrational state of an excited electronic state is highly probable, followed by emission from the S_1 to S_0 states. However, rapid vibrational coupling between different electronic states, occurring on a timescale between 10^{-14} and 10^{-11} seconds, can lead to internal conversion. Meanwhile, strong spin-orbit coupling or a small energy gap between singlet and triplet states can facilitate transitions between electronic states with different spin multiplicities, a process known as intersystem crossing. Several experimental methods, such as magnetic circular dichroism and electron spin resonance, are employed to probe these transitions. However, the high costs and potential errors associated with these techniques necessitate an interplay between experimental and theoretical approaches. Recently, several computational programs have been developed to calculate photophysical rates, relying on the Franck-Condon principle and Fermi's golden rule. Additionally, an electronic state's PES is often approximated as a harmonic oscillator using a second-order Taylor expansion around the relevant geometric coordinates. In this approximation, the ground and excited states are connected through a rotational matrix (Duschinsky matrix) and a displacement vector. The assessment of these quantities depends on the model employed to evaluate the harmonic PES and the coordinate chosen to calculate the normal modes. The discrepancy between the simulated and experimental rates may be attributed to additional decay channels, such as conical intersections or dark trap states, as well as to other effects including Duschinsky rotation, Herzberg–Teller coupling, anharmonicity, and electron correlation effects.

Different models have been proposed to describe the frequencies (Hessian) and geometries for such transitions. If one considers a transition occurring from state S_n to state S_m, the following harmonic models can be used:

- Adiabatic Hessian (AH): The extrapolation of the quadratic PES is performed around the optimized structures of the initial S_n and final S_m states. The geometries, frequencies and normal modes of both states are employed.
- Vertical Hessian (VH): The Hessians and gradients of the states (S_n and S_m) are calculated at the geometry of the initial state S_n.
- Adiabatic Shift (AS): S_n and S_m are assumed to have identical Hessians (vibrational modes and frequencies), and the PES minimum is simply shifted.

In order to evaluate vibrational wave function overlaps, both time-independent (TI) and time-dependent (TD) approaches are used. The former treats the overlap as a discrete summation over vibrational states' quantum numbers, with the option to include only those contributing most to the dominant transition, while the latter uses continuous vibrational integration solved through a Fourier transformation.

A major concern regarding the applicability of these vibronic models is that their reliability depends on the specific structure being investigated. Indeed, the real PESs of the ground and excited states must be accurately represented by harmonic approximations and should exhibit similar geometries within the Franck–Condon approximation. Otherwise, the discrepancy between the vertical and adiabatic models may become too large, especially when the system undergoes a large torsional distortion (**Figure 6.1**).

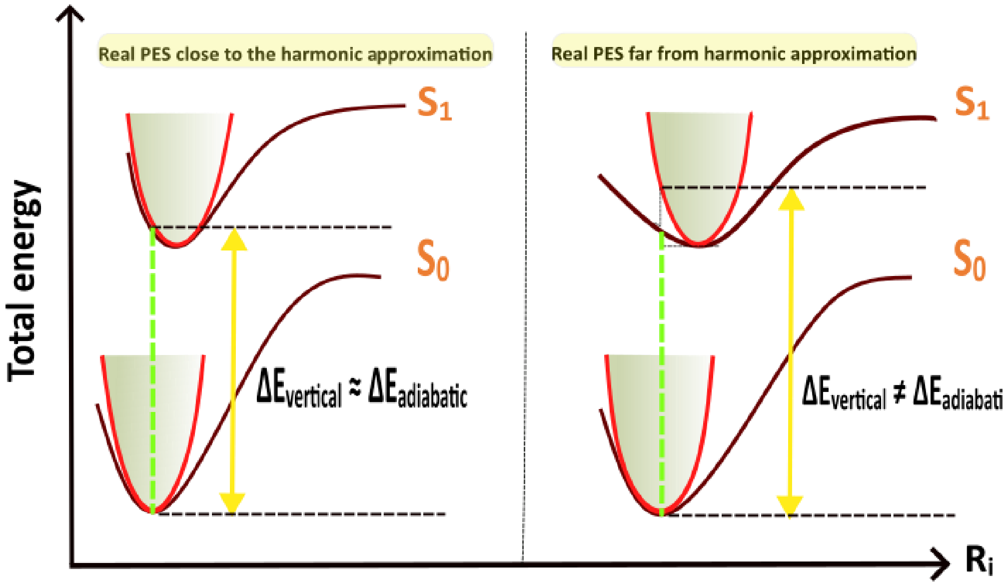

Figure 6.1: Illustration of a system well described by the harmonic approximation (left) and one showing significant anharmonicity (right).

The following section presents a literature review focusing on the applicability of vibronic models, particularly for rigid structures.

Santoro and his colleagues determined the photophysical properties of constrained and flexible compounds to assess the reliability of vibronic models [176]. The calculation of one-photon emission and resonance Raman showed good agreement with experimental data for rigid compounds. However, the plot of the k_{IC} as a function of the energy gap exhibited a dependency on broadening values, leading to unreliable k_{IC} rates in some cases. For flexible compounds, polyphenyl molecules, a scan of the relaxed PES along intra-ring torsion revealed significant configuration changes during transitions, with a torsion angle of around 40 degrees. This finding indicates that the harmonic oscillator approximation may not be suitable for flexible compounds.

Javier Cerezo examined the impact of Duschinsky rotation on the UV-Vis spectrum of β-carotene conformers [177]. The vibrational spectrum computed using the AH approach in Cartesian coordinates overestimated the experimental spectrum width due to the contribution of low-frequency torsional modes and high-frequency bond-stretching modes. Cartesian coordinates cannot adequately describe significant structural displacements between the ground and excited states. This anomaly traces back to a non-orthogonal Duschinsky matrix caused by the mixing of vibrational modes. In contrast, internal coordinates successfully described the curvilinear displacements.

Shuai et al. [178] also studied BODIPY systems and provided an overview of possible deactivation channels occurring between S_0 and S_1 states for these compounds, including IC. They divided the PES scan into two regions: the vertical transition across the Franck-Condon region (harmonic region) and the remaining PES (anharmonic region). The anharmonic channel, which is only accessible in low-efficiency fluorescence BODIPY dyes, involves an accessible energetic barrier.

Francisco José Avila Ferrer et al. [179] conducted a quantitative analysis to assess the performance of the AH, AS, and VH models. They compared quantities (frequency shifts, displacements, the Duschinsky matrix, and Franck-Condon factors between the vibrational states of the initial and final electronic states) involved in transitions between ππ* and nπ* states in various compounds (anthracene, coumarin, porphyrin and pyrazine). For semirigid compounds, AH and VH models yielded similar results, as the influence of imaginary frequencies on the PES is typically minor. However, the AS and VG models overestimated band spacing because these models do not account for differences in the excited-state Hessians.

Research by Daniel Escudero et al. has applied vibrational coupling methodologies to analyze diverse systems and photophysical properties. Initial investigations focused on phosphorescence in iridium complexes, where Huang-Rhys factors were computed to assess vibrational mode influence on de-excitation pathways [180], and later evaluating electron-vibration coupling as a key mechanism for anti-Kasha emission (emission from higher excited states) in organic molecules [181]. The study highlights applications to rigid π-conjugated systems, which are particularly suitable for such models, and reports qualitative estimations of photoluminescence quantum yields for the selected organic structures.

The quantitative study presented in this chapter aims to test the validity of the vibronic models (AH and VH) in determining the photophysical rates of BODIPY dyes. The methodology is applied to BOD-Ph to investigate various mechanisms involving the S_0, S_1, and triplet states, for which both radiative and non-radiative experimental data are available. In this context, the experimental absorption and emission spectra are reproduced using the mentioned models, and the discrepancies between the experimental and theoretical spectra are analyzed. Furthermore, the influence of different parameters (broadening width, energy gap ΔE, SOC, and normal modes coordinates) on the photophysical rates is examined, and the vibrational modes and Huang–Rhys factors contributing to the non-radiative pathways are identified. Throughout this study, unless otherwise specified, the spectra and rates were computed using the TD approach.

6.2 Emission and absorption spectra: theoretical (AH, VH) vs. experimental data

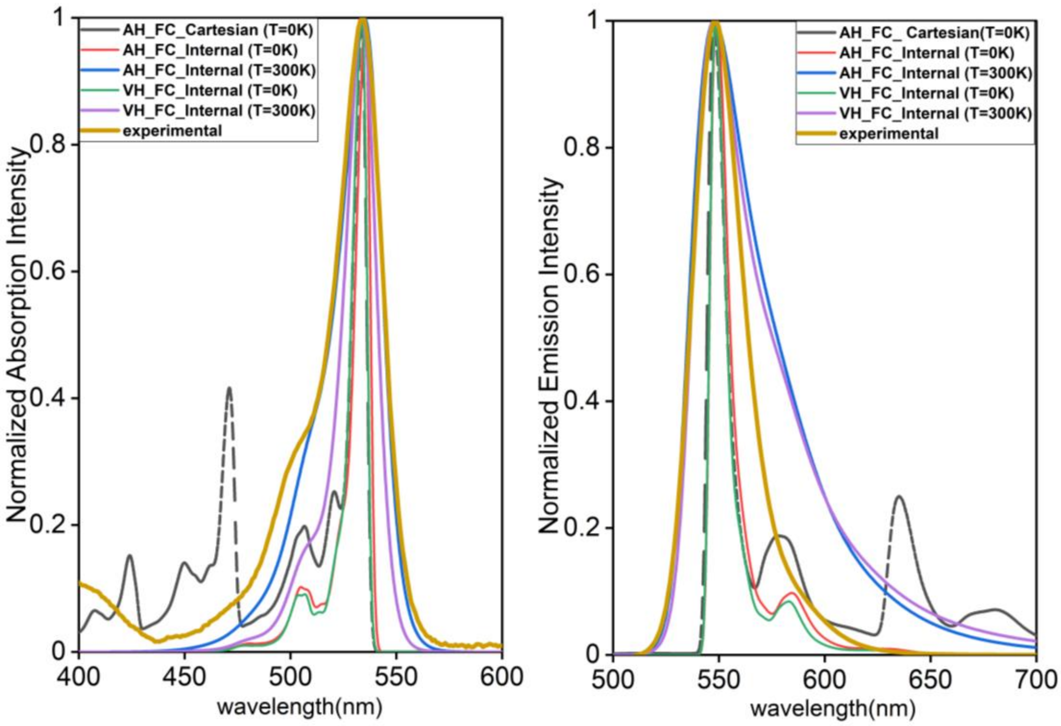

Figure 6.2: Comparison of experimental and computed absorption and emission spectra for BOD-Ph in dichloromethane (DCM, ε = 8.93). The calculations were performed at 0 K and 300 K. Spectral lineshapes were broadened using a Gaussian function with a half-width at half-maximum (HWHM) of 0.01 eV. For better visualization, the calculated spectra were shifted along the wavelength axis (between -0.26 and -0.31 eV) in order to align with the experimental maxima. The calculated and experimental [31] intensities were normalized.

Figure 6.2 shows the normalized absorption and emission spectra calculated using the XC functional MN15, the basis set def2-SVP, and the PCM solvation method, compared with the experimental spectra measured in DCM. Vibrational modes were computed using both Cartesian and internal coordinates, accounting for normal mode mixing between the S_0 and S_1 states, as well as frequency shifts. Within the VH approach for emission, two negative frequencies ($–45\ cm^{-1}$ and $–41\ cm^{-1}$) were obtained for the S_0 state when computing the frequencies at the S_1 geometry. These frequencies were converted to their absolute values in the calculation of the emission spectrum.

The absorption spectrum computed using Cartesian coordinates exhibits overall agreement with the experimental spectrum for wavelengths above 475 nm. However, below this wavelength, unphysical bands appear at anomalous positions. Previous studies [177] attribute this discrepancy to mode mixing between low- and high-frequency modes, indicating that

Cartesian coordinates may inadequately capture torsional displacements. To disentangle this effect, the displacement vector was set to 0, which is denoted as zero displacement vector (ZDV) calculation. As shown in **Figure 6.3**, the presence of unphysical overtone features in the simulated spectra can be attributed to mixing within the Duschinsky matrix when using Cartesian coordinates.

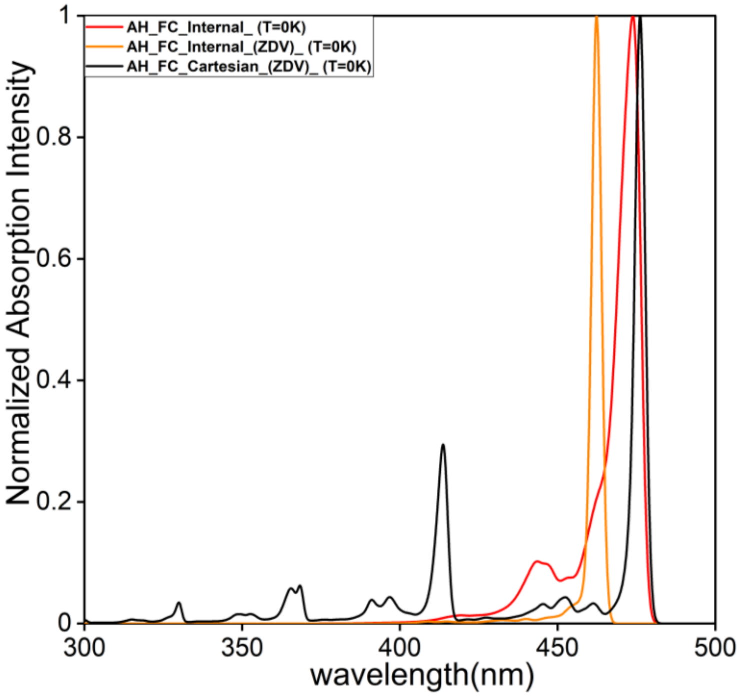

Figure 6.3: Simulated absorption spectrum using Duschinsky matrix evaluated with AH and ZDV.

To single out the vibrational modes responsible for such artifacts, the absorption spectrum was simulated using AH (Cartesian) with the TI approach at 0 K. The evaluation of FC factors indicates that the spectral artifacts predominantly arise from transitions to specific vibrational modes in the S_1 electronic state. These include low-frequency modes 2 (33.8 cm^{-1}), 7 (69.4 cm^{-1}), and 10 (102.6 cm^{-1}), as well as high-frequency modes 109 (3069.9 cm^{-1}) and 110 (3070.3 cm^{-1}). The low-frequency modes primarily correspond to phenyl and methyl torsional motions, while the high-frequency modes are associated with C–H stretching vibrations of the methyl groups (**Figure 6.4**). These results suggest that the artifacts stem from an incorrect coupling between vibrational modes in the S_1 and S_0 states when Cartesian coordinates are used in the simulation. A similar observation is made in the case of the emission spectrum (**Figure 6.2**).

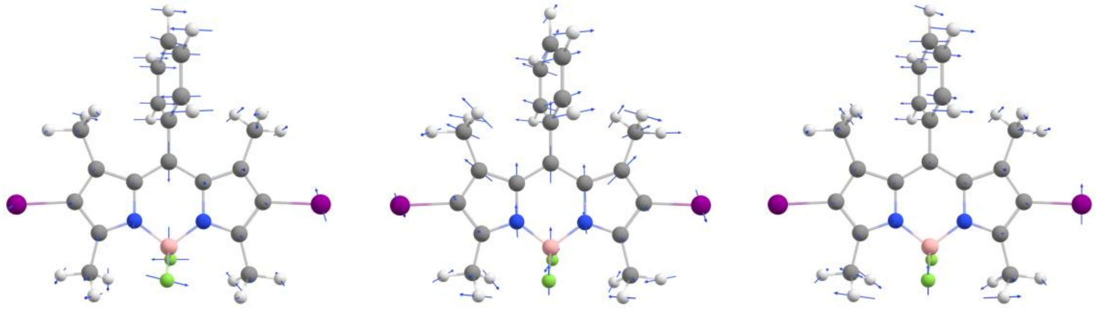

Mode 2: 33.8 cm^{-1} Mode 7: 69.4 cm^{-1} Mode 10: 102.6 cm^{-1}

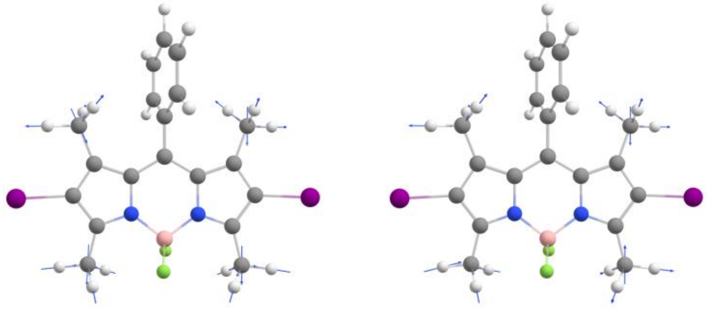

Mode 109: 3069.9 cm^{-1} Mode 110: 3070.3 cm^{-1}

Figure 6.4: S_1 state normal modes of vibration involved in Duschinsky matrix mixture. Blue arrows: Vibrational mode vectors.

In the second step, the normal mode displacements responsible for the pronounced broadening progression are examined (**Figure 6.5**). It is evident that the low-frequency modes 1 (20.7 cm^{-1}), 2 (36.5 cm^{-1}), 7 (71.5 cm^{-1}), 10 (100.4 cm^{-1}), 13 (145.6 cm^{-1}), 19 (215.2 cm^{-1}) contribute to the broadening in both internal and Cartesian coordinate representations. Moreover, higher-frequency modes with noticeable displacements are also contributing, for example the modes 34 (498.8 cm^{-1}), 39 (600.3 cm^{-1}), 59 (1010.8 cm^{-1}) and 79 (1317.7 cm^{-1}).

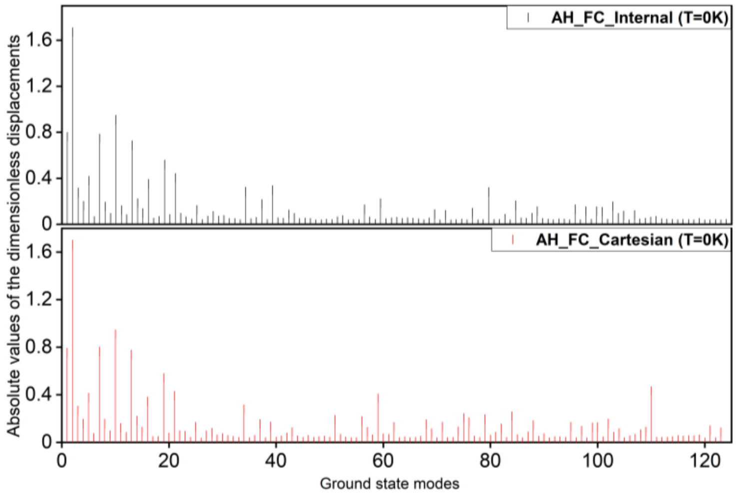

Figure 6.5: Absolute values of the dimensionless displacements, computed as $\delta_i = (2\pi\nu_i^{GS}/\hbar)^{\frac{1}{2}}K_i$ with the AH model.

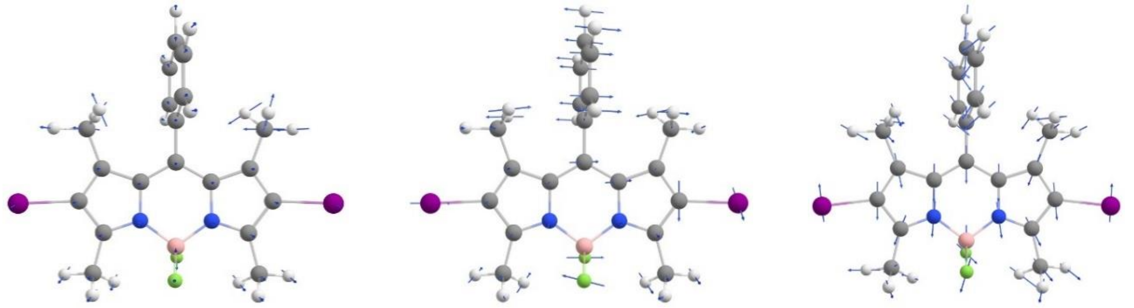

Mode 1: 20.7 cm^{-1} Mode 2: 36.5 cm^{-1} Mode 7: 71.5 cm^{-1}

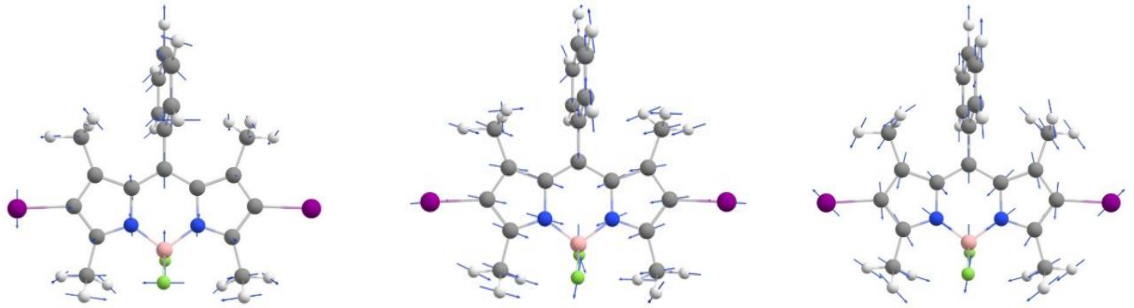

Mode 10: 100.4 cm^{-1} Mode 13: 145.6 cm^{-1} Mode 19: 215.2 cm^{-1}

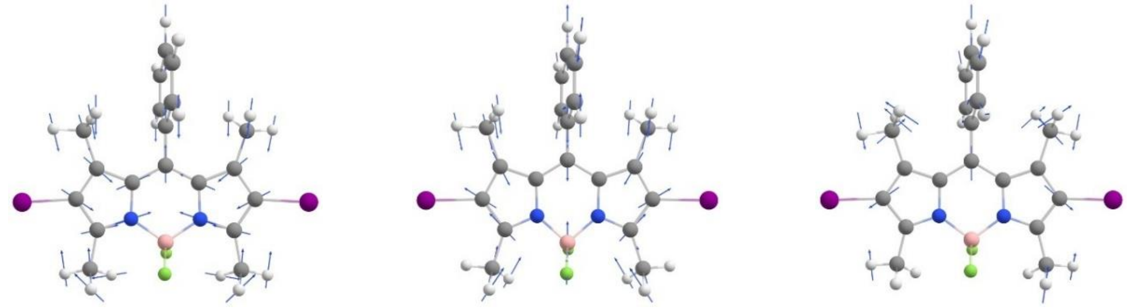

Mode 34: 498.8 cm^{-1} Mode 39: 600.3 cm^{-1} Mode 59: 1010.8 cm^{-1}

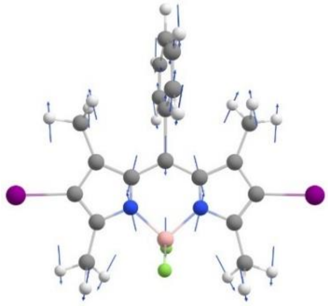

Mode 79: 1317.7 cm^{-1}

Figure 6.6: S_0 state normal modes of vibration involved in the broadening progression. Blue arrows: Vibrational mode vectors.

According to the normal modes 1 (20.7 cm^{-1}), 2 (36.5 cm^{-1}), 7 (71.5 cm^{-1}), and 10 (100.4 cm^{-1}), the broadening progression can be attributed to the torsional motion of the phenyl substituent and the bending of the methyls, while modes 13 (145.6 cm^{-1}) and 19 (215.28 cm^{-1}) can be associated mainly with the contraction and the stretching of the BODIPY core. At higher frequencies (modes 34, 39, 59, and 79), the spectrum is dominated by methyl bending, ring breathing modes, and C–I stretching.

During relaxation between the S_0 and S_1 geometries, the rotation angle of the meso-phenyl ring changed by approximately 8.1°, which additionally indicates that internal coordinates should be used to describe the vibronic progression in such a non-rigid system.

At T = 0 K, both the VH and AH approaches yield nearly identical spectra for both absorption and emission (**Figure 6.2**). At this temperature, transitions occur only from the lowest vibrational level of the initial electronic state toward the vibrational levels of the final state. At 300 K, higher vibrational levels of the initial state become thermally populated. Transitions from these higher levels to the vibrational levels of the final state lead to broader spectra. In absorption, thermal broadening leads to better agreement with the experimental spectra when using the AH model, whereas in emission, the broadening is somewhat overestimated in both the AH and VH models (**Figure 6.2**). However, the underlying cause of this overestimation is not entirely clear and may arise from an inaccurate choice of the HWHM value or from errors in the Franck–Condon factors calculation.

In order to interpret the mismatch between the experimental and modeled emission spectra, the effects of the type of broadening (Gaussian, Voigt), the width of the broadening ($HWHM_G$ of 0.001, 0.01, and 0.1 eV), and the normal modes contributing to the phenyl torsion in the AH model were tested.

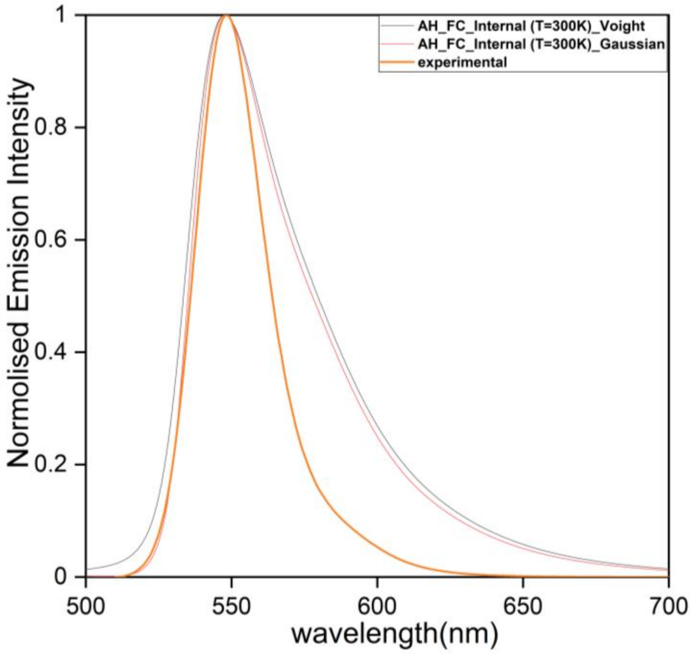

Figure 6.7: Influence of Gaussian and Voigt broadening on the emission spectrum using $HWHM_G$ (Gaussian) and $HWHM_L$ (Lorentzian) values of 0.01 eV.

As shown in **Figure 6.7**, the calculated emission spectrum with the AH model is independent of the type of broadening, both in terms of its shape and width. This already indicates that the radiative rate (k_r) may also be independent of the type of broadening and thus consistent.

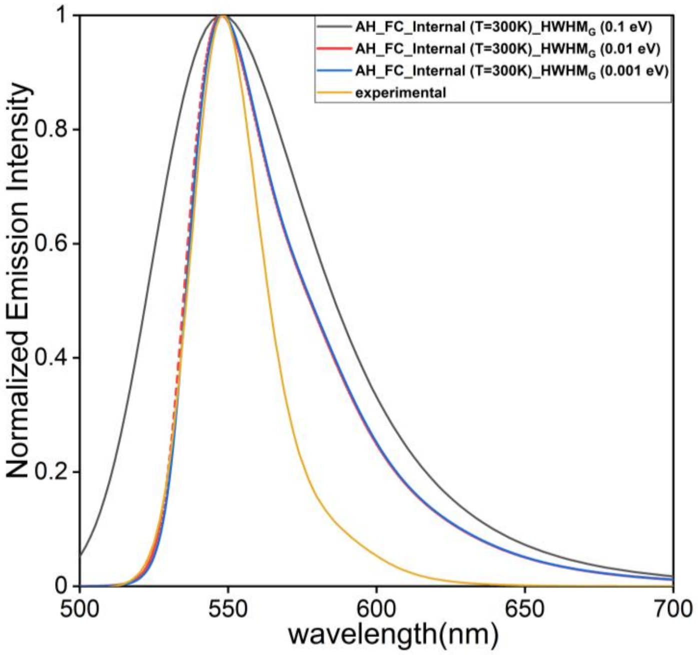

Figure 6.8: Theoretical emission spectrum using a Gaussian broadening and varying $HWHM_G$. Values indicated in the inset.

Figure 6.8 illustrates the impact of the $HWHM_G$ parameter on the broadening of the simulated emission spectrum. For $HWHM_G$ values of 0.001 eV and 0.01 eV, the spectra are nearly identical and remain relatively narrow. However, increasing the $HWHM_G$ to 0.1 eV leads to a significantly broadened spectral shape in larger disagreement with experiment. This simulated broadening may mismatch with the underlying physical broadening mechanism, which fails to replicate the experimental broadening. As a result, a $HWHM_G$ of 0.01 eV is employed in the further simulations.

Moreover, when modes 2 (33.8 cm^{-1}) and 7 (69.4 cm^{-1}), which correspond to low-frequency vibrational motions in the S_1 geometry, are omitted from the Franck–Condon calculations, the previously overestimated broadening becomes significantly narrower, indicating that these modes cannot be treated adequately within the simple harmonic approximation, thus, their removal from the calculation is justified (**Figure 6.9**).

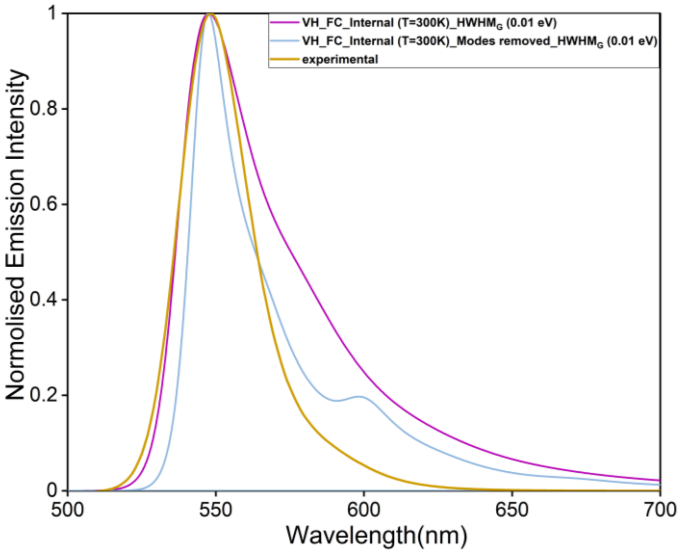

Figure 6.9: The effect of removing the normal modes associated with the phenyl torsion on the emission spectrum.

Going beyond the Franck–Condon approximation, we assess the impact of variations in the transition dipole moment with respect to nuclear coordinates, as illustrated in **Figure 6.10**. The HT approximation introduces only a negligible effect on both the absorption and emission spectra. The vibronic structure remains primarily governed by the large magnitude of the squared transition dipole moment. While the HT approximation leads to slight modifications in peak intensities, its effects become more pronounced only in cases of weak electronic transitions. Therefore, HT contributions were neglected in the following analyses.

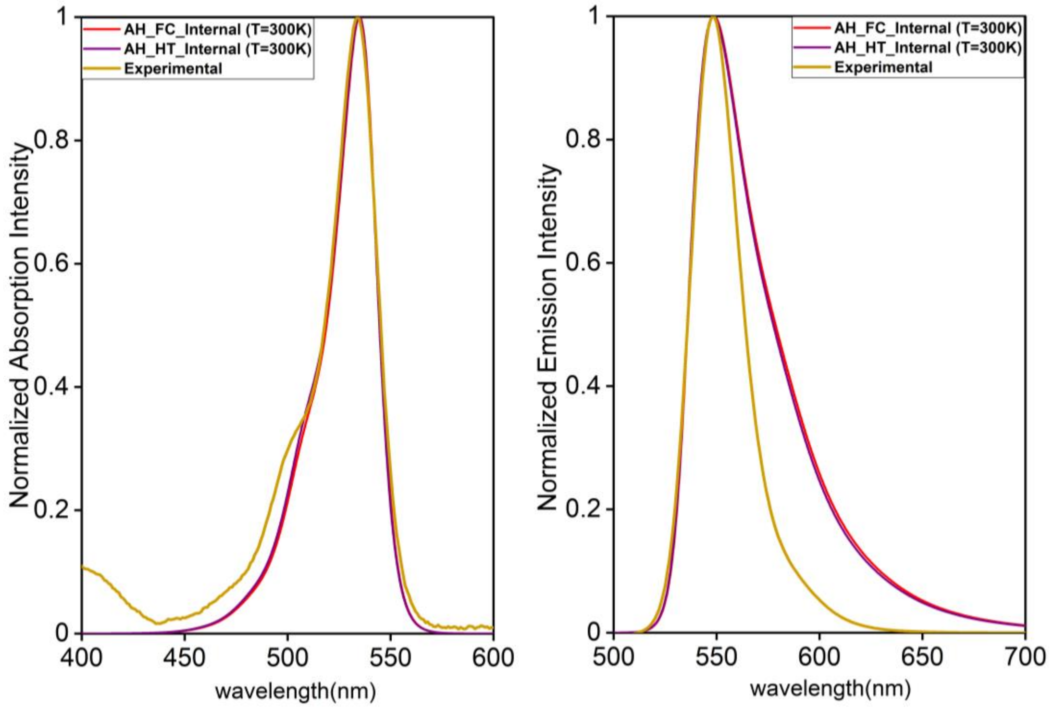

Figure 6.10: Impact of the Herzberg-Teller approximation on absorption and emission spectra.

6.3 Analysis of rate constants using AH and VH models

Table 6.1 presents the variation of the k_r and k_{IC} rates for BOD-Ph as a function of the Voigt broadening. The Lorentzian parameter $HWHM_L$ is varied, while the Gaussian parameter $HWHM_G$ is kept constant at 0.01 eV. Nearly no variation is observed in the radiative rate, except for the largest value of $HWHM_L$. However, the rate of internal conversion is strongly affected by several orders of magnitude when varying $HWHM_L$ over the whole range of values between 10^{-6} and 10^{-1} eV. In general, BODIPY compounds exhibit a relatively long excited-state lifetime (~7.2 ns) [182], which corresponds to a narrow Lorentzian broadening under experimental conditions. Therefore, some of the broadened values used in the model may not fully reflect realistic experimental linewidths.

Table 6.1 Values of k_{IC} and k_r rates obtained using the AH model with a Voigt broadening function, calculations made with a $HWHM_G$ = 0.01 eV.

$HWHM_L$ (eV)	k_{IC} (s^{-1})	k_r (s^{-1})
1E-1	1.08E+10	2.37E+08
1E-2	1.08E+09	2.59E+08
1E-3	1.08E+08	2.62E+08
1E-4	1.12E+07	2.62E+08
1E-5	1.53E+06	2.62E+08
1E-6	5.61E+05	2.62E+08

In **Table 6.2**, we report the variation of the rate constants k_{IC}, k_r, and k_{ISC}, calculated using the AH and VH models, as a function of different spectral broadening functions (Voigt, Lorentzian, and Gaussian). The ISC rate corresponds to the transition between S_1 and the lowest triplet state T_1. The Gaussian lineshape represents inhomogeneous broadening, which arises from factors such as small shifts in excited-state energies due to interactions between the molecule and the surrounding solvent. In contrast, the Lorentzian lineshape corresponds to homogeneous broadening, which is related to the finite lifetime of vibrational states. While the choice of broadening function has a minor effect on the k_r as shown for the emission spectrum, it has a substantial impact on both k_{IC} and k_{ISC}. Specifically, the values of k_{IC} and k_{ISC} computed using Voigt convolution and Lorentzian broadening are approximately two to four orders of magnitude higher than those obtained with Gaussian broadening. Moreover, a subtle difference is observed between the two models (AH and VH) in all cases except for k_{IC} and k_{ISC}, which, when computed using the Gaussian broadening function, exhibit a discrepancy of about an order of magnitude. According to **Table 6.1** and the reference [154], k_{IC} shows inconsistency as a function of $HWHM_L$, especially for higher $HWHM_L$ values. Therefore, the $HWHM_G$ will be used in the following part.

Table 6.2 k_r, k_{IC} and k_{ISC} rates predicted by harmonic models. The broadening functions are a Gaussian with $HWHM_G$ = 0.01 eV, a Lorentzian with $HWHM_L$ = 0.01 eV and a Voigtian with $HWHM_G$ = $HWHM_L$ = 0.01 eV.

Broadening Function	k_r (s^{-1})		k_{IC} (s^{-1})		k_{ISC} (s^{-1})	
	AH	VH	AH	VH	AH	VH
Gaussian	1.39E+08	2.45E+08	4.54E+05	4.42E+06	8.94E+05	2.69E+04
Lorentzian	2.21E+08	2.31E+08	5.82E+09	5.47E+09	7.35E+06	4.84E+06
Voigt	2.59E+08	2.43E+08	1.08E+09	1.10E+09	2.02E+06	8.47E+05

Table 6.3 shows how ΔE between S_1 and S_0 affects the k_r and k_{IC} decay rates, as calculated with the AH harmonic model, using a fixed Gaussian width ($HWHM_G$ = 0.01 eV). The k_r rate decreases as ΔE becomes smaller, in accordance with the Einstein coefficient relation, which predicts that the spontaneous emission rate is proportional to the cube of the transition energy (ΔE^3). The value obtained using the experimental gap (2.29 eV), 1.39 E+08 s^{-1}, agrees well with the experimental rate of 1.30 E+08 s^{-1}. On the other hand, k_{IC} decreases by over two orders of magnitude when calculated using TDA-TDDFT compared to the DLPNO-STEOM-CCSD method due to an increase in ΔE by 0.68 eV. Moreover, the k_{IC} rates obtained with the AH model are around one to three orders of magnitude lower than the experimental rate. This discrepancy may result from inaccuracies in the calculated ΔE or in the NACs, or it may originate from the neglected anharmonic shape of the PES. Adjusting ΔE to the experimental value (2.29 eV) provides a non-radiative rate comprised in-between the TDA-TDDFT and DLPNO-STEOM-CCSD results, which remains about two orders of magnitude below the experimental value.

Table 6.3 Effect of the variation of the adiabatic energy gap (ΔE) on the value of k_r and k_{IC} rates (s^{-1}), calculated with the AH model ($HWHM_G$ = 0.01 eV).

ΔE		Rates	
type	value (eV)	k_r (s^{-1})	k_{IC} (s^{-1})
Theoretical			
TDA-TDDFT	2.68	2.33E+08	4.54E+05
DLPNO-STEOM-CCSD	2.00	9.75E+07	6.00E+07
Experimental	2.29	1.39E+08	7.32E+06
Experimental [43]			
Experimental	2.29	1.30E+08	5.40E+08

To identify the normal modes that contribute most to the internal conversion process, the Huang–Rhys (HR) factors were plotted.

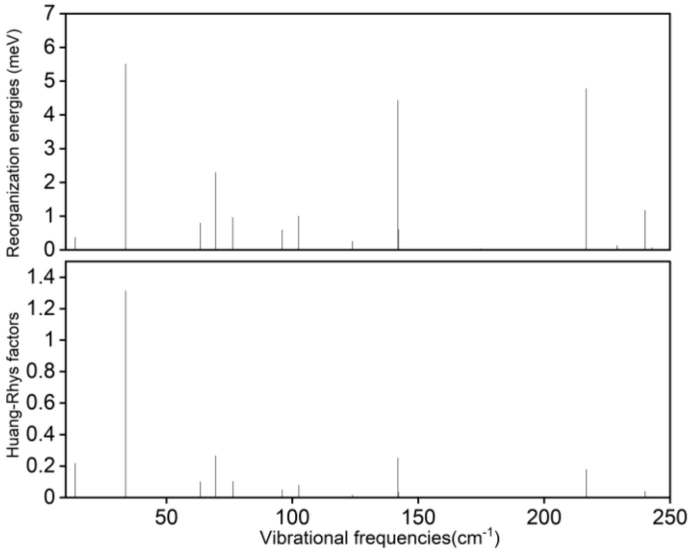

Figure 6.11: HR factors and reorganization energies for all vibrational modes of S_1 (AH).

Figure 6.11 represents the Huang–Rhys factors ($\mathrm{HR_i}$) corresponding to each vibrational mode frequency (v_i) and reorganization energies deduced from the relation $\mathrm{HR_i} * \mathrm{v_i}$.

Low frequencies, especially 33.8 cm^{-1}, participate the most in the k_{IC} rate, associated with the highest reorganization energy (5.46 meV). This mode, since it contributes the most to $k_{IC,}$ needs to be well described by a harmonic model to obtain a correct estimation of the internal conversion rate.

To this extent, the total energies of the S_0 and S_1 states were followed through a relaxed scan. This analysis varied the phenyl-(BODIPY-core) dihedral angle under consideration between 50° and 130°. At each point, this angle was held fixed while the molecule's other structural parameters were optimized. It is apparent from **Figure 6.12** that the harmonic approximation breaks down for this coordinate, which might explain the deviation between the calculated and experimental IC rates. Moreover, following the approach presented in reference [176] the total energies were used to plot the energy histogram of the Boltzmann distribution associated to this coordinate, and an estimation of $HWHM_G$ equal to 0.022 eV was concluded from the convoluted diagram.

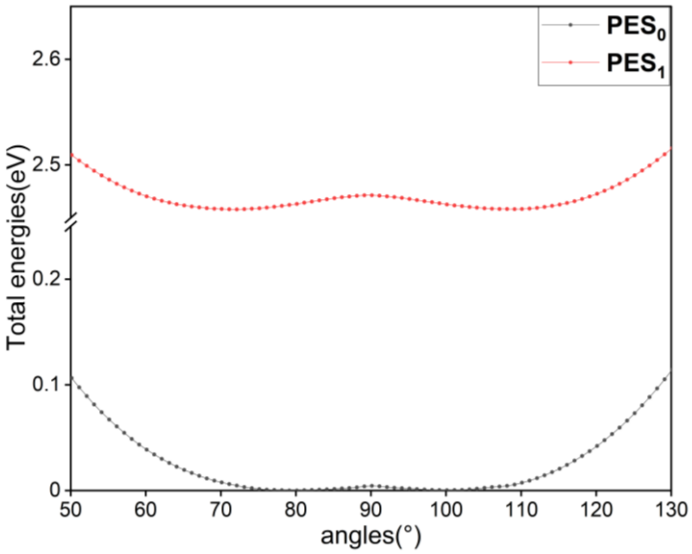

Figure 6.12:Relaxed scans of the S_0 and S_1 states along the phenyl-(BODIPY-core) angle.

Table 6.4 Radiative and IC rates calculated with the VH model ($HWHM_G$ = 0.01 eV).

ΔE		Rates*	
type	value (eV)	k_r (s^{-1})	k_{IC} (s^{-1})
Theoretical			
TDA-TDDFT	2.68	2.45E+08	5.33E+07
Experimental	2.29	1.60E+08	2.61E+08
Experimental [43]			
Experimental	2.29	1.30E+08	5.40E+08

*Imaginary frequencies converted to real positive values.

When the same geometry is enforced between the ground and excited states using the VH model and the imaginary frequencies were converted to real positive values, the k_r rates obtained are consistent with previous results obtained with the AH model (**Tables 6.3** and **6.4**). This is expected, as k_r is an intrinsic property that primarily depends on the square of the transition dipole moment and the energy gap. However, the k_{IC} rates increase by roughly one or two order of magnitude, giving in the case of the VH model a closer agreement with experiment.

Table 6.5 Rates calculated with the VH model using $HWHM_G$ = 0.01 eV (modes 2 and 7 removed).

ΔE		Rates	
type	value (eV)	k_r (s^{-1})	k_{IC} (s^{-1})
Theoretical			
TDA-TDDFT	2.68	2.76E+08	1.26 E+08
Experimental	2.29	1.98E+08 1.98E+08*	4.88E+08 4.92E+08*
Experimental [43]			
Experimental	2.29	1.30E+08	5.40E+08

*calculated using $HWHM_G$ = 0.022 eV.

When modes 2 and 7, which contribute most to the phenyl–(BODIPY core) torsion, are removed, and the $HWHM_G$ is set to 0.022 eV, the calculated internal conversion rate k_{IC} increases and becomes closer in agreement with the experimental value (**Table 6.5**).

Table 6.6 Spin-orbit couplings (SOC) in cm^{-1}, calculated at the S_1, T_1, T_2 and T_3 geometries.

Geometry	$\langle S_1 \vert H_{so} \vert T_1 \rangle$	$\langle S_1 \vert H_{so} \vert T_2 \rangle$	$\langle S_1 \vert H_{so} \vert T_3 \rangle$
S_1	1.25	6.05	15.65
T_1	1.15	11.34	10.40
T_2	7.13	17.92	12
T_3	3.47	10.17	21.58

Table 6.6 shows the dependence of spin–orbit coupling on the chosen geometry, as the angular momentum depends on the spatial configuration of the molecule. In the following, the S_1 -> T_n ISC rates were calculated for two values of the SOC, i.e., using the SOC estimated at the S_1 geometry and the SOC estimated at the T_n geometry (indicated in orange color in **Tables 6.6-6.9**).

Table 6.7 ISC rates of $S_1 \rightarrow T_1$ transition calculated using the AH model with $HWHM_G$ = 0.01 eV.

ΔE		Rates
type	value (eV)	k_{ISC} (s^{-1})
Theoretical		
TDA-TDDFT	1.06	8.94E+05 6.80E+05
DLPNO-STEOM-CCSD	0.64	3.52E+07
Experimental	0.59	4.92E+07
Experimental [43]		
Experimental	0.59	3.50E+09

Table 6.8 ISC rates of $S_1 \rightarrow T_2$ transition calculated using the AH model with $HWHM_G$ = 0.01 eV.

ΔE		Rates
type	value (eV)	k_{ISC} (s^{-1})
Theoretical		
TDA-TDDFT	0.10	7.08E+09 6.21E+10
DLPNO-STEOM-CCSD	0.08	7.09E+09
Experimental	-	-
Experimental [43]		
Experimental	0.59	3.50E+09

Table 6.9 ISC rates of $S_1 \rightarrow T_3$ transition calculated using the AH model with $HWHM_G$ = 0.01 eV.

ΔE		Rates
type	value (eV)	$k_{ISC}(s^{-1})$
Theoretical		
TDA-TDDFT	-0.13	1.35E+07 2.56E+07
DLPNO-STEOM-CCSD	-0.37	1.23E+02
Experimental	-	-
Experimental [43]		
Experimental	0.59	3.50E+09

The populations of T_1, T_2, and T_3 states generated by ISC are reported in **Tables 6.7**-**6.9**. The effect of the quantum chemistry method (TDA-TDDFT and DLPNO-STEOM-CCSD) on the calculated ΔE for the $S_1 \rightarrow T_1$ and $S_1 \rightarrow T_3$ transitions leads to k_{ISC} values that differ by factors of 10^2 and 10^5, respectively. In contrast, k_{ISC} for the $S_1 \rightarrow T_2$ transition remains nearly constant because the energy difference between the two methods is only 0.02 eV. Moreover, k_{ISC} depends on the square of the SOC matrix. This dependence is particularly significant for the $S_1 \rightarrow T_2$ SOC (**Table 6.6**). It leads to about a tenfold increase in k_{ISC} due to geometry-related changes in SOC when transitioning from the S_1 geometry towards the T_2 geometry (**Table 6.8**).

T_1 lies 1.06 eV lower in energy than S_1, while T_3 is 0.13 eV higher at the TDA-TDDFT level of theory. As a result, these triplet states are less likely to be populated through ISC, which may explain the large discrepancy from the experimental ISC rate. Moreover, the $S_1 \rightarrow T_1$ ISC rates obtained with the DLPNO-STEOM-CCSD energy gap or using the S_1-T_1 experimental gap (0.59 eV) remain two orders of magnitude below the experimental ISC rate (**Table 6.7**). In contrast, k_{ISC} calculated between the S_1 and T_2 states in S_1 geometry shows the closest agreement with the experimental value, differing by less than one order of magnitude (**Table 6.8**). This indicates that ISC in BOD-Ph occurs predominantly through population of the T_2 state.

6.4 Conclusion

In this chapter, vibronic models were applied to BOD-Ph, and the following conclusions were drawn:

1. The use of internal coordinates is essential for computing photophysical rates, as it avoids the artificial mode-mixing behavior that appears when Cartesian coordinates are employed.

2. The computed absorption spectrum reproduces the same profile of the experimental data, while the emission spectrum witnesses a spectral overbroadening that may be mainly attributed to methyl bending and phenyl rotation.
3. No noticeable variation in k_r is observed upon varying either the harmonic model (AH/VH) or the line-shape broadening function (Gaussian/Voigt). In contrast, the k_{IC} is strongly affected, yielding the most reasonable results when vibrational modes associated with phenyl torsion are excluded.
4. Theoretical results concerning intersystem crossing show that k_{ISC} proceeds from the S_1 state to the higher-lying triplet level T_2, rather than directly to the lowest triplet state T_1, which had been the conventional assumption.

Chapter 7: TDDFT Investigation of Down-Conversion Materials for Semitransparent Perovskite Solar Cells

7.1 Introduction

Solar cells based on perovskite photoabsorber layers have emerged as a promising third-generation photovoltaic technology due to their outstanding optoelectronic properties, achieving a power conversion efficiency of 33.89% in perovskite/silicon tandem solar cells [183]. In contrast to Si and GaAs solar cells, which require complex architectures, perovskite devices feature a relatively simple structure consisting of two main functional layers: the electron transport layer and the hole transport layer, which sandwich the perovskite absorber layer where electron-hole pair generation occurs. However, the increasing research interest in perovskite solar cells has not been limited to their advantages; it has also addressed the various factors that may disrupt their long-term stability. While environmental challenges such as moisture and oxygen exposure may be mitigated by encapsulation, intrinsic factors such as parasitic absorption of UV and IR light, which leads to optical and thermal losses, can ultimately degrade the performance of the solar cell. Leveraging the undesirable parts of the solar spectrum serves a dual function by shielding the solar cell while enhancing its efficiency. Without the need to alter the cell architecture, the incorporation of up and down photoconverter layers on either the front or rear surface of the device can maximize light harvesting. Up-conversion layers rely on a nonlinear optical process in which two photons in the infrared region are absorbed to generate visible light. On the other hand, several methods have been developed in the context of down-conversion, including quantum cutting [184], which is capable of splitting incident UV photons into two lower-energy photons instead of allowing the excess energy to be dissipated as heat. Moreover, processes based on rare-earth elements and involving partially split f–f transitions [185], as well as down-shifting mechanisms in organic compounds were successfully demonstrated. Whereas quantum dots and rare-earth inorganic compounds possess special photoluminescence properties, organic materials can be readily embedded in polymer layers and possess good thermal stability. In particular, aggregation-induced emission (AIE) molecules show large Stokes shifts, as the restriction of molecular vibrations and rotations suppresses non-radiative decay and enhances emission [186]. The latter materials have contributed to more than a 1% improvement in the cell's efficiency, making them a prospective choice among down-conversion materials [187].

Within this field of research, I performed a computational study of the optical properties of down-conversion materials. This led to a publication [188] that I co-authored in cooperation with our experimental partners: D. Głowienka, C.-M. Tsai, A. Sbai, D. Luo, P.-H. Lee, S.-H. Huang, C.-F. Li, H.-W. Wang, G.-S. Liou, J. Guthmuller, and W.-F. Su, ACS Appl. Mater. Interfaces **16** (2024) 63528-63539, *Improving the Efficiency of Semitransparent Perovskite Solar Cell Using Down-Conversion Coating.* In this publication, the experimental setup (**Figure 7.1**) developed by the our research partners consisted of a heterojunction semitransparent perovskite solar cell composed of the following layers: NiO$_x$/P3HT–COOH as the hole transport layer, a perovskite as the light-absorbing active layer, and PC$_{61}$BM/SnO$_2$ as the electron transport layer.

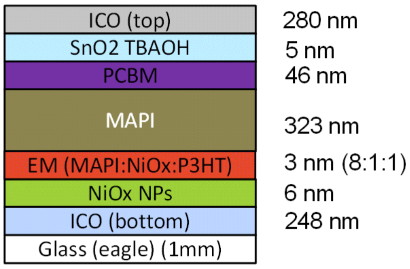

Figure 7.1: The optical configuration of the perovskite solar cells, including the respective thicknesses of all layers.

In order to enhance the efficiency of the solar cell, two specific AIE molecules, 4-(N, N-diphenylamino)benzaldehyde (DPABA) and N, N-diphenyl-4-(1,2,2-triphenylethenyl) benzenamine (TPETPA), were investigated and tested as potential down-conversion layers.

7.2 Summary of TDDFT results for the investigated down-conversion layers

In the first step, experimental spectroscopic techniques were employed to probe the cause of parasitic absorption. It appears that this absorption is mainly due to the glass and ITO bottom electrodes, especially on the front side, resulting in a loss of up to 0.56 mA cm^{-2} in the cell's overall photocurrent.

DPABA was homogeneously dispersed in a binder solution composed of TFEVE polymer to ensure the formation of a solid-state film. The experimental absorption spectra exhibit a hypsochromic shift from the 380 nm peak to approximately 360 nm, indicating changes in the molecular environment associated with aggregation (**Figure 7.2**). During this process, the intermolecular interactions are reinforced. In contrast, the experimental emission from the layer embedded in TFEVE shows a redshift of about 22 nm, triggered by interactions between the hydroxyl (–OH) functional groups in TFEVE and the central nitrogen atom of DPABA. This interaction alters the angular disposition of the benzene–C–N–benzene linkage.

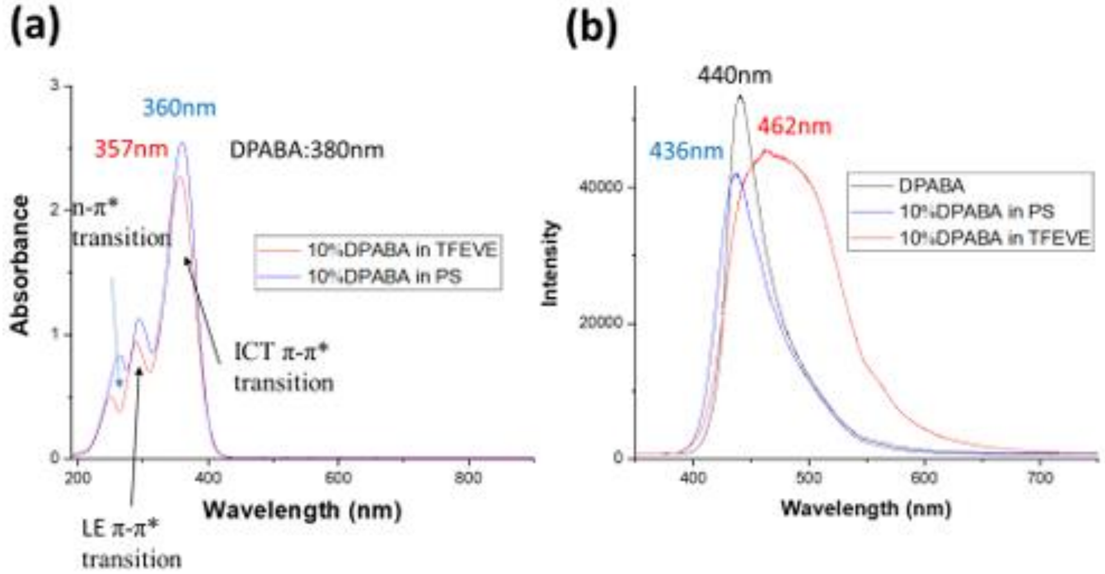

Figure 7.2: (A) Absorption and (B) photoluminescence spectra of DPABA dispersed in polystyrene (PS) and TFEVE, respectively.

The experimental part also discusses the dependency of the concentration of TPETPA and DPABA systems on their optical behavior. Increasing concentration enhances UV absorption until it reaches a plateau. For DPABA films, emission strengthens with aggregation up to an optimal concentration, while TPETPA films maintain stable emission across concentrations. This outlines the overall effect of aggregation in amplifying emission and suppressing non-radiative decay.

I performed quantum chemical calculations for DPABA and TPETPA molecules to gain a deeper understanding of their optical behaviors. This computational study aimed to identify and characterize the electronic transitions governing their absorption and emission processes. In this context, calculations were carried out on individual DPABA and TPETPA molecules in both vacuum and ethyl acetate (EtOAc) using the PCM model. However, this approach neglects weak intermolecular and hydrogen-bonding interactions that may play a critical role in describing the solid-state phase.

Table 7.1 Calculated state-specific vertical absorption and emission energies, along with Stokes shifts, as well as experimentally measured absorption and emission wavelength maxima.

	$\lambda_{Max,Abs}$ (nm)[a]	**$\lambda_{Max,Em}$ (nm)[a]**	**Stokes shift (eV)**
DPABA			
Theo. (vacuum)	332 (3.73)	422 (2.93)	-0.80
Theo. (ethyl acetate)	362 (3.42)	512 (2.42)	-1.00
Exp. (film)	355 (3.49)	482 (2.57)	-0.92
Exp. (ethyl acetate)	353 (3.51)	492 (2.52)	-0.99
TPETPA			
Theo. (vacuum)	362 (3.42)	646 (1.92)	-1.50
Theo. (ethyl acetate)	377 (3.29)	689 (1.80)	-1.49
Exp. (film)	361 (3.43)	500 (2.48)	-0.95

[a] The energy (in eV) associated to λ_{Max} is given in brackets.

For the DPABA compound, the electronic response of the solvent induces solvatochromic shifts of −0.31 eV and −0.51 eV (computed vertical energies of the lowest-lying excited state) for absorption and emission, respectively, compared to the vacuum. This reveals a pronounced dependence of the dye's spectra on its environmental conditions. Moreover, the excitation energies calculated in EtOAc show excellent agreement with the experimental data obtained in both EtOAc and the solid phase, with deviations of about 0.1 eV. This strong consistency confirms that the PCM model is capable of reproducing the key solute–environment interactions of DPABA, both in solution and in the condensed phase. These results were obtained using the SS solvation scheme of the PCM, which outperforms the LR approach in terms of accuracy. Intermolecular charge transfer occurring during relaxation was analyzed through CDD mapping. While the S_1 state of DPABA at the ground state geometry exhibits a partial local excited character, the transition to the optimized S_1 geometry involves a stronger CT character from the nitrogen center and the unsubstituted phenyl rings toward the phenyl–CHO group. This relaxation is accompanied by phenyl-ring rotations of 10–23°, owing to the unrestricted rotational motion in the solvated phase.

Concerning the TPETPA compound, the absorption exhibited a solvatochromic shift of –0.13 eV, showing only a small deviation from the experimental data, similar to that observed for DPABA. However, the emission displayed a solvatochromic shift of –0.12 eV, in clear contrast to the –0.51 eV reported for DPABA. Quantum chemical calculations showed an inconsistency with the experimental emission data for the aggregated phase of TPETPA, underestimating the emission energy by 0.68 eV. As a result, the predicted Stokes shift (–1.49 eV) was substantially larger than the experimentally observed value (–0.95 eV). This observation raises questions regarding the character of the S_1 electronic state at its optimized geometry. The CDD mapping of S_1 indicates a transition from the CT state at the ground-state geometry (S_0), characterized by electron transfer from the TPA donor to the TPE acceptor, to a locally excited state confined to the TPE moiety at the excited-state geometry (S_1). This structural alteration is likely caused by the phenyl rotations within the TPE group, which range from 18° to 38°, as observed during the PCM solvation modeling. This occurs because the compound is treated as an isolated monomer surrounded by a solvation cavity wherein specific interactions are neglected, rather than as part of a solid-state phase. It has been previously demonstrated that in EtOAc, a rapid non-radiative decay occurs for the $S_1 \rightarrow S_0$ transition. However, in the condensed phase, the state S_1 is destabilized due to restrictions on molecular rotational motion [189].

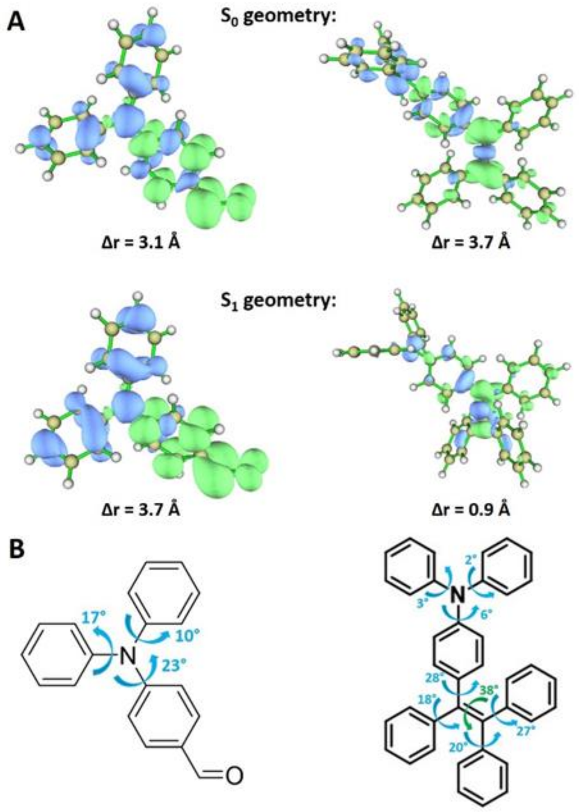

Figure 7.3: (A) Isosurfaces of charge density difference and charge transfer index (Δr) corresponding to the S_1 excitation in DPABA (left) and TPETPA (right). Positive (electron) and negative (hole) values are indicated in green and blue colors, respectively. (B) Rotation angles illustrating the principal structural changes between the S_0 and S_1 geometries for DPABA (left) and TPETPA (right).

7.3 Conclusion

The integration of down-conversion materials, obtained by blending the AIE dyes TPETPA or DPABA with the polymeric binder TFEVE and deposited on the front side of the solar cell, resulted in increases in the open-circuit voltage of 20 and 9 mV, respectively. Furthermore, the computational studies, despite their limitations, shed light on how the molecular environment affects the optical properties of the AIE dyes, highlighting their unique aggregation behavior.

Chapter 8: Summary and Perspectives

8.1 Summary

In this investigation, various quantum-chemical approaches were employed to assess the photoinduced electron-transfer mechanism in three BODIPY dyes used as photosensitizers in two-component photocatalytic hydrogen-generation systems. The dyes differ in the substitution pattern on the aromatic ring at the 8-position, bearing an EWG (NO_2) or an EDG (OH). The objectives were:1) benchmark (TDA)-TDDFT at the hybrid and double-hybrid levels against DLPNO-STEOM-CCSD in the Franck–Condon region for accuracy assessment. 2) Identify the nature of the electronic states that govern the electron-transfer processes in the three compounds, either promoting hydrogen production or causing compound deactivation and degradation in both neutral and reduced hydrogen production cycles, and assess the effect of the DCM solvent and the substituents on their adiabatic energies. 3) Evaluate the accuracy of the adiabatic and vertical Hessian models in predicting absorption, emission, and radiative/non-radiative rates relative to experimental data.

Regarding the comparison between (TDA)-TDDFT and DLPNO-STEOM-CCSD methods, MN15 reproduces the vertical excitation energies of both bright states and charge-transfer states with good accuracy relative to the DLPNO-STEOM-CCSD method, with an associated MAD of 0.25 eV, whereas it struggles to accurately describe the dissociative character due to its approximate treatment of electron correlation. As for the solvent effect, it was shown that it can lead to either stabilization or destabilization of the CT states, depending on the nature of the substituent. This provides a brief overview of the expected dominant character in the electron transfer pathway, including its accessibility in the vertical transition region.

Computational results for the neutral compound BOD-Ph show that, upon proceeding from the vertically excited bright state, the system may undergo ISC to a triplet state localized on the BODIPY core. The small SOC suggests that this triplet could be long-lived and populated, whereas triplet charge-transfer states are inaccessible. In contrast, for BOD-PhOH and BOD-$PhNO_2$, the proximity of the charge-transfer states to the bright states (first and second absorption peaks) at the CT states’ equilibrium geometries suggests that population may be feasible, with the caveat that the MN15 functional underestimates CT character relative to the DLPNO-STEOM-CCSD method.

Concerning the singly reduced compounds, TDA-TDDFT calculations show that only the doublet low-lying bright state can be populated at its minimum structure. In contrast, for the substituted BODIPY compounds, tracking the doublet CT states reveals that, at certain points along the relaxation pathway, they can prevail over competing electronic states, particularly for BOD-$PhNO_2$, as confirmed by both MN15 and the double-hybrid SOS-ωPBEPP86 functionals.

The above computational results comply with hypotheses 3.1 and 3.2 which propose that the propensity for populating the long-lived triplet state and the doublet bright state in the BOD-Ph compound coincides with the highest turnover number (TON) of hydrogen generation, whereas population of the charge-transfer states may act as a deactivation channel, consistent with the dramatic decrease in hydrogen production observed for BOD-PhOH and BOD-$PhNO_2$, (i.e., TON(BOD-$PhNO_2$) = 45, TON(BOD-PhOH) = 2997, TON(BOD-Ph) = 7389 [31])

Both vibronic models (AH and VH) successfully reproduced the k_r rate of BOD-Ph. In contrast, the k_{ic} rate showed inconsistent behavior, with the best agreement with experiment obtained when torsional motion was excluded within the VH model. Several attempts were made to adjust the parametrization of the rate, but these modifications had only a minor impact, largely due to the structural flexibility of BOD-Ph. Finally, the results concerning ISC show that k_{ISC} proceeds from the S_1 state toward the triplet level T_2, rather than directly to the lowest triplet state T_1.

8.2 Perspectives

While this study depicts electron transfer in the neutral and reduced cycles of the photosensitizers and draws post hoc inferences, it does not provide insight into the electron transfer between the photosensitizer and the catalyst, which is essential for assessing charge separation efficiency and the ability to accumulate charge from the key electronic states of the photosensitizers. The description of the dissociative state generally requires higher-level electronic structure approaches, such as RASPT2 or Quantum Monte Carlo. Likewise, standard vibronic treatments often fail to yield reliable internal conversion rates, which require more advanced methods like anharmonic QM/MM or quantum dynamics calculations. Such aspects could form the basis for further investigations.

References

[1] Höök M, Tang X. Depletion of fossil fuels and anthropogenic climate change—A review. *Energy Policy* 2013; 52: 797–809.

[2] Capellán-Pérez I, Mediavilla M, de Castro C, et al. Fossil fuel depletion and socio-economic scenarios: An integrated approach. *Energy* 2014; 77: 641–666.

[3] Kirsch S. Running out? Rethinking resource depletion. *Extr Ind Soc* 2020; 7: 838–840.

[4] Graham E, Fulghum N, Altieri K. *Global Electricity Review 2025. Ember*. 2025.

[5] Krozer Y, Bykuc S, Coenen F. Growth of Renewable Energy: A Review of Drivers from the Economic Perspective. *Energies (Basel)* 2025; 18: 5250.

[6] You B, Sun Y. Innovative Strategies for Electrocatalytic Water Splitting. *Acc Chem Res* 2018; 51: 1571–1580.

[7] Oka K, Tsujimura O, Suga T, et al. Light-assisted electrochemical water-splitting at very low bias voltage using metal-free polythiophene as photocathode at high pH in a full-cell setup. *Energy Environ Sci* 2018; 11: 1335–1342.

[8] Li X, Zhao L, Yu J, et al. Water Splitting: From Electrode to Green Energy System. *Nanomicro Lett* 2020; 12: 131.

[9] Tee SY, Win KY, Teo WS, et al. Recent Progress in Energy-Driven Water Splitting. *Adv Sci* 2017; 4: 1600337.

[10] Kawawaki T, Kawachi M, Yazaki D, et al. Development and Functionalization of Visible-Light-Driven Water-Splitting Photocatalysts. *Nanomaterials* 2022; 12: 344.

[11] Fujishima A, Honda K. Electrochemical Photolysis of Water at a Semiconductor Electrode. *Nature* 1972; 238: 37–38.

[12] Pålsson L-O, Flemming C, Gobets B, et al. Energy Transfer and Charge Separation in Photosystem I: P700 Oxidation Upon Selective Excitation of the Long-Wavelength Antenna Chlorophylls of Synechococcus elongatus. *Biophys J* 1998; 74: 2611–2622.

[13] Shen S, Jiang J, Guo P, et al. Effect of Cr doping on the photoelectrochemical performance of hematite nanorod photoanodes. *Nano Energy* 2012; 1: 732–741.

[14] Kikuchi E, Saito N, Yamaguchi Y, et al. Temperature Dependence of Photocatalytic Water Splitting under Visible Light Irradiation over Ir- and Sb-Codoped $SrTiO_3$:Al. *J Phys Chem C* 2025; 129: 2381–2390.

[15] Ye C, Zhang D-S, Chen B, et al. Interfacial Charge Transfer Regulates Photoredox Catalysis. *ACS Cent Sci* 2024; 10: 529–542.

[16] Wang K, Shen Y, Jeyakkumar P, et al. Supramolecular artificial light-harvesting systems for photocatalysis. *Curr Opin Green Sustain Chem* 2023; 41: 100823.

[17] Wouters KL, De Tacconi NR, Konduri R, et al. Driving multi-electron reactions with photons: Dinuclear ruthenium complexes capable of stepwise and concerted multi-electron reduction. *Photosynth Res* 2006; 87: 41–55.

[18] Ozawa H, Haga MA, Sakai K. A photo-hydrogen-evolving molecular device driving visible-light-induced EDTA-reduction of water into molecular hydrogen. *J Am Chem Soc* 2006; 128: 4926–4927.

[19] Teplý F. Photoredox catalysis by $[Ru(bpy)_3]^{2+}$ to trigger transformations of organic molecules: Organic synthesis using visible-light photocatalysis and its 20th century roots. *Collect Czechoslov Chem Commun* 2011; 76: 859–917.

[20] Keijer T, Bouwens T, Hessels J, et al. Supramolecular strategies in artificial photosynthesis. *Chem Sci* 2021; 12: 50–70.

[21] Zhang F, Jiang Y, Liu J, et al. Exploration of ultrafast dynamic processes in photocatalysis: Advances and challenges. *Fundam Res* 2025; 5: 2838–2849.

[22] Gobbato T, Volpato GA, Sartorel A, et al. A breath of sunshine: oxygenic photosynthesis by functional molecular architectures. *Chem Sci* 2023; 14: 12402–12429.

[23] Nachimuthu S, Lai KH, Taufany F, et al. Theoretical study on molecular design and optical properties of organic sensitizers. *Phys Chem Chem Phys* 2014; 16: 15389–15399.

[24] Narsaria AK, Poater J, Fonseca Guerra C, et al. Distortion-Controlled Redshift of Organic Dye Molecules. *Chem Eur J* 2020; 26: 2080–2093.

[25] Xie A, Pan ZH, Yu M, et al. Photocatalytic hydrogen production from acidic aqueous solution in BODIPY-cobaloxime-ascorbic acid homogeneous system. *Chin Chem Lett* 2019; 30: 225–228.

[26] Mou Z, Dong Y, Li S, et al. Eosin Y functionalized graphene for photocatalytic hydrogen production from water. *Int J Hydrogen Energy* 2011; 36: 8885–8893.

[27] Zhang X, Jin Z, Li Y, et al. Efficient Photocatalytic Hydrogen Evolution from water without an electron mediator over Pt−Rose Bengal Catalysts. *J Phys Chem C* 2009; 113: 2630–2635.

[28] Almazroai LS, El-Mekawy RE. Synergetic effects of Cu/TiO2 sensitized with different cyanine dyes on hydrogen evolution. *RSC Adv* 2019; 9: 24670–24681.

[29] Cui A, Peng X, Fan J, et al. Synthesis, spectral properties and photostability of novel boron–dipyrromethene dyes. *J Photochem Photobiol A Chem* 2007; 186: 85–92.

[30] Gemen J, Ahrens J, Shimon LJW, et al. Modulating the Optical Properties of BODIPY Dyes by Noncovalent Dimerization within a Flexible Coordination Cage. *J Am Chem Soc* 2020; 142: 17721–17729.

[31] Costabel D, Nabiyan A, Chettri A, et al. Diiodo-BODIPY Sensitizing of the $[Mo3S13]^{2-}$ Cluster for Noble-Metal-Free Visible-Light-Driven Hydrogen Evolution within a Polyampholytic Matrix. *ACS Appl Mater Interfaces* 2023; 15: 20833–20842.

[32] Bartelmess J, Francis AJ, El Roz KA, et al. Light-Driven Hydrogen Evolution by BODIPY-Sensitized Cobaloxime Catalysts. *Inorg Chem* 2014; 53: 4527–4534.

[33] Ziems K, Gräfe S, Kupfer S. Photo-Induced Charge Separation vs. Degradation of a BODIPY-Based Photosensitizer Assessed by TDDFT and RASPT2. *Catalysts* 2018; 8: 520.

[34] Liao J, Zhao H, Xu Y, et al. Novel BODIPY dyes with electron donor variety for dye-sensitized solar cells. *RSC Adv* 2017; 7: 33975–33985.

[35] D'Souza F, Smith PM, Zandler ME, et al. Energy transfer followed by electron transfer in a supramolecular triad composed of boron dipyrrin, zinc porphyrin, and fullerene: A model for the photosynthetic antenna-reaction center complex. *J Am Chem Soc* 2004; 126: 7898–7907.

[36] Roncali J. Molecular Bulk Heterojunctions: An Emerging Approach to Organic Solar Cells. *Acc Chem Res* 2009; 42: 1719–1730.

[37] Thompson BL. *BODIPY dyes: A privileged molecular scaffold with tunable properties. In: BODIPY Dyes – A Privileged Molecular Scaffold with Tunable Properties.* London: IntechOpen, 2019.

[38] Loudet A, Burgess K. BODIPY dyes and their derivatives: Syntheses and spectroscopic properties. *Chem. Rev* 2007; 107: 4891–4932.

[39] Zhang XF, Zhang Y, Xu B. Enhance the fluorescence and singlet oxygen generation ability of BODIPY: Modification on the meso-phenyl unit with electron withdrawing groups. *J Photochem Photobiol A Chem* 2017; 349: 197–206.

[40] Prlj A, Vannay L, Corminboeuf C. Fluorescence Quenching in BODIPY Dyes: The Role of Intramolecular Interactions and Charge Transfer. *Helv Chim Acta* 2017; 100: e1700093.

[41] Vyšniauskas A, Cornell B, Sherin PS, et al. Cyclopropyl Substituents Transform the Viscosity-Sensitive BODIPY Molecular Rotor into a Temperature Sensor. *ACS Sens* 2021; 6: 2158–2167.

[42] Nguyen VN, Yim Y, Kim S, et al. Molecular Design of Highly Efficient Heavy-Atom-Free Triplet BODIPY Derivatives for Photodynamic Therapy and Bioimaging. *Angew Chem Int Ed* 2020; 59: 8957–8962.

[43] Ly JT, Presley KF, Cooper TM, et al. Impact of iodine loading and substitution position on intersystem crossing efficiency in a series of ten methylated-meso-phenyl-BODIPY dyes. *Phys Chem Chem Phys* 2021; 23: 12033–12044.

[44] Llano RS, Zaballa EA, Bañuelos J. *Tailoring the photophysical signatures of BODIPY dyes: Toward fluorescence standards across the visible spectral region. In: BODIPY Dyes – A Privileged Molecular Scaffold with Tunable Properties*. London: IntechOpen, 2018.

[45] Mai DK, Kim C, Lee J, et al. BODIPY nanoparticles functionalized with lactose for cancer-targeted and fluorescence imaging-guided photodynamic therapy. *Sci Rep* 2022; 12: 2541.

[46] Hu W, Liu M, Zhang X-F, et al. Can BODIPY-Electron Acceptor Conjugates Act as Heavy Atom-Free Excited Triplet State and Singlet Oxygen Photosensitizers via Photoinduced Charge Separation-Charge Recombination Mechanism? *J Phys Chem C* 2019; 123: 15944–15955.

[47] Chen Y, Wan L, Zhang D, et al. Modulation of the spectroscopic properties of BODIPY derivatives through tuning the molecular configuration. *Photochem Photobiol Sci* 2011; 10: 1030–1038.

[48] Dorh N, Zhu S, Dhungana KB, et al. BODIPY-Based Fluorescent Probes for Sensing Protein Surface-Hydrophobicity. *Sci Rep* 2015; 5: 18337.

[49] Qi H, Teesdale JJ, Pupillo RC, et al. Synthesis, electrochemistry, and electrogenerated chemiluminescence of two BODIPY-appended bipyridine homologues. *J Am Chem Soc* 2013; 135: 13558–13566.

[50] Filatov MA, Karuthedath S, Polestshuk PM, et al. Generation of Triplet Excited States via Photoinduced Electron Transfer in meso-anthra-bodipy: Fluorogenic response toward singlet oxygen in solution and in vitro. *J Am Chem Soc* 2017; 139: 6282–6285.

[51] Xu Z, Huang Y, Cao Y, et al. Enhanced intersystem crossing of boron dipyrromethene by TEMPO radical. *J Chem Phys* 2020; 153: 154201.

[52] Liu D, El-Zohry AM, Taddei M, et al. Long-Lived Charge-Transfer State Induced by Spin-Orbit Charge Transfer Intersystem Crossing (SOCT-ISC) in a Compact Spiro Electron Donor/Acceptor Dyad. *Angewandte Chemie - International Edition* 2020; 59: 11591–11599.

[53] Wang Z, Zhao J, Barbon A, et al. Radical-Enhanced Intersystem Crossing in New BODIPY Derivatives and Application for Efficient Triplet-Triplet Annihilation Upconversion. *J Am Chem Soc* 2017; 139: 7831–7842.

[54] Krzemien W, Rohlickova M, Machacek M, et al. Tuning Photodynamic Properties of BODIPY Dyes, Porphyrins’ Little Sisters. *Molecules* 2021; 26: 4194.

[55] Rey YP, Abradelo DG, Santschi N, et al. Quantitative Profiling of the Heavy-Atom Effect in BODIPY Dyes: Correlating Initial Rates, Atomic Numbers, and $1O_2$ Quantum Yields. *Eur J Org Chem* 2017; 2017: 2170–2178.

[56] Yogo T, Urano Y, Ishitsuka Y, et al. Highly efficient and photostable photosensitizer based on BODIPY chromophore. *J Am Chem Soc* 2005; 127: 12162–12163.

[57] Sabatini RP, Lindley B, McCormick TM, et al. Efficient Bimolecular Mechanism of Photochemical Hydrogen Production Using Halogenated Boron-Dipyrromethene (BODIPY) Dyes and a Bis(dimethylglyoxime) Cobalt(III) Complex. *J Phys Chem B* 2016; 120: 527–534.

[58] Dura L, Ahrens J, Pohl M, et al. Design of BODIPY Dyes as Photosensitisers in Multicomponent Catalyst Systems for Light-Driven Hydrogen Production. *Chem Eur J* 2015; 21: 13549–13552.

[59] Cullen AA, Heintz K, O'Reilly L, et al. A Time-Resolved Spectroscopic Investigation of a Novel BODIPY Copolymer and Its Potential Use as a Photosensitiser for Hydrogen Evolution. *Front Chem* 2020; 8: 584060.

[60] Makino K, Imahori T, Kubo Y. A benzofuran[b]-fused BODIPY as an efficient sensitizer for photocatalytic hydrogen production. *Sustain Energy Fuels* 2021; 5: 3676–3686.

[61] Manton JC, Long C, Vos JG, et al. A photo- and electrochemical investigation of BODIPY-cobaloxime complexes for hydrogen production, coupled with quantum chemical calculations. *Phys Chem Chem Phys* 2014; 16: 5229–5236.

[62] Lewars EG. *Computational Chemistry*. Cham: Springer International Publishing, 2016.

[63] Nauenberg M. Max Planck and the birth of the quantum hypothesis. *Am J Phys* 2016; 84: 709–720.

[64] Pais A. Einstein and the quantum theory. *Rev Mod Phys* 1979; 51: 863–914.

[65] Einstein A. Die Plancksche Theorie der Strahlung und die Theorie der spezifischen Wärme. *Ann Phys* 1907; 327: 180–190.

[66] Tosto S. Reappraising 1907 Einstein's Model of Specific Heat. *Open J Phys Chem* 2016; 06: 109–128.

[67] Khanna V, Anwar J, Frenkel D, et al. Free energies of crystals computed using Einstein crystal with fixed center of mass and differing spring constants. *J Chem Phys* 2021; 154: 164509.

[68] Bohr N. On the constitution of atoms and molecules. *Philos Mag* 1913; 26: 1–25.

[69] Sales JH de O, Suzuki AT. Revisiting Angular Momentum Quantization in Bohr's Atomic Model. *J Eng Exact Sci* 2022; 8: 13960–01e.

[70] Duncan A, Janssen M. *The Oxford Handbook of the History of Quantum Interpretations*. Oxford: Oxford University Press, 2022.

[71] Eckert M. How Sommerfeld extended Bohr's model of the atom (1913–1916). *Eur Phys J H* 2014; 39: 141–156.

[72] Nastase H. *Quantum Mechanics*. Cambridge: Cambridge University Press, 2022.

[73] Atkins PW, Friedman RS. *Molecular Quantum Mechanics*. Oxford: Oxford University Press, 2010.

[74] Cramer CJ. Dyall K G, Fægri K, Jr.: Introduction to Relativistic Quantum Chemistry. *Theor Chem Acc* 2008; 119: 523–524.

[75] Bahoueddine T. Beyond the Madelung-Klechkowski Rule of Aufbau Orbital Filling Principle. *World J Chem Educ* 2015; 3: 160–167.

[76] Wang SG, Qiu YX, Fang H, et al. The Challenge of the So-Called Electron Configurations of the Transition Metals. *Chem Eur J* 2006; 12: 4101–4114.

[77] Karayianis N, Morrison CA. Physical Basis for Hund's Rule. *Am J Phys* 1964; 32: 216–220.

[78] Liu S, Langenaeker W. Hund's multiplicity rule: a unified interpretation. *Theor Chem Acc* 2003; 110: 338–344.

[79] Galbraith JM, Shaik S, Danovich D, et al. Valence Bond and Molecular Orbital: Two Powerful Theories that Nicely Complement One Another. *J Chem Educ* 2021; 98: 3617–3620.

[80] Plasser F, Ruckenbauer M, Mai S, et al. Efficient and Flexible Computation of Many-Electron Wave Function Overlaps. *J Chem Theory Comput* 2016; 12: 1207–1219.

[81] Bursill RJ, Castleton C, Barford W. Optimal parametrisation of the Pariser–Parr–Pople Model for benzene and biphenyl. *Chem Phys Lett* 1998; 294: 305–313.

[82] Gupta VP. *Principles and applications of quantum chemistry*. Academic Press (Elsevier), 2016.

[83] Ishikawa A, Nakashima H, Nakatsuji H. Accurate solutions of the Schrödinger and Dirac equations of H_2+ , HD+, and HT+: With and without Born–Oppenheimer approximation and under magnetic field. *Chem Phys* 2012; 401: 62–72.

[84] Cave RJ, Newton MD. Generalization of the Mulliken-Hush treatment for the calculation of electron transfer matrix elements. *Chem Phys Lett* 1996; 249: 15–19.

[85] Cederbaum LS, Friedman RS, Ryaboy VM, et al. Conical Intersections and Bound Molecular States Embedded in the Continuum. *Phys Rev Lett* 2003; 90: 013001.

[86] Roothaan CJC, Soukup GA. Accurate and stable numerical Hartree–Fock calculations for atoms. I. The $1s^2$ ground state of H^-, He, Li^+, and Be^{++}. *Int J Quantum Chem* 1979; 15: 449–462.

[87] Foresman JB, Frisch A. *Exploring Chemistry with Electronic Structure Methods Third Edition*. Wallingford: Gaussian Inc, 2015.

[88] Pranita RYP. *Principles of Quantum Chemistry*. New Delhi: Foundation Books, 2014.

[89] Jones RO. Density functional theory: Its origins, rise to prominence, and future. *Rev Mod Phys* 2015; 87: 897–923.

[90] Hugenholtz NM. Variational Principle in Quantum Mechanics. *Phys Rev* 1954; 96: 1158–1159.

[91] Szabo A, Ostlund NS. *Modern Quantum Chemistry Introduction to Advanced Electronic Structure Theory*. New York: Dover Publications, 1966.

[92] Samsonova I, Tucker GB, Alaal N, et al. Hydrogen-Atom Electronic Basis Sets for Multicomponent Quantum Chemistry. *ACS Omega* 2023; 8: 5033–5041.

[93] Boys SF. Electronic wave functions - I. A general method of calculation for the stationary states of any molecular system. *Proc R Soc Lond A* 1950; 200: 542–554.

[94] Traore D, Adjoua O, Feniou C, et al. Shortcut to chemically accurate quantum computing via density-based basis-set correction. *Commun Chem* 2024; 7: 269.

[95] George WO, Jones BF, Lewis RH. Computer Modelling of Properties of Alcohols. *Int J Vib Spect* 1999; 3: 5.

[96] Papajak E, Zheng J, Xu X, et al. Perspectives on Basis Sets Beautiful: Seasonal Plantings of Diffuse Basis Functions. *J Chem Theory Comput* 2011; 7: 3027–3034.

[97] Frisch MJ, Pople JA, Binkley JS. Self-consistent molecular orbital methods. 25. Supplementary functions for Gaussian basis sets. *J Chem Phys* 1984; 80: 3265–3269.

[98] Roscioni OM, Lee EPF, Dyke JM. Development and testing of a compact basis set for use in effective core potential calculations on rhodium complexes. *J Comput Chem* 2012; 33: 2049–2057.

[99] Bursch M, Mewes J, Hansen A, et al. Best-Practice DFT Protocols for Basic Molecular Computational Chemistry. *Angew Chem Int Ed* 2022; 61: e202205735.

[100] Xu LT, Dunning TH. Generalized Valence Bond Description of the Ground States (X1Σg+) of Homonuclear Pnictogen Diatomic Molecules: N2, P2, and As2. *J Chem Theory Comput* 2015; 11: 2496–2507.

[101] Lendvay G. On the correlation of bond order and bond length. *J Mol Struct THEOCHEM* 2000; 501–502: 389–393.

[102] Fuchs M, Niquet Y-M, Gonze X, et al. Describing static correlation in bond dissociation by Kohn–Sham density functional theory. *J Chem Phys* 2005; 122: 094116.

[103] Semidalas E, Martin JML. Correlation Consistent Basis Sets for Explicitly Correlated Theory: The Transition Metals. *J Chem Theory Comput* 2023; 19: 5806–5820.

[104] Hachmann J, Dorando JJ, Avilés M, et al. The radical character of the acenes: A density matrix renormalization group study. *J Chem Phys* 2007; 127: 134309.

[105] Møller Chr, Plesset MS. Note on an Approximation Treatment for Many-Electron Systems. *Phys Rev* 1934; 46: 618–622.

[106] Cremer D. Møller-Plesset perturbation theory: From small molecule methods to methods for thousands of atoms. *WIREs Comput Mol Sci* 2011; 1: 509–530.

[107] Jensen F. *Introduction to Computational Chemistry*. Hoboken: John Wiley & Sons, 2006.

[108] Čížek J. On the Correlation Problem in Atomic and Molecular Systems. Calculation of Wavefunction Components in Ursell-Type Expansion Using Quantum-Field Theoretical Methods. *J Chem Phys* 1966; 45: 4256–4266.

[109] Kitsaras MP, Stopkowicz S. Spin contamination in MP2 and CC2, a surprising issue. *J Chem Phys* 2021; 154: 131101.

[110] Tajti A, Szalay PG. Accuracy of Spin-Component-Scaled CC2 Excitation Energies and Potential Energy Surfaces. *J Chem Theory Comput* 2019; 15: 5523–5531.

[111] Bensberg M, Neugebauer J. Direct orbital selection within the domain-based local pair natural orbital coupled-cluster method. *J Chem Phys* 2021; 155: 224102.

[112] Schurkus HF, Luenser A, Ochsenfeld C. Communication: Almost error-free resolution-of-the-identity correlation methods by null space removal of the particle-hole interactions. *J Chem Phys* 2017; 146: 211106.

[113] Li Q, Huang Y, Lou Y, et al. Experimental electron density distribution of $KZnB_3O_6$ constructed by maximum-entropy method. *Powder Diffr* 2023; 38: 233–239.

[114] Nejadsattari F, Stadnik ZM. Spin polarized density functional theory calculations of the electronic structure and magnetism of the 112-type iron pnictide compound $EuFeAs_2$. *Sci Rep* 2021; 11: 12113.

[115] Zhang M-Y, Jiang H. Density-functional theory methods for electronic band structure properties of materials. *Sci Sin Chim* 2020; 50: 1344–1362.

[116] Slater JC. A Simplification of the Hartree-Fock Method. *Phys Rev* 1951; 81: 385–390.

[117] Perdew JP. Jacob's ladder of density functional approximations for the exchange-correlation energy. *AIP Conf Proc* 2001; 577: 1–20.

[118] Patra A, Bates JE, Sun J, et al. Properties of real metallic surfaces: Effects of density functional semilocality and van der Waals nonlocality. *PNAS* 2017; 114: E9188–E9196.

[119] Csonka GI, Perdew JP, Ruzsinszky A, et al. Assessing the performance of recent density functionals for bulk solids. *Phys Rev B* 2009; 79: 155107.

[120] Maurer RJ, Freysoldt C, Reilly AM, et al. Advances in Density-Functional Calculations for Materials Modeling. *Annu Rev Mater Res* 2019; 49: 1–30.

[121] Becke AD. Density-functional exchange-energy approximation with correct asymptotic behavior. *Phys Rev A* 1988; 38: 3098–3100.

[122] Lee C, Yang W, Parr RG. Development of the Colle-Salvetti correlation-energy formula into a functional of the electron density. *Phys Rev B* 1988; 37: 785–789.

[123] Polo V, Kraka E, Cremer D. Electron correlation and the self-interaction error of density functional theory. *Mol Phys* 2002; 100: 1771–1790.

[124] Sun J, Ruzsinszky A, Perdew JP. Strongly Constrained and Appropriately Normed Semilocal Density Functional. *Phys Rev Lett* 2015; 115: 036402.

[125] Becke AD. Density-functional thermochemistry. III. The role of exact exchange. *J Chem Phys* 1993; 98: 5648–5652.

[126] Chai J Da, Head-Gordon M. Long-range corrected hybrid density functionals with damped atom-atom dispersion corrections. *Phys Chem Chem Phys* 2008; 10: 6615–6620.

[127] Kumar VB, Śmiga S, Grabowski I. A Critical Evaluation of the Hybrid KS DFT Functionals Based on the KS Exchange-Correlation Potentials. *J Phys Chem Lett* 2024; 15: 10219–10229.

[128] Kepp KP. The ground states of iron(III) porphines: Role of entropy-enthalpy compensation, Fermi correlation, dispersion, and zero-point energies. *J Inorg Biochem* 2011; 105: 1286–1292.

[129] El-Meligy AB, El-Demerdash SH, Abdel-Rahman MA, et al. Structures, Energetics, and Spectra of (NH) and (OH) Tautomers of 2-(2-Hydroxyphenyl)-1-azaazulene: A Density Functional Theory/Time-Dependent Density Functional Theory Study. *ACS Omega* 2022; 7: 14222–14238.

[130] Srikanth KE, Veeraiah A, Pooventhiran T, et al. Detailed molecular structure (XRD), conformational search, spectroscopic characterization (IR, Raman, UV, fluorescence), quantum mechanical properties and bioactivity prediction of a pyrrole analogue. *Heliyon* 2020; 6: e04106.

[131] Matsushita Y, Nakamura K, Oshiyama A. Comparative study of hybrid functionals applied to structural and electronic properties of semiconductors and insulators. *Phys Rev B* 2011; 84: 075205.

[132] Chevrier VL, Ong SP, Armiento R, et al. Hybrid density functional calculations of redox potentials and formation energies of transition metal compounds. *Phys Rev B* 2010; 82: 075122.

[133] Boese AD, Martin JML. Development of density functionals for thermochemical kinetics. *J Chem Phys* 2004; 121: 3405–3416.

[134] Yu HS, He X, Li SL, et al. MN15: A Kohn-Sham global-hybrid exchange-correlation density functional with broad accuracy for multi-reference and single-reference systems and noncovalent interactions. *Chem Sci* 2016; 7: 5032–5051.

[135] Hohenstein EG, Chill ST, Sherrill CD. Assessment of the Performance of the M05−2X and M06−2X Exchange-Correlation Functionals for Noncovalent Interactions in Biomolecules. *J Chem Theory Comput* 2008; 4: 1996–2000.

[136] Sebastian S, Riley V, Wanniarachchi B, et al. Spin-scaled double hybrids with long-range correction solve the TD-DFT overestimation problem in BODIPY dyes: benchmarking and experimental validation. *RSC Adv* 2025; 15: 22419–22431.

[137] Grimme S. Density functional calculations with configuration interaction for the excited states of molecules. *Chem Phys Lett* 1996; 259: 128–137.

[138] Petersilka M, Gossmann UJ, Gross EKU. Excitation Energies from Time-Dependent Density-Functional Theory. *Phys Rev Lett* 1996; 76: 1212–1215.

[139] Dreuw A, Head-Gordon M. Single-Reference ab Initio Methods for the Calculation of Excited States of Large Molecules. *Chem Rev* 2005; 105: 4009–4037.

[140] Chantzis A, Laurent AD, Adamo C, et al. Is the Tamm-Dancoff approximation reliable for the calculation of absorption and fluorescence band shapes? *J Chem Theory Comput* 2013; 9: 4517–4525.

[141] Hu C, Sugino O, Watanabe K. Performance of Tamm-Dancoff approximation on nonadiabatic couplings by time-dependent density functional theory. *J Chem Phys* 2014; 140: 054106.

[142] Van Dijk J, Casanova-Páez M, Goerigk L. Assessing Recent Time-Dependent Double-Hybrid Density Functionals on Doublet-Doublet Excitations. *ACS Phys Chem Au* 2022; 2: 407–416.

[143] Fransson T, Pettersson LGM. Evaluating the Impact of the Tamm-Dancoff Approximation on X-ray Spectrum Calculations. *J Chem Theory Comput* 2024; 20: 2181–2191.

[144] Zhou C, Hermes MR, Wu D, et al. Electronic structure of strongly correlated systems: recent developments in multiconfiguration pair-density functional theory and multiconfiguration nonclassical-energy functional theory. *Chem Sci* 2022; 13: 7685–7706.

[145] Thomas DG, Chun J, Chen Z, et al. Parameterization of a geometric flow implicit solvation model. *J Comput Chem* 2013; 34: 687–695.

[146] Herbert JM. Dielectric continuum methods for quantum chemistry. *WIREs Comput Mol Sci* 2021; 11: e1519.

[147] Andreussi O, Dabo I, Marzari N. Revised self-consistent continuum solvation in electronic-structure calculations. *J Chem Phys* 2012; 136: 064102.

[148] Le Bris C (Ed.). *Handbook of Numerical Analysis, Vol. 10: Special Volume—Computational Chemistry*. Amsterdam: Elsevier Science B.V, 2003.

[149] Marenich A V., Cramer CJ, Truhlar DG. Universal Solvation Model Based on Solute Electron Density and on a Continuum Model of the Solvent Defined by the Bulk Dielectric Constant and Atomic Surface Tensions. *J Phys Chem B* 2009; 113: 6378–6396.

[150] Jana D, Jana S. Donor-Pyrene-Acceptor Distance-Dependent Intramolecular Charge-Transfer Process: A State-Specific Solvation Preferred to the Linear-Response Approach. *ACS Omega* 2020; 5: 9944–9956.

[151] Xu L. *Towards Improving The Accuracy of Implicit Solvent Models and Understanding Electrostatic Catalysis in Complex Solvent Environments*. Australian National University, 2022.

[152] Santos-Martins D, Forli S. Charting Hydrogen Bond Anisotropy. *J Chem Theory Comput* 2020; 16: 2846–2856.

[153] Do Casal MT, Veys K, Bousquet MHE, et al. First-Principles Calculations of Excited-State Decay Rate Constants in Organic Fluorophores. *J Phys Chem A* 2023; 127: 10033–10053.

[154] Humeniuk A, Bužančić M, Hoche J, et al. Predicting fluorescence quantum yields for molecules in solution: A critical assessment of the harmonic approximation and the choice of the lineshape function. *J Chem Phys* 2020; 152: 054107.

[155] Koseki S, Matsunaga N, Asada T, et al. Spin-Orbit Coupling Constants in Atoms and Ions of Transition Elements: Comparison of Effective Core Potentials, Model Core Potentials, and All-Electron Methods. *J Phys Chem A* 2019; 123: 2325–2339.

[156] Wang X, Zhang C, Liu J, et al. Relativistic two-electron contributions within exact two-component theory. *Chem Phys Rev* 2025; 6: 031404.

[157] Chibani S, Le Guennic B, Charaf-Eddin A, et al. Revisiting the optical signatures of BODIPY with ab initio tools. *Chem Sci* 2013; 4: 1950.

[158] Guennic B Le, Jacquemin D. Taking Up the Cyanine Challenge with Quantum Tools. *Acc Chem Res* 2015; 48: 530–537.

[159] Sia RCE, Arellano-Reyes RA, Keyes TE, et al. Radiative lifetime of a BODIPY dye as calculated by TDDFT and EOM-CCSD methods: solvent and vibronic effects. *Phys Chem Chem Phys* 2021; 23: 26324–26335.

[160] Chen Y, Zhao J, Guo H, et al. Geometry relaxation-induced large stokes shift in red-emitting borondipyrromethenes (BODIPY) and applications in fluorescent thiol probes. *J Org Chem* 2012; 77: 2192–2206.

[161] Jong F De, Feldt M, Feldt J, et al. Modelling absorption and emission of a meso-aniline-BODIPY based dye with molecular mechanics. *Phys Chem Chem Phys* 2018; 20: 14537–14544.

[162] Sbai A, Guthmuller J. Singlet and triplet excited states of a series of BODIPY dyes as calculated by TDDFT and DLPNO-STEOM-CCSD methods. *Phys Chem Chem Phys* 2024; 26: 25925–25935.

[163] Feldt M, Brown A. Assessment of local coupled cluster methods for excited states of BODIPY/Aza-BODIPY families. *J Comput Chem* 2021; 42: 144–155.

[164] Casanova-Páez M, Goerigk L. Assessing the Tamm–Dancoff approximation, singlet–singlet, and singlet–triplet excitations with the latest long-range corrected double-hybrid density functionals. *J Chem Phys* 2020; 153: 064106.

[165] Peach MJG, Williamson MJ, Tozer DJ. Influence of Triplet Instabilities in TDDFT. *J Chem Theory Comput* 2011; 7: 3578–3585.

[166] Virca CN, McCormick TM. DFT analysis into the intermediates of nickel pyridinethiolate catalysed proton reduction. *Dalton Trans* 2015; 44: 14333–14340.

[167] Felter KM, Grozema FC. Singlet Fission in Crystalline Organic Materials: Recent Insights and Future Directions. *J Phys Chem Lett* 2019; 10: 7208–7214.

[168] Jhun BH, Park Y, Kim HS, et al. The degradation mechanism of multi-resonance thermally activated delayed fluorescence materials. *Nat Commun* 2025; 16: 392.

[169] Nakahara K, Oyaizu K, Nishide H. Organic radical battery approaching practical use. *Chem Lett* 2011; 40: 222–227.

[170] Salewski M, Poltavtsev S V., Yugova IA, et al. High-resolution two-dimensional optical spectroscopy of electron spins. *Phys Rev X* 2017; 7: 031030.

[171] Hudson JM, Hele TJH, Evans EW. Efficient light-emitting diodes from organic radicals with doublet emission. *J Appl Phys* 2021; 129: 180901.

[172] Milaeva ER, Rubezhov AZ, Prokof'ev AI, et al. The Unpaired Electron in Transition Metal Complexes. *Russ Chem Rev* 1982; 51: 942–960.

[173] Fores M, Adamowicz L. A CASSCF-CASPT2 study of the excited-state intramolecular proton transfer reaction in 1-amino-3-propenal using different active spaces. *J Comput Chem* 1999; 20: 1422–1431.

[174] Casanova D, Krylov AI. Spin-flip methods in quantum chemistry. *Phys Chem Chem Phys* 2020; 22: 4326–4342.

[175] Luo GG, Fang K, Wu JH, et al. Noble-metal-free BODIPY-cobaloxime photocatalysts for visible-light-driven hydrogen production. *Phys Chem Chem Phys* 2014; 16: 23884–23894.

[176] Cerezo J, Santoro F. FCclasses3: Vibrationally-resolved spectra simulated at the edge of the harmonic approximation. *J Comput Chem* 2023; 44: 626–643.

[177] Cerezo J, Zúñiga J, Requena A, et al. Harmonic models in cartesian and internal coordinates to simulate the absorption spectra of carotenoids at finite temperatures. *J Chem Theory Comput* 2013; 9: 4947–4958.

[178] Ou Q, Peng Q, Shuai Z. Toward Quantitative Prediction of Fluorescence Quantum Efficiency by Combining Direct Vibrational Conversion and Surface Crossing: BODIPYs as an Example. *J Phys Chem Lett* 2020; 11: 7790–7797.

[179] Avila Ferrer FJ, Santoro F. Comparison of vertical and adiabatic harmonic approaches for the calculation of the vibrational structure of electronic spectra. *Phys Chem Chem Phys* 2012; 14: 13549–13563.

[180] Zhang X, Jacquemin D, Peng Q, et al. General Approach to Compute Phosphorescent OLED Efficiency. *J Phys Chem C* 2018; 122: 6340–6347.

[181] Veys K, Escudero D. Computational Protocol To Predict Anti-Kasha Emissions: The Case of Azulene Derivatives. *J Phys Chem A* 2020; 124: 7228–7237.

[182] Jiao L, Yu C, Wang J, et al. Unusual spectroscopic and photophysical properties of meso-tert-butylBODIPY in comparison to related alkylated BODIPY dyes. *RSC Adv* 2015; 5: 89375–89388.

[183] Liu J, He Y, Ding L, et al. Perovskite/silicon tandem solar cells with bilayer interface passivation . *Nature* 2024; 635: 596–603.

[184] Trupke T, Green MA, Würfel P. Improving solar cell efficiencies by down-conversion of high-energy photons. *J Appl Phys* 2002; 92: 1668–1674.

[185] van der Ende BM, Aarts L, Meijerink A. Lanthanide ions as spectral converters for solar cells. *Phys Chem Chem Phys* 2009; 11: 11081–11095.

[186] Li Y, Li Z, Wang Y, et al. Increasing the power output of a CdTe solar cell via luminescent down shifting molecules with intramolecular charge transfer and aggregation-induced emission characteristics. *Energy Environ Sci* 2013; 6: 2907–2911.

[187] Bella F, Griffini G, Correa-Baena J-P, et al. Improving efficiency and stability of perovskite solar cells with photocurable fluoropolymers. *Science (1979)* 2016; 354: 203–206.

[188] Glowienka D, Tsai C-M, Sbai A, et al. Improving the Efficiency of Semitransparent Perovskite Solar Cell Using Down-Conversion Coating. *ACS Appl Mater Interfaces* 2024; 16: 63528–63539.

[189] Lin H-T, Huang C-L, Liou G-S. Design, Synthesis, and Electrofluorochromism of New Triphenylamine Derivatives with AIE-Active Pendent Groups. *ACS Appl Mater Interfaces* 2019; 11: 11684–11690.